

Crack in Corrosion Flaw Assessment in Thin-Walled Pipe

by

Seyed Aliakbar Hosseini

A thesis

presented to the University of Waterloo

in fulfillment of the

thesis requirements for the degree of

Doctor of Philosophy

in

Mechanical and Mechatronics Engineering

Waterloo, Ontario, Canada, 2014

© Seyed Aliakbar Hosseini 2014

AUTHOR'S DECLARATION

I hereby declare that I am the sole author of this thesis. This is a true copy of the thesis, including any required final revisions, as accepted by my examiners.

I understand that my thesis may be made electronically available to the public.

Seyed Aliakbar Hosseini

Abstract

Pipelines are a safe and efficient method for transporting high volumes of oil and gas. However, aging pipelines may experience flaws, such as cracks or corrosion. Present approaches include detection, assessment and repair before flaws may become critical to the integrity of the line. There are different codes and standards for assessing pipeline flaws depending on the type of flaw, with the API 579 being the most common code for the assessment of cracks in oil and gas pipelines. Corrosion is commonly assessed using Modified B31G, CPS or the RSTRENG method. Other methods or procedures such as the Finite Element method may be used for evaluation of crack and corrosion flaws.

Cracks may occur coincident with corrosion representing a new hybrid flaw in gas and oil pipelines known as Crack in Corrosion (CIC) that is not directly addressed in the current codes or assessment methods. Hence, the goal of this study was to provide guidance for the assessment of CIC flaws in linepipe.

Four full scale rupture tests were undertaken to expand an existing data base in order to evaluate the collapse pressures of lines containing corrosion and/or cracks in a typical line pipe (API 5L Grade X52, 508 mm (20 inch) diameter, 5.7 mm wall thickness). Different types of flaws (cracks, corrosion and CIC) were formed. The mechanical properties of the pipe were measured using tensile, Charpy and J-testing for use in applying the evaluation criteria. Rupture tests were undertaken on end-capped sections containing uniform depth, finite length corrosion crack or CIC defects. Failure occurred by the combination of plastic collapse and ductile tearing of the corrosion flaws, cracks and CIC geometries tested. Two rupture tests were also carried out on 914.4 mm (36 inch) diameter pipe the mechanical properties of these pipes were measured using tensile, and Charpy tests.

API Level 3 Methods B & D are the most common procedures for assessing the crack flaws. In addition, FEM Level 3 FAD Method B was also applied which was based on the failure assessment diagram (FAD); however, the K_r ratio was defined as the ratio of the converged elastic-plastic J_{Total} to that of the critical value (J_Q). The L_r ratio was predicted using the actual stress in the remaining ligament (σ_{Ligament}), calculated using the FE analysis, to the yield stress.

All methods use some measure of fracture toughness. Most common are the Charpy test conversion, fracture toughness test (K) or J test. However, at present, there is no standard approach to measure the fracture toughness of thin-walled pipe, which is a critical parameter in assessing crack flaws. This was addressed by conducting J tests on sub-sized samples to determine the fracture toughness of the thin-walled line pipe steel using the ASTM E1820 procedure. Due to geometry limitations, J_Q was determined from the resistance curves (J versus crack extension). The average measured J_Q was 197 kJ/m². The average difference between the predicted failure pressure based on API Level 3 FAD Methods B and D, FEM Level 3 FAD Method B, and the experimental failure pressure was 30%, 14%, and 21% respectively.

In the absence of a standard for the evaluation of CIC flaws, they were treated as cracks in a pipe of reduced wall thickness with the same remaining ligament as the original CIC flaws. The average differences between the experimental and predicted failure pressures based on API Level 3 FAD Method B (25%), Method D (16%) and FEM Level 3 FAD Method B (11%) demonstrate that the FAD method can be used with toughness characterized using specimens of similar thickness to the pipe, although the toughness results are not geometry independent.

Table of Contents

List of Figures	viii
List of Tables	xiii
Nomenclature	xv
Chapter 1 Introduction	1
1.1 Motivation	1
1.2 Thesis Overview	4
Chapter 2 Literature Review	5
2.1 Fracture Mechanics	5
2.1.1 An Atomic View of Fracture	5
2.1.2 Linear-Elastic Fracture Mechanics (LEFM) [13]	7
2.1.3 Elastic-Plastic Fracture Mechanics (EPFM) [18]	18
2.2 Plastic Collapse Concept	35
2.2.1 Net Section Yield Load [53]	35
2.2.2 Global versus Local Collapse	37
2.3 Material Characterization	38
2.3.1 Tensile Test [5]	38
2.3.2 Charpy Test [5]	38
2.3.3 Fracture Toughness Test, Values and Trends	43
2.4 Flaw Assessment Methods [5]	52

2.4.1	Corrosion Flaw Assessment	52
2.4.2	Crack Flaw Assessment	56
2.5	Experimental Burst Tests [5]	61
2.5.1	Corrosion Flaws	62
2.5.2	Crack Flaws	64
2.5.3	Crack in Corrosion (CIC) Flaws	66
Chapter 3	Experimental Testing	69
3.1	Material Characterization	69
3.1.1	Tensile Test	70
3.1.2	Charpy Tests	72
3.2	Experimental Rupture Tests	75
3.2.3	20 Inch Diameter Pipes	75
3.2.4	36 Inch Diameter Pipes	75
Chapter 4	Results and Discussion	80
4.1	Corrosion Flaws	80
4.1.1	Corrosion-Finite Element Model Development	80
4.1.2	Collapse Pressure Prediction for a Corrosion Flaw	82
4.1.3	Comparison between Experimental, Analytical, and FEM Results	86
4.2	Crack Flaws	88
4.2.1	Crack Flaws-Finite Element Model Development	88
4.2.2	Collapse Pressure Prediction for a Crack Flaw	93
4.2.3	Comparison between Experimental, Analytical, and FEM Results	97

4.3	Crack in Corrosion (CIC) Flaws.....	102
4.3.1	Crack in Corrosion (CIC) Flaws- Finite Element Model Development.....	102
4.3.2	Comparison between Experimental, Analytical, and FEM Results	102
4.3.3	CIC Parametric Study.....	105
Chapter 5	Conclusions and Future Work	110
5.1	Conclusions	110
5.2	Recommendations and Future Work.....	112
References	113
Appendix A:	API Level I Evaluation.....	125
Appendix B:	Q-Stress	127

List of Figures

Figure 1-1- Examples of Pipeline Flaws.....	2
Figure 2-1- Schematic of the Fracture Phenomenon from View Point of Scale Levels [12]	6
Figure 2-2- Potential Energy and Force as a Function of Atomic Separation. At the Equilibrium Separation X_0 the Potential Energy is Minimized and the Attractive and Repulsing Forces are balanced [10].....	7
Figure 2-3-Elliptical Hole in a Flat Plate	8
Figure 2-4- Potential Energies for Two Neighbouring Crack Lengths and the Energy Change dU Used to Define the Strain Energy Release Rate G [15]	9
Figure 2-5- Crack Propagation in Various Types of Materials, with Corresponding Fracture Energy. a) Ideally Brittle Material b)Quasi-brittle Elastic-Plastic Material and, c) Brittle Material with Crack Meandering and Branching [10]	11
Figure 2-6-Variation of Energy with Crack Length [13].....	12
Figure 2-7- The Three Modes of Loading that can be Applied to a Crack [10]	13
Figure 2-8- Three-dimensional Coordinate System for the Region of a Crack Tip [15].....	14
Figure 2-9- Plastic Zone Size and Shape around Crack Tip [18]	15
Figure 2-10- Plastic Zone of Plane Stress and Plane Strain [19]	16
Figure 2-11- A Crack and its Plastic Zone, and the Larger K -field that Must Exist for LEFM to be Applicable [15].....	17
Figure 2-12- Small Plastic Zone Compared with Planner Dimensions [15]	18

Figure 2-13- Range of Applicability of LEFM and EPFM for Describing Fracture Behavior [18]	19
Figure 2-14- Schematic Residual Strength Diagrams for a) Relatively Brittle and b) Relatively Ductile materials [18]	19
Figure 2-15- Crack Tip Opening Displacement (CTOD). An Initially Sharp Crack Blunts with Plastic Deformation, Resulting in a finite Displacement (δ) at the Crack Tip [10]	21
Figure 2-16- Alternative Definitions of CTOD a) Displacement at the Original Crack Tip b) Displacement at the Intersection of a 90° Vertex with the Crack Flanks [10]	22
Figure 2-17- The SE(B) Specimen for Estimating CTOD from Three Point Bend Specimen [10]	22
Figure 2-18- Determination of the Plastic Component of the Crack Mouth Opening Displacement [10]	23
Figure 2-19- Arbitrary Contour around the Tip of a Crack to Characterize J [10]	24
Figure 2-20- Effect of Plasticity on the Crack Tip Stress Fields: a) Small Scale Yielding, b) Elastic-Plastic Conditions, and c) Large-Scale Yielding	28
Figure 2-21- Crack Tip Stress Fields for a Center Cracked Panel in Plane Strain with $a/W = 0.75$ and $n = 10$ [29]	29
Figure 2-22- Crack Tip Stress Fields for an Edge Cracked Bend Specimen in Plane Strain With $a/W = 0.75$ and $n = 10$ [28]	30
Figure 2-23- Schematic Showing the Experimental Test Data of Fracture Toughness as a Function of the Constraint [37]	33
Figure 2-24- J and J-Q* Controlled Zones in Ductile Crack Growth [39]	35
Figure 2-25- CVN vs. K_{IC} (Tyson 2005) [60]	40

Figure 2-26- K_{mat} Plotted against Charpy Impact Energy for Upper Shelf Behavior [2]	41
Figure 2-27- Scaled Energy Chart [5].....	42
Figure 2-28- Standardized Fracture Mechanics Test Specimens [10]	45
Figure 2-29- Force vs. Displacement Curve during an Elastic-Plastic Fracture Toughness Test [15].....	46
Figure 2-30- J-Integral Example Test Result for One Pipe Section	46
Figure 2-31- Fracture Toughness vs. Temperature for Different Steels [15]	49
Figure 2-32- Effect of Thickness on Fracture Toughness	50
Figure 2-33- Effect of Loading Rate on the Fracture Toughness of a Structural Steel [15].....	51
Figure 2-34- Comparison of Temperature-Transition Behaviors for KIC and Charpy Test on a Same Steel [15]	52
Figure 2-35- A Corroded Pipe Section	53
Figure 2-36- Corrosion Flaw Profile.....	55
Figure 2-37- Failure Assessment Diagram (Level 1) [73].....	58
Figure 2-38- Failure Assessment Diagram (Level 3) [1].....	58
Figure 2-39- Illustration of Tearing Instability Criterion [4].....	61
Figure 2-40- A Sample Corrosion Flaw Profile.....	62
Figure 2-41- An Artificial Corrosion in a Tested Pipe	62
Figure 2-42- Failure Pressures Comparison between the Analytical Methods and the Experimental [5]	63
Figure 2-43- Machined slit, and crack after cyclic loading	64
Figure 2-44- Crack Profile in a Tested Pipe after Pre-Fatiguing Procedure.....	65
Figure 2-45- CIC Flaw Manufacture a) Cut slit, b) Fatigue crack and c) Corrosion flaw [73]....	66

Figure 2-46- Comparison between Crack, Corrosion and CIC Flaws of Equivalent Depths	67
Figure 3-1- The Engineering and True Stress-Strain Curves in Circumferential Direction for One of Specimens	70
Figure 3-2- Tensile Tests Results for 36” Diameter Pipe 1 (A) & Pipe 2 (B)	71
Figure 3-3- The Sample Fracture Surfaces of Charpy Specimens (20” Diameter Pipe)	73
Figure 3-4 Charpy V-Notch Impact Test Results (Full Size-36 Inches Pipes)	74
Figure 3-5- 36”s Pipe Sections before Rupture Tests	76
Figure 3-6 Collapse Pressure Prediction for Crack using API579 Level 2 FAD Method B (Pipe1-36”)	77
Figure 3-7- The Tested Pipe 2 Containing Corrosion Flaw after the Rupture Test.....	78
Figure 3-8- Sample Flaws for 36 inches Pipes	79
Figure 4-1- Boundary Condition of the Corrosion Model (45%)	81
Figure 4-2- A Sample Corrosion Model (45% WT).....	82
Figure 4-3-Corrosion Flaw Model (45% WT).....	85
Figure 4-4- FE Analysis of Corrosion Flaws (varying depths).....	85
Figure 4-5- Predicted Corrosion Flaw Collapse Pressure Compared to Experimental Data	87
Figure 4-6--Singular 2D Element (Right) Produced from Regular 6-Node Triangular Element [102].....	89
Figure 4-7- Predicted J integral value for elastic and elastic-plastic analysis (47% WT)	89
Figure 4-9- The Crack Tip and Crack Front for the EPFM Analysis	90
Figure 4-10- J Contour convergence and the remaining net section beyond the converged J Contour (average stress calculated for this section)	91

Figure 4-11- Quarter Symmetry Crack Model (47% WT) (Top: Geometry, Bottom Left: Crack, Right: Close view of crack tip mesh).....	92
Figure 4-12- The J-Integral throughout the Semi-Elliptical Crack (47% WT)	94
Figure 4-13- Failure Pressure Prediction for Cracks using API579 Level 3 FAD Method B	97
Figure 4-14-Failure Pressure Prediction for Cracks using API579 Level 3 FAD (Method D) (47%WT)	98
Figure 4-15- FE Analysis for FEM Level 3 FAD Method B API 579 (47% WT)	100
Figure 4-16- CIC Quarter Model (Left: Geometry, Right: FE Mesh)	102
Figure 4-17-Crack in Corrosion (left) and Equivalent Cracks in the Remained Pipe Section Profile.....	103
Figure 4-18-Transverse View through CIC Flaw	106
Figure 4-19- Collapse Pressure Prediction for CIC Flaws of Varying Different Crack & Corrosion Ratio for Total Depth of (20% WT)	107
Figure 4-20- Collapse Pressure Prediction for CIC Flaws of Varying Different Crack & Corrosion Ratio for Total Depth of (40% WT)	108
 Figure A.1- FEM Analysis of 47% WT Crack Model using a Modified Level 1 FAD	 125
 Figure B.1- Modified Boundary Layer Analysis	 127
Figure B.2- Boundary Conditions of MBL Model (47%WT)	128
Figure B.3- Boundary Layer Mesh	129
Figure B.4- von-Mises Stress Distribution for MBL Model (47% WT)	129

List of Tables

Table 2-1- Charpy Test Results (scaled to full size equivalent using Equation (2.41) [5]	42
Table 2-2- Charpy Impact Energy Correlation to Fracture Toughness in Different Methods.....	43
Table 2-3- Comparison of Measured and Predicted Failure Pressures for the Pipes Tested in Different Methods.....	65
Table 2-4- CIC flaw geometry	67
Table 2-5- Comparison between the Experimental and the Predicted Collapse Pressures for CIC Flaws	68
Table 3-1-Charpy V-Notch Impact Test Results (20” Diameter Pipe) (Full Size).....	72
Table 3-2- Upper & Lower Shelf Energy (Full Size-36 Inches Pipes).....	74
Table 3-3- Pipe Dimension (Geometry & Flaws-36” Diameter).....	76
Table 3-4- Comparison between the Experimental and the Predicted Collapse Pressures (Pipe 1-36”)	77
Table 3-5- Comparison between the Experimental and the Predicted Collapse Pressures (Pipe 2-36”)	78
Table 4-1- Comparison between Experimental and FEM Results for Corrosion Modeling	86
Table 4-2- API Failure Pressure predictions for Crack Flaws	98
Table 4-3- FEM Failure Pressure predictions for Crack Flaws	100
Table 4-4- CIC Flaw Dimensions for API analysis	103
Table 4-5- API Failure Pressure predictions for CIC Flaws.....	104
Table 4-6- FEM Failure Pressure Predictions for CIC Flaws.....	104

Table 4-7-Test Matrix for CIC Parametric Study	106
Table 4-8- Parametric Study for CIC Flaws (20% WT)	107
Table 4-9- Parametric Study for CIC Flaws (40% WT)	108
Table A.1- FEM Collapse Pressure predictions for Crack Flaws	126

Nomenclature

a	Crack depth/length
a_i	Initial crack
A	Fracture area of the Charpy specimen
A_{pl}	Plastic area
B	Material thickness
C_{eq}	Crack half length
CVN	CVN Charpy fracture energy
CVN^S	Sub-size specimen Charpy impact energy
d	Flaw depth
ds	Increment of contour path
D	Pipe diameter
Δa	Crack extension
δ	Crack tip opening displacement
E	Elasticity modulus
E'	Elasticity modulus for plane strain
ϵ_{ref}	Reference strain
G	Energy per unit crack area required to extend the crack
γ_p	Plastic work per unit area
γ_s	Surface energy per unit area

Γ	Arbitrary path enclosing the crack tip
J	J integral
J_{el}	Elastic portion of J-integral
J_{IC}	Fracture toughness in J-integral terms determined at the point of instability
J_{pl}	Plastic portion of J-integral
J_Q	J-integral value at crack extension by tearing of 0.2 mm
K	Stress strength of material
K_I	Stress Intensity
K_{IC}	Fracture toughness of material for plane strain
K_{ic}	Threshold stress intensity for plane stress
K_Q	Fracture value at rapid crack propagation
K_r	Ordinate of the failure assessment diagram (FAD) ($=K_I / K_{IC}$)
K_t	Stress concentration
L	Length of corroded area
L_r	Abscissa of the failure assessment diagram (FAD Level 2 &3) ($=\sigma_{ref}^P / \sigma_0$)
$L_{r(max)}^P$	FAD cutting line localized plastic collapse
M	Folias bulging factor
M_p	Bulging factor
ν	Poisson ratio
P	Force
P_C	The value of CTOD force at the onset of stable crack extension
P_f	Failure pressure
P_Q	The value of CTOD force at rapid crack propagation

P_u	The value of CTOD force at the onset of unstable crack extension
R	Pipe radius
r_p	Plastic zone radius
σ_c	Cohesive stress
σ_m	Nominal stress
σ_0	Yield strength
σ_θ	Hoop stress
σ_{yy}	Opening stress ahead of crack
σ_u	Ultimate tensile strength
σ_{ref}^P	Reference stress
σ_f	Flow stress
t	Pipe wall thickness
T	T stress
t_c	Thickness of the full-size specimen
t_c^s	Thickness of the sub-size specimen
T_i	Traction vector
t_0	Plane stress thickness
t_1	Plane strain thickness
u_i	Displacement vector at ds
U	Strain energy
U_e	Elastic energy
U_s	Surface energy
V_c	Clip gage displacement at onset of stable crack extension

V_g	Total clip gage displacement
V_p	The plastic component of total clip gage displacement
V_u	Clip gage displacement onset of unstable crack extension
W	Specimen width
w	the strain energy density
Y	Dimensionless geometrical factor

Chapter 1

Introduction

1.1 Motivation

Pipelines have been used widely for the transport of oil and gas since the 1860s. They are the most economical high capacity form of transportation for natural gas, oil and petroleum. Pipeline flaws resulting from degradation of the protective coating or cathodic protection degradation, a corrosive environment, or third party damage may lead to corrosion, crack or hybrid crack-in-corrosion flaws. Although the mechanisms that create these flaws vary, the resulting flaws require assessment to determine fitness for continued service or the need for repair. The most common flaws in pipelines include corrosion, crack and more recently hybrid crack-in-corrosion (CIC) flaws (Figure 1-1).

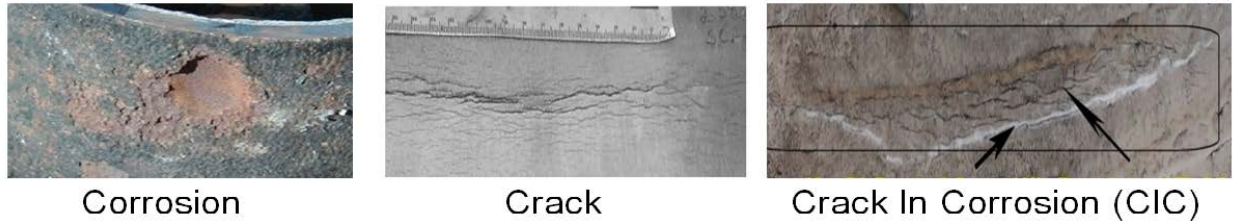


Figure 1-1- Examples of Pipeline Flaws

Based on the type of flaw, there are different codes and standards for assessing flaws in pipelines. For instance, the most common codes for crack flaw assessment in oil and gas pipelines are API 579 [1], and BS7910 [2] and the most common methods for corrosion assessment flaws are RSTRENG and Modified B31G [3]. Besides these codes and methods, there are some other numerical programs, such as CorLAS [4], which have been used successfully for assessing cracks in pipelines.

Previous work [5] has demonstrated application of existing crack or corrosion evaluation techniques of equivalent depth and length to CIC geometry in a typical line pipe (API 5L Grade X52, 508 mm diameter, 5.7mm wall thickness) and the results showed that the CIC collapse pressures were bounded by those of a long corrosion groove (upper bound) and a long crack (lower bound), with the collapse dominated by the crack when the crack depth was significant. Moreover, this work highlighted the need for improved measures of material properties for thin-walled pipes. In particular, one of the largest gaps in knowledge is the material toughness for thin-walled pipes, which is used in the evaluation techniques. The usual fracture mechanics tests are not well suited to measuring the fracture toughness of thin material due to geometry limitations. Therefore, there is a need to measure a meaningful fracture toughness value for thin-walled pipes. Gas and oil transmission pipelines are usually between 203.2 (8 in) and 1219.2 mm (48 in) in diameter and 4.8 (0.25 in) and up to 31.8 mm (1.25 in) in wall thickness [6, 7]. In

general, a pipe is considered thin-walled when the wall thickness (t) is less than $1/20$ of the diameter (D) [7].

The fracture toughness values for thin-walled pipes can be determined by using three different methods as follows:

- A) Conducting the direct fracture toughness test (J test) [8]
- B) Correlating the Charpy test upper shelf energy values to K_{IC} or J_{IC} using empirical correlations which can be found in different standards such as API 579 [1] or BS 7910 [2]
- C) Using the Tyson-CANMET (2005) empirical correlations between Charpy energy and K_{IC} or J_Q [9]

It has been noted that each method provides a different estimate of toughness. The fracture toughness values for method A to C in the previous work [5] for API 5L Grade X52, 508 mm diameter, 5.7mm wall thickness pipe were 202, 89, and 121 $MPa\sqrt{m}$ respectively. This confirms that there is a large difference, i.e. 227 %, between the highest and lowest of fracture toughness calculations, which results an average of 30% difference in the collapse pressure prediction for a specific crack depth. Therefore, the most important step to develop a new method for assessing a CIC flaw or even optimizing the other current assessment methods for cracks or corrosion flaws is an accurate measurement of the material properties. However, due to geometry limitations it is commonly not possible to measure an acceptable J_{IC} value, and no study has been conducted to determine how to measure this or correctly interpret the results from tests on thin-walled material.

The primary benefit of this study will be the development of an accurate method to evaluate crack and CIC flaws in operating lines, and an understanding the limitations and sensitivity of this method to the input parameters. This work will be directly enabled by fundamental studies to

evaluate the fracture toughness of thin sections and will lead to improved integrity assessment and safety for operating lines. Another goal of this study is finding a way determining the procedure to evaluate CIC flaws.

1.2 Thesis Overview

The present thesis contains four major parts: assessment methods, material characterization, experimental rupture tests, and finite element modeling. The overall structure of the thesis is as follows:

Chapter 2 briefly presents background information about fracture mechanics, plastic collapse concept, and assessment methods for corrosion, crack and CIC flaws. Moreover, the previous work regarding the material characterization and experimental rupture tests are reviewed in this Chapter.

Chapter 3 introduces the extended material characterization tests included Tensile and Charpy tests. It also reviews the rupture test results for both 20 & 36 inch pipe diameter. Moreover, it presents the geometry dimension, and type of flaws contained in the tested pipes.

Chapter 4 covers the finite element modeling for corrosion, crack and CIC flaws. The experimental with analytical and FEM results are compared. The parametric study of CIC flaws presented in this Chapter.

Finally, chapter 5 summarizes the research contributions, gives concluding remarks, and recommendations for future work.

Chapter 2

Literature Review

2.1 Fracture Mechanics

The concept of fracture mechanics was developed before 1960, and was applicable only to materials that obeyed Hooke's law and the specific analysis of cracks in components was not possible [10, 11]. In fact, engineering design was based on tension, compression or bending; along with failure criteria for uncracked material. The method assumed that there was no large crack in the component. Since 1960, fracture mechanics theories have been developed to account for nonlinear material behavior.

2.1.1 An Atomic View of Fracture

It is well known that fracture involves a complex and multistage process, which initiates well before the occurrence of visible cracks. A material fractures when sufficient stress is applied at

the atomic level to break the bonds between atoms. The linear scales of fracturing are shown in Figure 2-1.

It is worth noting that the strength of a material is due to the cohesive forces between atoms. The attractive and repulsive force acting on the two atoms varies in relation to the separation between them (Figure 2-2).

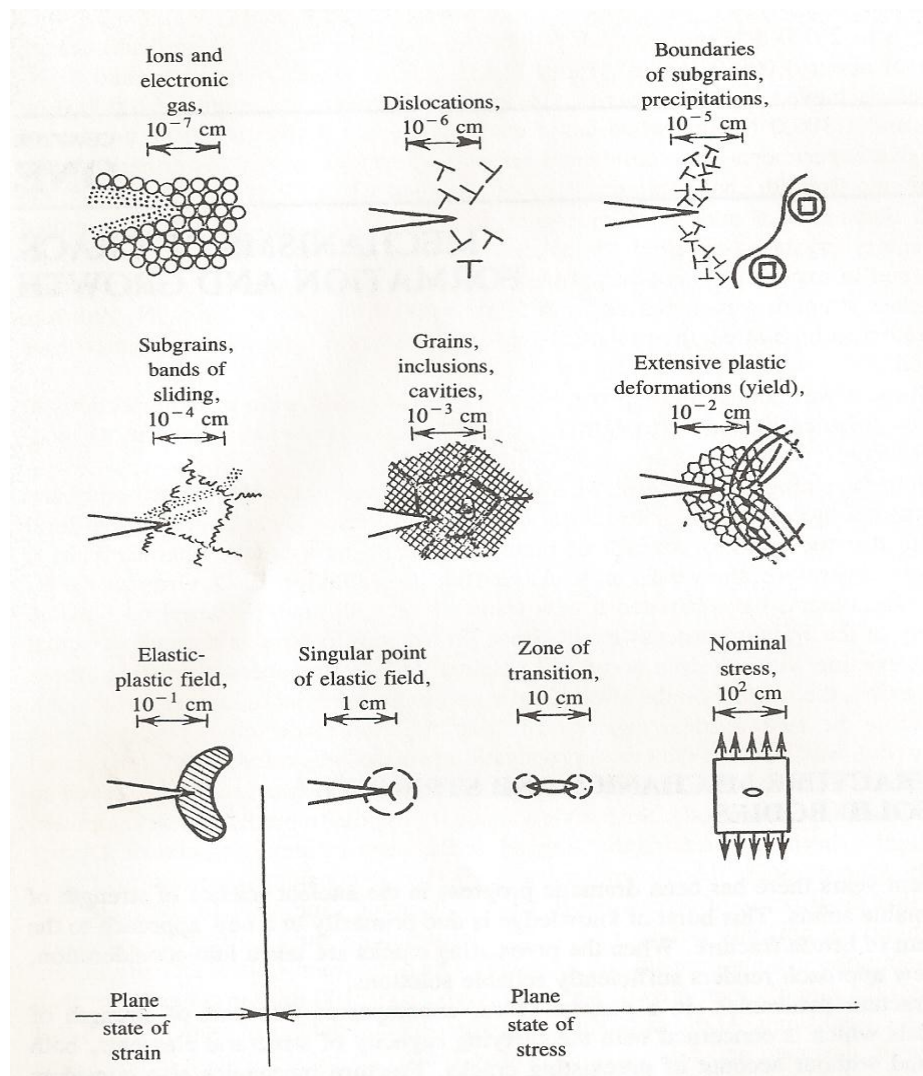


Figure 2-1- Schematic of the Fracture Phenomenon from View Point of Scale Levels [12]

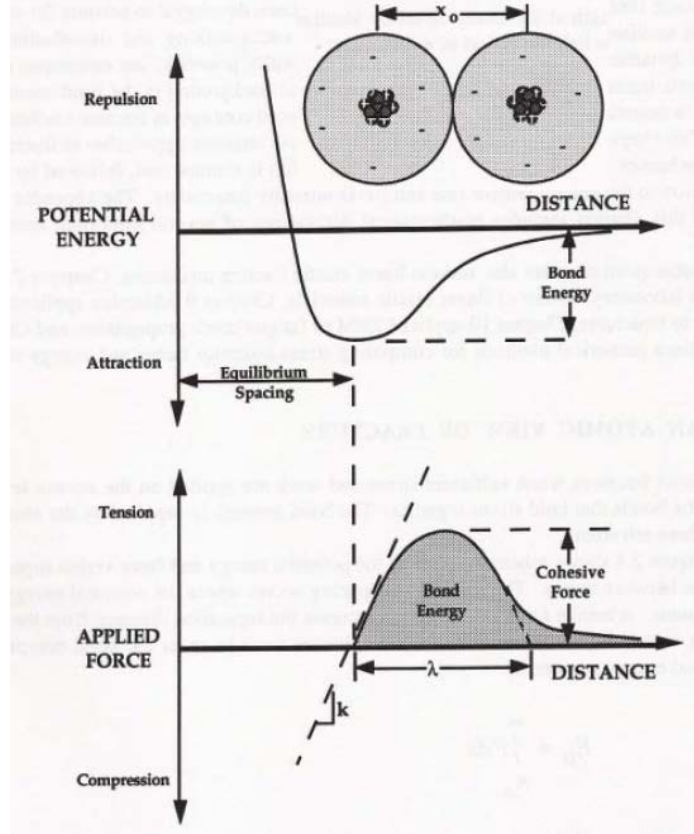


Figure 2-2- Potential Energy and Force as a Function of Atomic Separation. At the Equilibrium Separation X_0 the Potential Energy is Minimized and the Attractive and Repulsing Forces are balanced [10]

The theoretical cohesive stress σ_c can be obtained in relation to the sine curve above as follows:

$$\sigma_c = \sqrt{\frac{E\gamma}{x_0}} \quad (2.1)$$

2.1.2 Linear-Elastic Fracture Mechanics (LEFM) [13]

Linear-elastic fracture mechanics (LEFM) developed from the early work of Griffith [14] who explained why the observed strength of a material was considerably less than the theoretical strength based on the forces between atoms. He concluded that real materials contain flaws and

small cracks which reduce their strength. These cracks cause stress concentrations. This is because an elliptical flaw (Figure 2-3) has its stress concentration factor defined as follows:

$$K_t = 1 + 2\left(\frac{a}{b}\right) \quad (2.2)$$

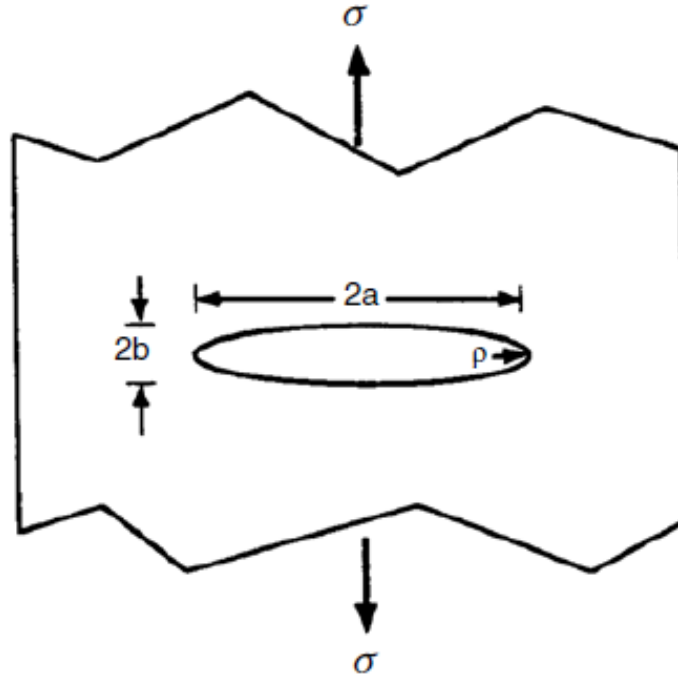


Figure 2-3-Elliptical Hole in a Flat Plate

As $b \rightarrow 0$ the flaw becomes a crack, but $K_t \rightarrow \infty$ which would suggest that a material with a crack would not be able to withstand any applied forces. This is contrary to what was observed, so Griffith developed a concept to explain how a stable crack could exist in a material. He explained that a crack only becomes unstable if an increment of crack growth, da , results in more potential energy, G , being released which can be absorbed by the creation of the new crack surface (Figure 2-4 and Equation (2.3)).

$$G = -\frac{1}{t} \frac{dU}{da} \quad (2.3)$$

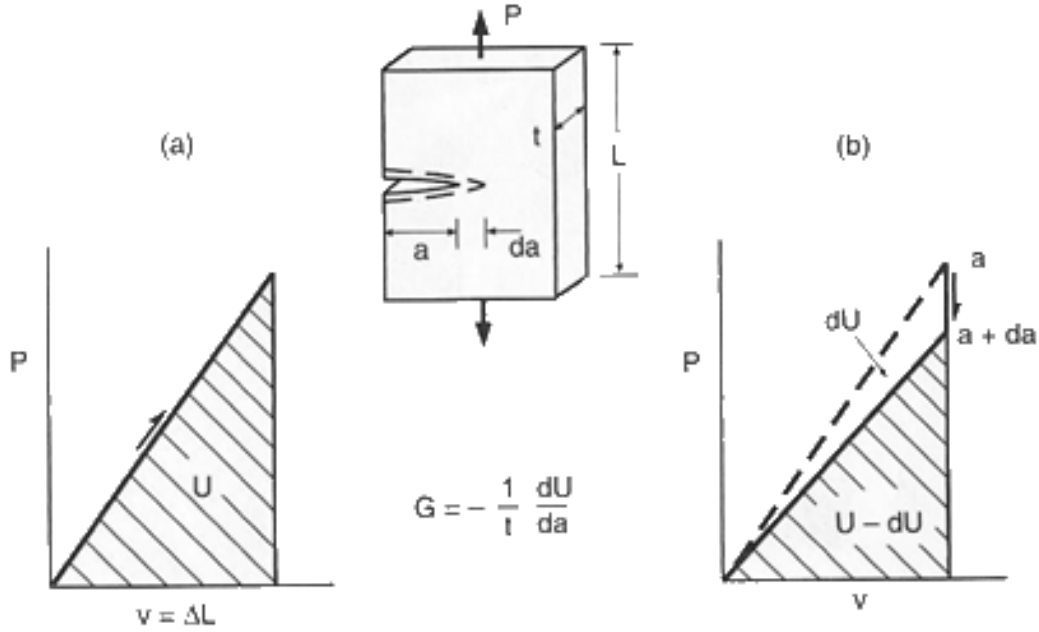


Figure 2-4- Potential Energies for Two Neighbouring Crack Lengths and the Energy Change dU Used to Define the Strain Energy Release Rate G [15]

The energy consumed in crack propagation is denoted by $R=dU/da$ which is called the crack resistance. It is assumed that the energy required to produce a crack is the same for each increment (da). This means that R is constant, and G must be equal R (or reach the critical value G_{IC}) before crack growth can occur. Therefore, crack propagates when:

$$G_{IC} = \frac{\pi \sigma_c^2 a}{E} \quad (2.4)$$

$$\sigma_c = \sqrt{\frac{2E\gamma_s}{\pi a}} = \sqrt{\frac{EG_{IC}}{\pi a}} \quad (2.5)$$

It should be noted that this is correct for brittle materials such as glass that crack with essentially no plastic deformation ($2\gamma_s = G$). However, in ductile materials, a majority of the energy may be used in deforming the material in the plastic zone at the crack tip. In applying G

to metals in the 1950s, Irwin [16] showed that the concept was applicable even to these circumstances if the plastic zone was small. Therefore, Equation (2.6) can be revised for ductile material as follows:

$$\sigma_c = \sqrt{\frac{2E(\gamma_s + \gamma_p)}{\pi a}} \quad (2.6)$$

It is possible to generalize the Griffith model to account for any type of energy dissipation:

$$\sigma_c = \sqrt{\frac{2Ew_f}{\pi a}} \quad (2.7)$$

where w_f is fracture energy, which could include plastic, viscoelastic, or viscoplastic effects, depending on the material. Figure 2-5 shows various types of material behavior and the corresponding fracture energy. As shown, there is no plastic zone at the crack tip in ideally brittle materials. However, there is a small plastic zone at the crack tip in quasi-brittle elastic-plastic materials. The fracture energy can be increased by crack tip branching in brittle materials.

It should be noted that the Griffith model applies only to linear elastic material behavior. Thus the global behavior of the structure must be elastic. Any nonlinear effects, such as plasticity, must be confined to a small region near the crack tip. In addition, Equation (2.7) assumes that W_f is constant. In many ductile materials, the fracture energy increases with crack growth [10].

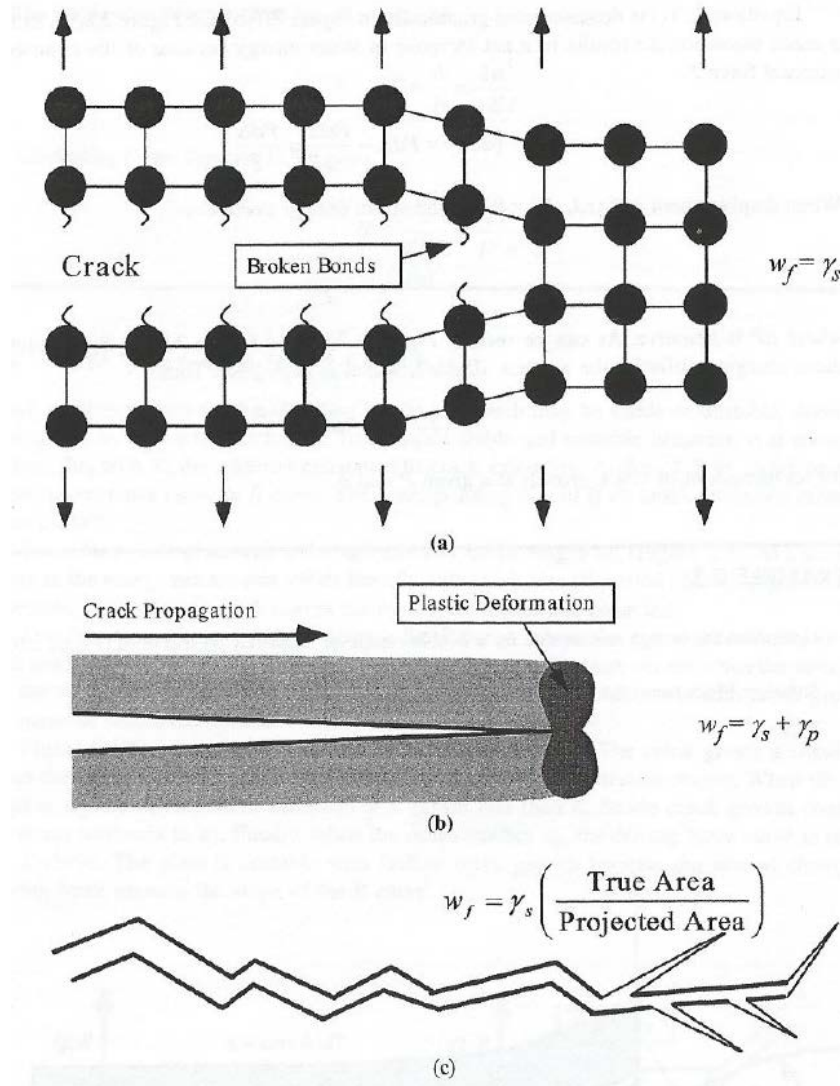


Figure 2-5- Crack Propagation in Various Types of Materials, with Corresponding Fracture Energy. a) Ideally Brittle Material b) Quasi-brittle Elastic-Plastic Material and, c) Brittle Material with Crack Meandering and Branching [10]

2.1.2.1 Strain Energy Release Rate

For a through crack of length $2a$ in an infinite body of unit thickness, as shown in Figure 2-3, the surface energy U_s stored in the material due to the formation of the crack is given by:

$$U_s = 2a * 2\gamma_s \quad (2.8)$$

Considering $2\gamma_s = G$, the Equation (2.8) may be written as follows:

$$U_s = 2aG \quad (2.9)$$

Based upon stress field calculations for an elliptical flaw by Inglis [17], Griffith calculated the elastic strain energy released by the formation of a crack as :

$$U_e = \frac{\pi\sigma^2 a^2}{E} k \quad (2.10)$$

where $k = (1 - \nu^2)$ for plane strain and $k=1$ for plane stress.

The surface energy increases linearly with crack length (a), whereas the energy released by the formation of the crack increases with a^2 .

The total energy in the presence of a crack is the mathematical summation of the surface energy U_s and the energy released U_e (Figure 2-6). The critical condition occurs at point A corresponding to the critical crack a_c where $dU/da=0$.

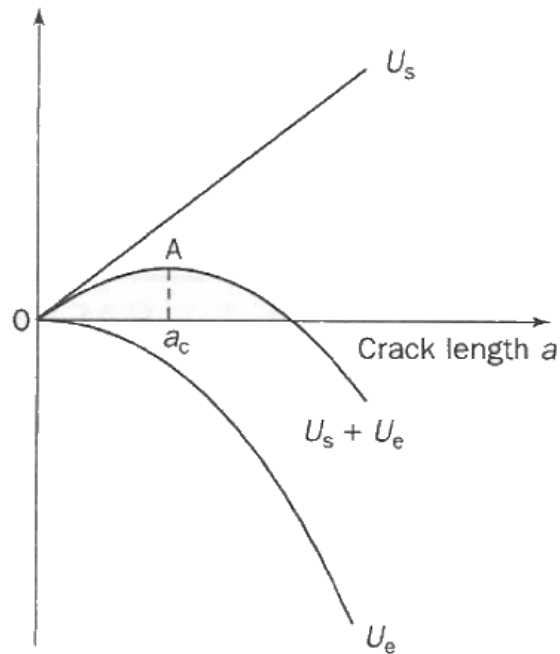


Figure 2-6-Variation of Energy with Crack Length [13]

2.1.2.2 Stress Intensity Factor

There are three common modes of loading (Figure 2-7). Mode I is the opening mode where the principal load is applied normal to the crack plane and consists of the crack faces simply moving apart. Mode II corresponds to a sliding mode and tends to slide one crack face to one another in the direction normal to the leading edge of the crack. Mode III is a tearing mode which refers to sliding of the crack faces, but now the direction is parallel to the leading edge. In general, mode I loading is the most common in industry and engineering design.

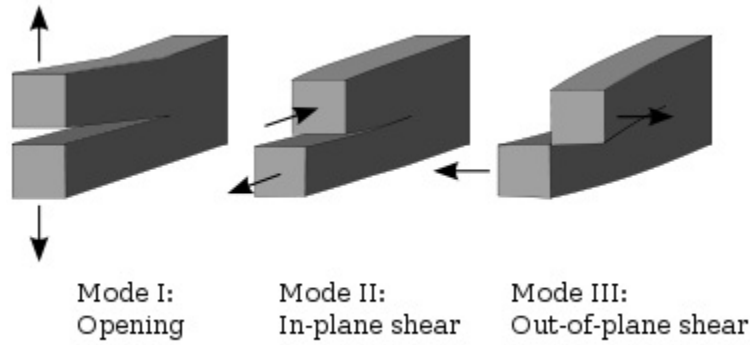


Figure 2-7- The Three Modes of Loading that can be Applied to a Crack [10]

Irwin showed that the elastic stress distribution at the crack tip subjected to external load (Figure 2-8) for mode I is as follows:

$$\begin{aligned}
 \sigma_x &= \frac{k}{\sqrt{2\pi r}} \cos\left(\frac{\theta}{2}\right) \left[1 - \sin\left(\frac{\theta}{2}\right) \left(\frac{3\theta}{2}\right)\right] \\
 \sigma_y &= \frac{k}{\sqrt{2\pi r}} \cos\left(\frac{\theta}{2}\right) \left[1 + \sin\left(\frac{\theta}{2}\right) \left(\frac{3\theta}{2}\right)\right] \\
 \tau_{xy} &= \frac{k}{\sqrt{2\pi r}} \sin\left(\frac{\theta}{2}\right) \cos\left(\frac{\theta}{2}\right) \cos\left(\frac{3\theta}{2}\right) \\
 \sigma_z &= 0 \quad (\text{Plane stress})
 \end{aligned}
 \tag{2.11}$$

$$\sigma_z = \nu(\sigma_x + \sigma_y), \quad \varepsilon_z = \tau_{yz} = \tau_{zx} = 0 \quad (\text{Plane strain})$$

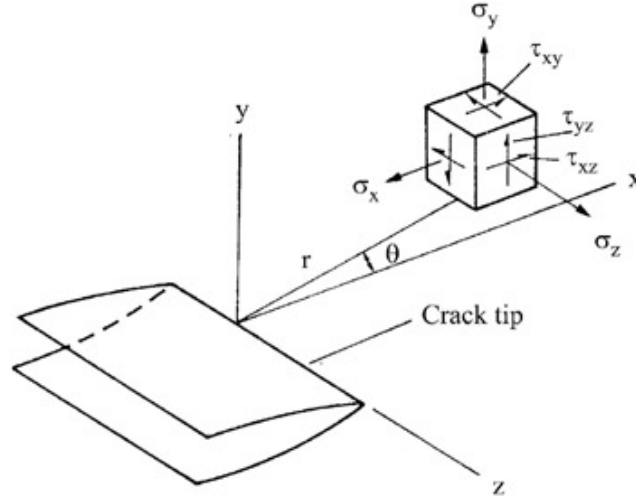


Figure 2-8- Three-dimensional Coordinate System for the Region of a Crack Tip [15]

Equation (2.11) is applicable for ductile materials with limited plastic deformation at the crack tip.

Irwin observed that the stresses are proportional to $(\pi a)^{0.5}$, where a is the half-length of the crack. Therefore, he defined the stress intensity factor K as follows:

$$k = \sigma \sqrt{\pi a} \quad (2.12)$$

The stress intensity in the above equation for mode I is K_I . For mode I $\theta=0$ and shear stress is zero, hence Equation (2.11) can be written as follows:

$$\sigma_x = \sigma_y = \frac{k}{\sqrt{2\pi r}} \quad (2.13)$$

In general, the crack length is assumed small compared to the size of the component. As the crack size increases, or component dimensions decrease, the outer boundaries begin to exert an influence on the crack tip. Under such conditions, the stress intensity solution is usually not applicable in analytical methods. In order to extend the applicability of the LEFM approach

beyond the case of a central crack in an infinite plate, K_I is usually expressed in the more general form as follows:

$$k_I = Y\sigma_m\sqrt{\pi a} \quad (2.14)$$

2.1.2.3 Crack Tip Plasticity

The stresses at the crack tip should be infinite based on Equation (2.11). However, in reality, the stresses at the crack tip are finite because the crack tip radius is finite. Moreover, the elastic stress analysis becomes more inaccurate as the plastic region at the crack tip grows. Combining the elastic solution around the crack tip with the von-Mises yield criterion, the size and the shape of the plastic zone for plane stress and plane strain (Figure 2-9) is expressed as follows:

$$r_p = \frac{1}{2\pi} \left(\frac{K_{IC}}{\sigma_0} \right)^2 \quad \text{Plane Stress} \quad (2.15)$$

$$r_p = \frac{1}{6\pi} \left(\frac{K_{IC}}{\sigma_0} \right)^2 \quad \text{Plane Strain} \quad (2.16)$$

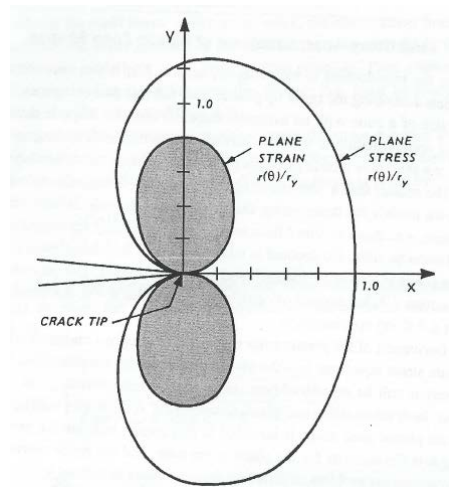


Figure 2-9- Plastic Zone Size and Shape around Crack Tip [18]

The ratio of the plastic zone to the specimen thickness is an important factor (Figure 2-10). If the size of the plastic zone is nearly equal to the plate thickness (plane stress), then the plate can yield freely in the thickness direction. On the other hand, if the plastic zone size is much smaller than, the plate thickness (plane strain), the plate cannot yield simply along the plate thickness. This is due to the surrounding material, as shown in Figure 2-10.

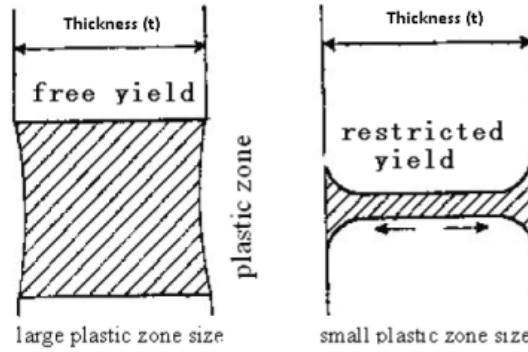


Figure 2-10- Plastic Zone of Plane Stress and Plane Strain [19]

Following ASTM E399 [20], a specimen is considered to be in a state of plane stress when $r_p/t \approx 1$ and in a state of plane strain when $r_p/t \leq 0.025$ [19]. The plane stress and plane strain thickness can be determined using following two equations as follows:

$$t_0 = \frac{1}{3\pi} \left(\frac{K_{IC}}{\sigma_0} \right)^2 \quad \text{Plane Stress} \quad (2.17)$$

$$t_1 = 2.5 \left(\frac{K_{IC}}{\sigma_0} \right)^2 \quad \text{Plane Strain} \quad (2.18)$$

2.1.2.4 Plastic Zone Size and Plasticity Limitations For LEFM [15]

The stresses near the crack tip in linear elastic materials vary with $\frac{1}{\sqrt{r}}$, but Equation (2.11) does not describe the stress distribution inside the plastic zone. However, if the plastic zone is

small enough, there is a region outside of the crack tip where Equation (2.11) is still applicable. This region is named K-controlled fracture or the K-field (Figure 2-11).

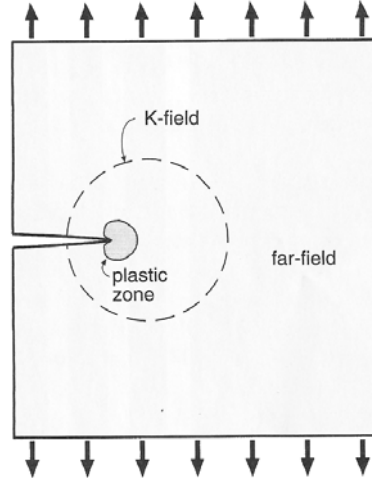


Figure 2-11- A Crack and its Plastic Zone, and the Larger K-field that Must Exist for LEFM to be Applicable [15]

The existence of such a region is necessary for LEFM theory to be applicable. The K-field surrounds and controls the behavior of the plastic zone at the crack tip. Although the actual stress distribution at the plastic zone is unknown, it can be argued the size of plastic zone and stress distribution within the K-field region are functions of the boundary conditions and material properties of the K-field region. Thus, K continues to characterize the severity of the crack, despite the occurrence of limited plasticity. However, if the plastic zone is large, then K is no longer applicable.

In general, the distance between the crack tip to any boundary of the specimen, such as a , $(b - a)$, and h (Figure 2-12), should be greater than $8r_p$ [15]. Considering Equations (2.15) & (2.16), the plastic radius for the plane stress condition is greater than that for plane strain, so an overall limit on the use of LEFM is as follows:

$$a, (b - a), h \geq \frac{4}{\pi} \left(\frac{K_{IC}}{\sigma_0} \right)^2 \quad (2.19)$$

The above equation should be satisfied for all three dimensions of a , $(b-a)$, and h . Otherwise, the situation closely approaches gross yielding with the plastic zone extending to one of the boundaries, as shown in Figure 2-12.

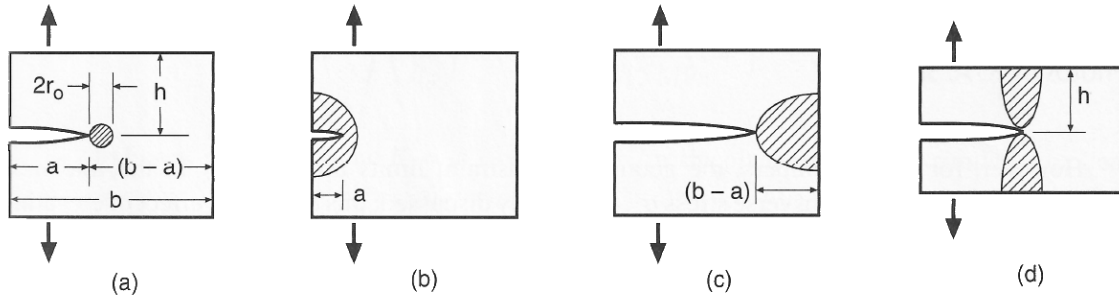


Figure 2-12- Small Plastic Zone Compared with Planar Dimensions [15]

2.1.3 Elastic-Plastic Fracture Mechanics (EPFM) [18]

Linear elastic fracture mechanics (LEFM) was developed to characterize the crack behavior for brittle materials. In this case, there is a small plastic zone surrounding the crack tip. However, such conditions are met only for brittle materials such as glasses, ceramics and rocks. Moreover, it was shown that the LEFM concept could be extended to more ductile materials where the crack tip plastic zone is slightly greater than that for a brittle material, and the K-field region still controls the behavior of the plastic zone. Nevertheless, there are other materials which show nonlinear behavior, when the crack tip plastic zone is large enough. For these types of materials, other method such as elastic-plastic fracture mechanics (EPFM) is applied. It is worth noting that EPFM is not applicable to general yielding conditions (or plastic collapse). The range of applicability of LEFM and EPFM in the different regions of fracture behavior is shown in Figure 2-13.

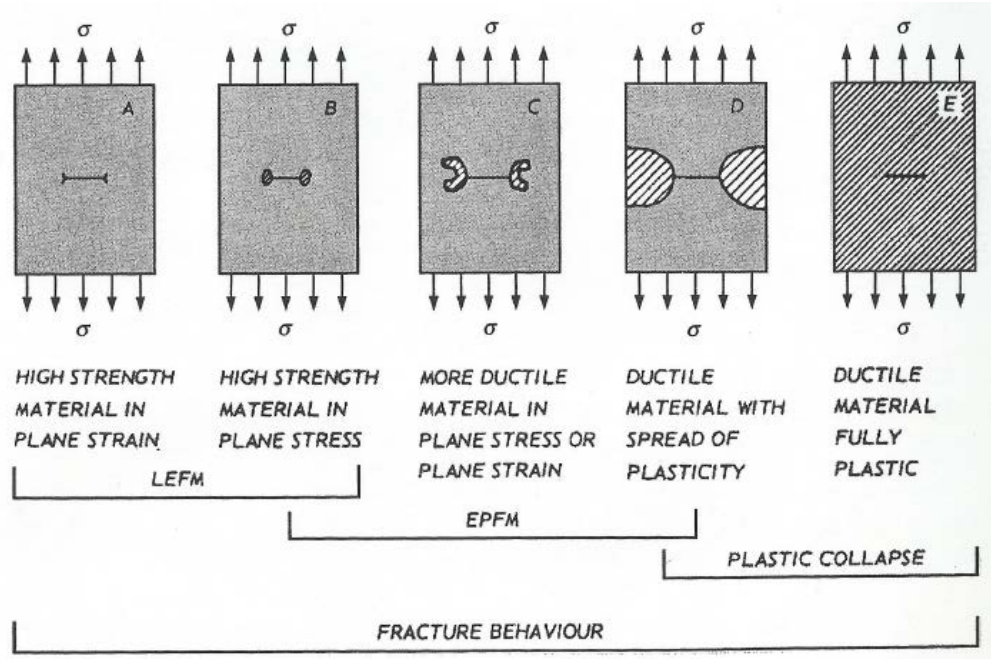


Figure 2-13- Range of Applicability of LEFM and EPFM for Describing Fracture Behavior [18]

As shown in Figure 2-13, there is some overlap of the applicability for LEFM and EPFM methods. This can be explained in more detail based on Figure 2-14 which gives a schematic residual strength diagram for relatively brittle and ductile materials.

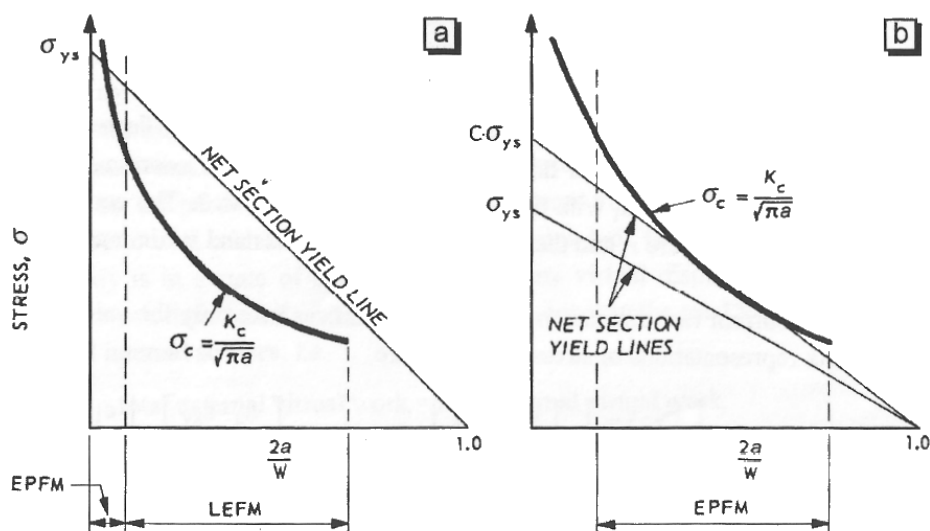


Figure 2-14- Schematic Residual Strength Diagrams for a) Relatively Brittle and b) Relatively Ductile materials [18]

For the dimensionless crack length, $2a/w$, of a center cracked component (Figure 2-14.a), the residual strength is determined by the stress intensity factor, since the K_c curve lies well below the line representing net section yield of the un-cracked ligaments. Therefore, LEFM is applicable for most cases. However, for very short cracks the plastic zone is no longer small, and EPFM should be applied. For relatively ductile materials (Figure 2-14.b), the unconstrained yield stress, σ_0 , will be reached in the un-cracked ligaments well before the critical stress $\sigma_0 = \frac{K_c}{\sqrt{\pi a_c}}$ because the critical stress intensity factor, K_c , is high in ductile materials. Therefore, yielding occurs earlier than fracture, and LEFM or EPFM are not applicable. However, in the plane strain condition, the effective yield stress increases to $C\sigma_0$, and the K_c curve may then predict a failure stress, σ_c , of the same order of magnitude as that given by the net section yield line. In such a situation as shown in Figure 2-14.b, for the wide range of $2a/w$, the EPFM approach can be applied. It is worth noting that the ratio of the principal stress, σ_1 , and the yield stress becomes as high as 3 for plane strain conditions. This ratio is named the plastic constraint factor, C .

2.1.3.1 Crack Tip Opening Displacement (CTOD or COD)

The COD approach was introduced by Wells in 1960 [21]. He found that the stress and strain in the vicinity of a crack tip causes failure. At the crack tip the stresses always exceed the yield strength, and plastic deformation occurs. Therefore, he concluded that if plastic strain reaches a critical value, then plastic strain at the crack tip controls fracture. Wells noticed that the crack faces moved apart prior to fracture in test specimens which exhibited a high degree of plasticity. He proposed using the displacement of the crack faces as a measure of fracture toughness. The crack opening displacement (COD) is termed the crack tip opening displacement (CTOD) or δ as shown in Figure 2-15.

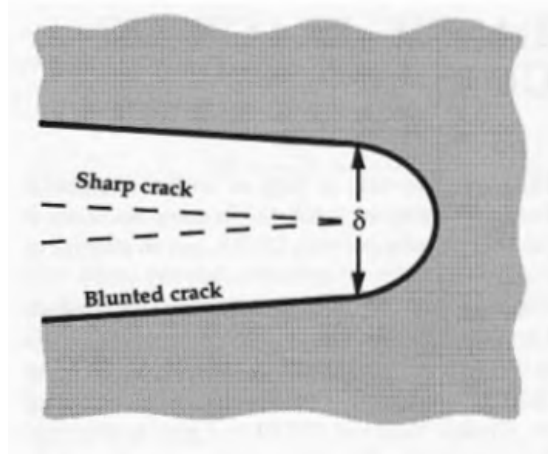


Figure 2-15- Crack Tip Opening Displacement (CTOD). An Initially Sharp Crack Blunts with Plastic Deformation, Resulting in a finite Displacement (δ) at the Crack Tip [10]

Wells performed an approximate analysis relating CTOD to the stress intensity factor at the limit of small scale yielding in plane strain condition showing that::

$$\delta = \frac{K_I^2}{\sigma_0 E} \quad (2.20)$$

In 1966, Burdekin and Stone [22] provided an improved basis for the CTOD. They applied the strip yield model to estimate CTOD for plane stress condition as follows:

$$\delta = \frac{8 \sigma_0 a}{\pi E} \left[\frac{1}{2} \left(\frac{\pi \sigma}{2 \sigma_0} \right)^2 + \frac{1}{12} \left(\frac{\pi \sigma}{2 \sigma_0} \right)^4 + \dots \right] = \frac{K_I^2}{\sigma_0 E} \left[1 + \frac{1}{6} \left(\frac{\pi \sigma}{2 \sigma_0} \right)^2 + \dots \right] \quad (2.21)$$

The Burdekin and Stone equation reduces to the Wells equation (Equation (2.21)) for small scale yielding when $\frac{\sigma}{\sigma_0} \rightarrow 0$.

It should be noted that the above equation assumes the ideal plastic (non-hardening) material behavior. The actual relationship between CTOD and K_I and G depends on the stress state and strain hardening. The more general form of this relationship can be expressed as follows:

$$\delta = \frac{K_I^2}{m \sigma_0 E} = \frac{G}{m \sigma_0} \quad (2.22)$$

where m is a dimensionless constant that is approximately 1 for plane stress, and 2 for plane strain.

There are a number of definitions for CTOD. The two most common are the displacement at the original crack tip, and the 90° interception is shown in Figure 2-16.

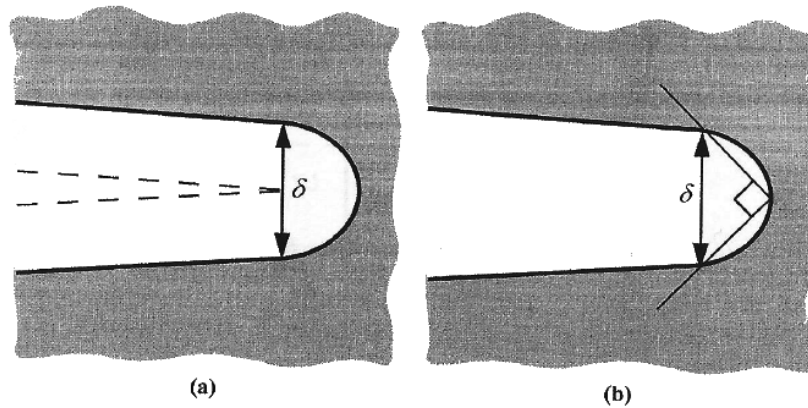


Figure 2-16- Alternative Definitions of CTOD a) Displacement at the Original Crack Tip b) Displacement at the Intersection of a 90° Vertex with the Crack Flanks [10]

Most laboratory measurements of CTOD have been made on SE(B) specimens (Figure 2-17).

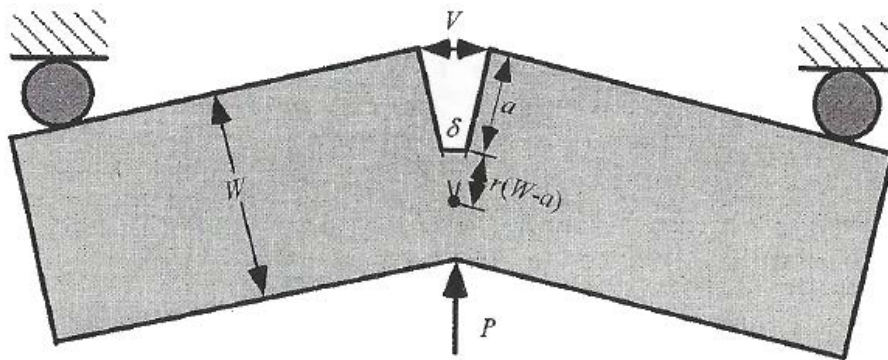


Figure 2-17- The SE(B) Specimen for Estimating CTOD from Three Point Bend Specimen [10]

The crack tip displacement is divided into elastic and plastic components based on ASTM E 1820-11 [8]. A typical load (P) vs. displacement (V) curve from a CTOD test is shown in Figure 2-18. At a given point on the curve, the displacement is divided into elastic and plastic components by constructing a line parallel to the elastic loading line. The CTOD in this specimen is estimated as follows:

$$\delta = \delta_{el} + \delta_{pl} = \frac{K_I^2}{m \sigma_0 E} + \frac{r_p(W - a)V}{r_p(W - a) + a} \quad (2.23)$$

The plastic rotational factor is approximately 0.44 for the typical materials and test specimens.

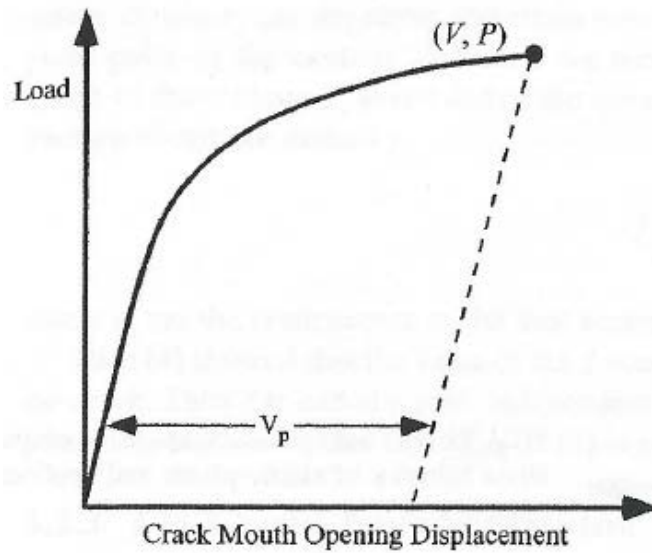


Figure 2-18- Determination of the Plastic Component of the Crack Mouth Opening Displacement [10]

2.1.3.2 The J Contour Integral

In engineering applications where crack extension and fracture take a place, a significant amount of plasticity at the crack tip may occur. In such a case, the J-integral is used. In a formal mathematical concept, the J-integral is defined as the quantity obtained from evaluating an arbitrary counter clockwise path (Γ) around the crack tip (Figure 2-19).

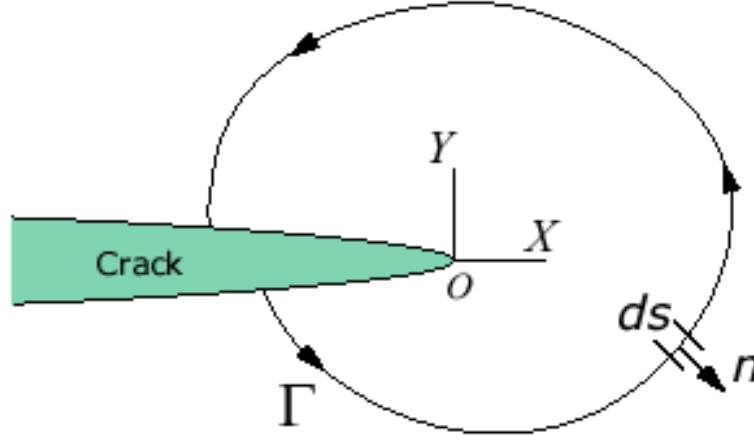


Figure 2-19- Arbitrary Contour around the Tip of a Crack to Characterize J [10]

The J-integral is determined as follows:

$$J = \int_{\Gamma} (w dy - T_i \frac{\partial u_i}{\partial x} ds) \quad (2.24)$$

$$w = \int_0^{\varepsilon_{ij}} \sigma_{ij} d\varepsilon_{ij} \quad (2.25)$$

where σ_{ij} and ε_{ij} are the stress and strain tensors respectively. The traction (T_i) is a stress vector at a given point on the contour. If a free body diagram of the material inside of the contour is constructed, T_i would define the stresses acting at the boundaries. The components of the traction vector are given by:

$$T_i = \sigma_{ij} n_j \quad (2.26)$$

where n_j are components of the unit vector normal to Γ .

The following are important points regarding the J integral [18]:

- 1) J is derived assuming the deformation behavior to be nonlinear, and is not reversible.

Moreover, the energy dissipated cannot be transformed into any other kind of energy.

- 2) It is also worth noting that the assumption of nonlinear elasticity is compatible with actual deformation behavior only if no unloading occurs in any part of the material. But during crack growth the newly formed crack flanks are completely unloaded from stresses as high as the yield strength. Therefore in principle, J is applicable only up to the beginning of crack extension and not for crack growth.

- 3) The total value of J for elastic-plastic behavior of material can be divided into elastic and plastic part as follows:

$$J = J_{el} + J_{pl} \quad (2.27)$$

- 4) The J integral for the linear elastic case is the same as G and for plane stress and plane strain conditions as follows:

$$J = G = \frac{K^2}{E'} \quad (2.28)$$

where $E' = E$ for plane stress and $E' = \frac{E}{1-\nu^2}$ for plane strain condition.

2.1.3.3 Relationship between J and CTOD

In a linear elastic case, $J=G$ and CTOD and K_I are related by Equation (2.22). The relationship between CTOD and J for linear elastic in the plane stress conditions is:

$$\delta = \frac{J}{m\sigma_0} \quad (2.29)$$

Since, the J value in the elastic-plastic material can be divided into elastic and plastic parts, the relationship between CTOD and J can be written based on ASTM E1820-11 [8] as shown in Equation (2.30).

$$\delta = \delta_{el} + \delta_{pl} = \frac{J_{el}}{m\sigma_0} + \frac{J_{pl}}{m\sigma_0} \quad (2.30)$$

2.1.3.4 J as a Stress Intensity Parameter

Hutchinson [23] and Rice and Rosengren [24] independently derived a crack tip stress strain solution for nonlinear elastic materials which became known as the HRR singularity. The HRR solution was derived for materials which show nonlinear hardening behavior (having a power law relationship between plastic strain and stress). If elastic strains are included, this relationship for uniaxial deformation is known as the Ramberg-Osgood equation as follows:

$$\frac{\varepsilon}{\varepsilon_0} = \frac{\sigma}{\sigma_0} + \alpha \left(\frac{\sigma}{\sigma_0} \right)^n \quad (2.31)$$

where α and n are material constants.

The HRR stress and strain fields near the crack tip are:

$$\sigma_{ij} = \sigma_0 \left(\frac{EJ}{\alpha \sigma_0^2 I_n r} \right)^{\frac{1}{n+1}} g_{ij}(n, \theta) \quad (2.32)$$

and

$$\varepsilon_{ij} = \frac{\alpha \sigma_0}{E} \left(\frac{EJ}{\alpha \sigma_0^2 I_n r} \right)^{\frac{n}{n+1}} h_{ij}(n, \theta) \quad (2.33)$$

where I_n is a dimensionless constant that depends on n , and g_{ij} and h_{ij} are dimensionless functions of n and θ . These parameters also depend on the assumed stress state such as plane

stress and plane strain conditions. The J integral defines the amplitude of the HRR singularity, in a similar manner as the stress intensity factor characterizes the amplitude of the linear elastic singularity. Thus J completely describes the conditions within the plastic zone. A structure in small scale yielding has two singularity zones: one in the elastic region, where stress varies as $\frac{1}{\sqrt{r}}$, and the other in the plastic zone where the stress varies as $r^{-\frac{1}{n+1}}$.

2.1.3.5 Effect of Yielding on Crack Tip Stress Fields [25]

Figure 2-20 schematically illustrates the effect of plasticity on the crack tip stresses. Part (a) illustrates small scale yielding behavior where both K and J characterize crack tip conditions. At a short distance from the crack tip, where the crack tip stress and strain fields are described by Equation (2.11) the stress intensity factor completely defines the stresses and strains. This area is controlled by K. Somewhat closer to the crack tip, in the plastic zone, is the J controlled region where Equations (2.32 and (2.33) apply. The small region near the crack tip is the large strain region where the HRR solution is no longer applicable. In small scale yielding, both J and K can characterize the crack tip conditions.

Part (b) illustrates elastic-plastic conditions, where J is still valid, but there is no longer a K field. As the plastic zone size increases around the crack tip, the K controlled region disappears. Therefore, K cannot characterize the crack tip in this case; however, J still is an appropriate fracture criterion. It is worth noting that the size of large strain region in part (b) is much bigger than part (a). The size of this region is approximately 2δ [26]. Part (c) is large strain region where neither K nor J approach is valid.

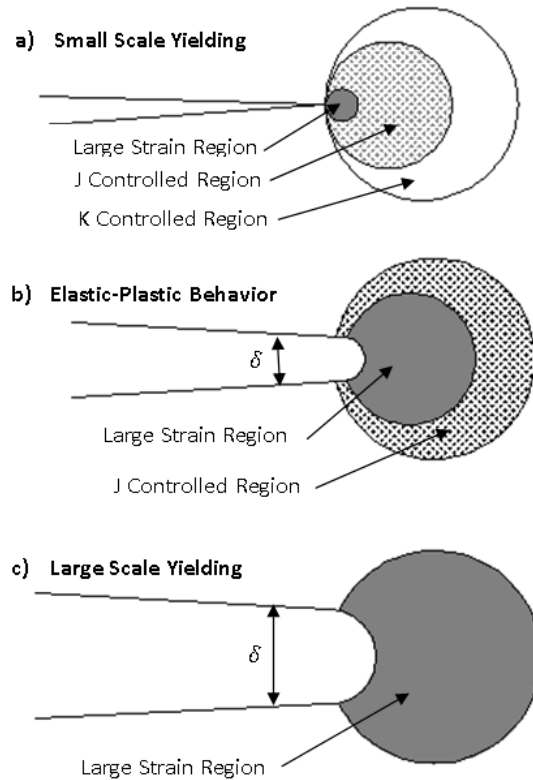


Figure 2-20- Effect of Plasticity on the Crack Tip Stress Fields: a) Small Scale Yielding, b) Elastic-Plastic Conditions, and c) Large-Scale Yielding

2.1.3.6 Crack tip Constraint under Large Scale Yielding

The J integral and CTOD (EPFM) can accommodate significantly more plasticity than linear elastic fracture (LEFM) parameters such as stress intensity. However, elastic-plastic fracture theory cannot be applied where large scale yielding occurs. In such cases, J does not uniquely characterize crack tip conditions, and fracture toughness depends on the size and geometry of the test specimen. Hence, the constraint level dictates the crack tip stresses under fully plastic conditions [27]. As a result K, J or CTOD can no longer be reported as a material property.

Figure 2-21 and Figure 2-22 show crack tip stress fields computed from finite element analysis [28] for a center cracked tension panel and an SENB specimen, respectively. The results are plotted so that all data collapse onto a single curve when the J integral theory is valid. In the

case of the center cracked panel, the computed stresses for large scale yielding lie well below the HRR solution. It is worth noting that the term of $\frac{b\sigma_0}{J}$ shows the distances from the crack tip.

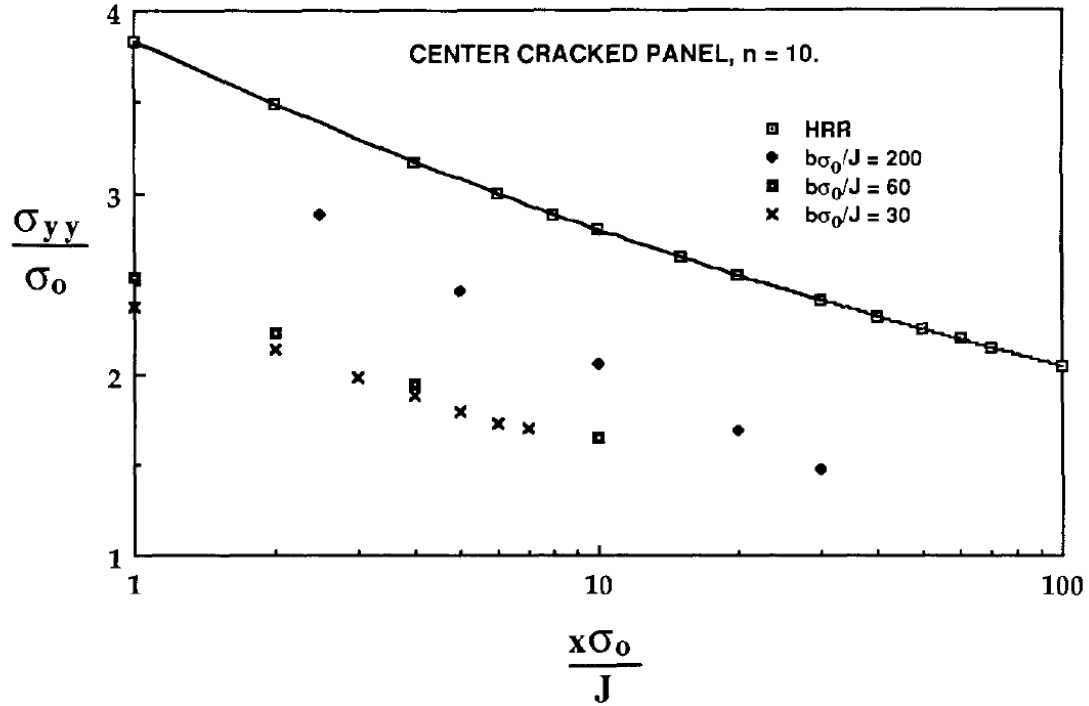


Figure 2-21-Crack Tip Stress Fields for a Center Cracked Panel in Plane Strain with $a/W = 0.75$ and $n = 10$ [29]

The stresses in the edge cracked bend specimen (Figure 2-22) are close to the HRR solution near the crack tip, but diverge at greater distances. Since the stresses at the crack tip control fracture, J is a good parameter in bend specimens up to relatively high levels of plasticity. The ASTM standard for J_{IC} testing [8] states that the ratio $\frac{b\sigma_0}{J}$ must be greater than 25 in order to obtain a valid result from specimens loaded predominately in bending.

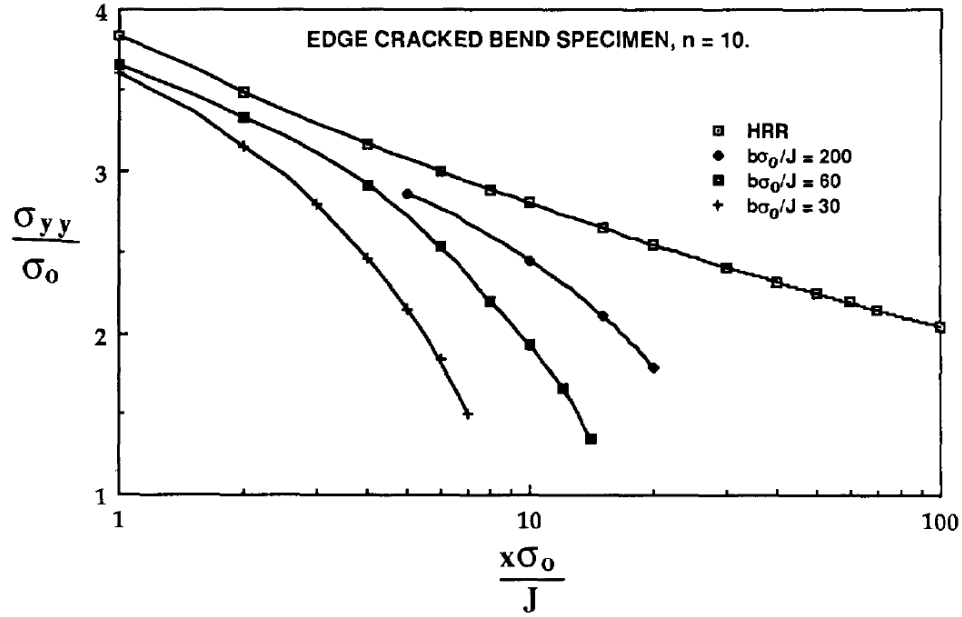


Figure 2-22- Crack Tip Stress Fields for an Edge Cracked Bend Specimen in Plane Strain With $a/W = 0.75$ and $n = 10$ [28]

The above figures confirm that bending loading produces more constraint than tensile loading at the crack tip. When the crack tip conditions are no longer characterized by J , fracture toughness becomes geometry dependent. In addition, a unique relationship between J and CTOD no longer exists. The J -CTOD relationship becomes dependent on the loading and geometry configuration [28].

2.1.3.7 The Elastic T-Stress [10]

Williams [30] showed that the crack tip stress field in an isotropic elastic material can be expressed as an infinite power series (Equation (2.34)), where the first term exhibits $\frac{1}{\sqrt{r}}$ singularity, the second term is constant with r and the third term is proportional to \sqrt{r} . Classical fracture mechanics neglects the second and the third terms. However, it has been shown that [31, 32] also the constant stress contribution acting over a long distance from the crack tip may affect

fracture behavior. The general form of T-stress is the first and second term of Williams's equation as follows:

$$\sigma_{ij} = \frac{K_I}{\sqrt{2\pi r}} f_{ij}(\theta) + \begin{bmatrix} T & 0 & 0 \\ 0 & 0 & 0 \\ 0 & 0 & \nu T \end{bmatrix} + U_{ij}(\theta)\sqrt{r} \quad (2.34)$$

where T and νT are uniform stresses in the x and z directions respectively. Similar to the stress intensity factor, the T-stress depends on the geometry and loading configurations.

Leevers and Randon [32] have shown that T is proportional to the remote stress as follows:

$$\beta = \frac{T\sqrt{\pi a}}{K_I} = \frac{T}{\sigma_m Y} \quad (2.35)$$

where β is the biaxiality ratio and is identical for a specific geometry and loading configuration.

The special case of $T=0$ corresponds to the small scale yielding limit, where the plastic zone is negligible, and the singular term uniquely defines stresses at the crack tip. The negative values of T cause a significant downward shift in the stress fields. Al-Ani and Hancock [33] showed that J alone cannot characterize the stress-strain fields and two parameters T-stress and J are required to characterize the stress-strain fields at the crack tip. They also found that for positive values of T , J still characterizes the stress-strain fields at the crack tip. Since the HRR singularity uniquely characterizes the conditions at the crack tip.

2.1.3.8 The J-Q Approach

O'Dowd and Shih [34, 35] proposed the J-Q theory to quantify the constraint level under fully plastic conditions where the Q stress represents the state of triaxial stress at the crack tip. They

approximated a different stress field within the circular area with the radius of $1 < \frac{r\sigma_0}{J} < 5$, ahead of the crack tip as follows:

$$\sigma_{ij} = \sigma_{ij}^{ref} + Q\sigma_{ij}\delta_{ij} \quad (2.36)$$

O'Dowd and Shih [36] showed that the Q-field corresponds to a uniform hydrostatic stress field, and Q as a constraint parameter that can be estimated as follows:

$$Q = \frac{\sigma_{yy} - (\sigma_{yy})_{T=0}}{\sigma_0} \text{ at } \theta = 0 \text{ and } \frac{r\sigma_0}{J} = 2 \quad (2.37)$$

The Q parameter, like the T-stress, has been applied to characterize the geometry dependent constraint. Both quantities affect the hydrostatic stress in the same way. Negative values of Q and T-stress lower, whereas positive values raise the hydrostatic stress [37].

The constraint levels that occur in different fracture mechanics test specimens [36, 38] were investigated and are shown schematically in Figure 2-23. This figure shows K_{IC} and J_{IC} as a function of the constraint (Q or T-stress). The specimens with higher constraint such as three point bending show a lower fracture toughness whereas a center-cracked tensile specimen which has low constraint give a higher fracture toughness [37]. As a result, the test data of J_{IC} and J-R curves are generally geometry dependent. Therefore, the constraint effects on the J-R curves due to specimen geometry must be considered. This confirms the need for simple and efficient constraint estimation procedures for assessing a crack flaw. Figure 2-23 shows the fracture toughness as function of constraint. The red circle in Figure 2-23 shows the crack depth has an effect on the constraint and fracture toughness value as well.

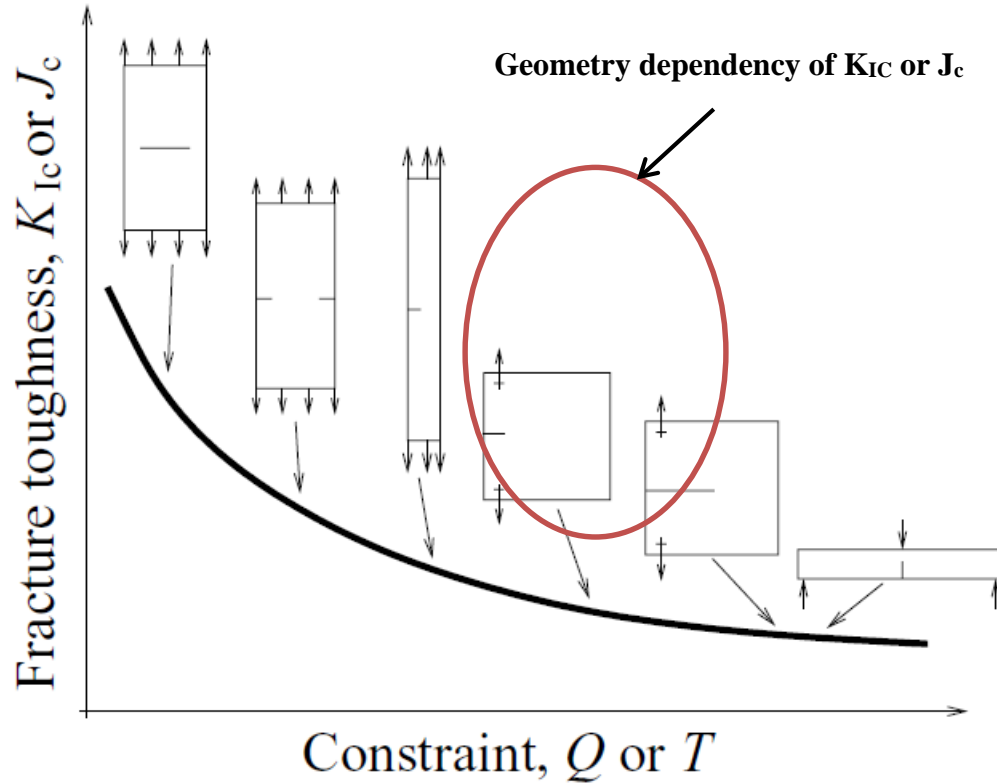


Figure 2-23- Schematic Showing the Experimental Test Data of Fracture Toughness as a Function of the Constraint [37]

2.1.3.9 The J-R Curves Correction [39]

The standard J-R curve is a plot of the J-integral versus crack extension within the region of J-controlled growth. It is size and geometry independent when using ASTM fracture test standard E 1820-11 [8]. For nonstandard fracture specimens, the J-R curves could be size and geometry dependent due to large scale yielding through the ligament, when there is not enough constraint around the crack tip and the J value becomes dependent on the specimen size.

In general, the fracture toughness J_{IC} and J-R curve of a material could be functions of test specimen geometry, size, thickness and loading configuration. To investigate the crack-tip constraint effects on the fracture properties of ductile growing cracks, a large number of nonstandard fracture specimens have been proposed and analyzed. Hancock et al. [40] obtained

the fracture toughness J_{IC} and J-R curves for SENB, CT, center cracked panel (CCP) and surface cracked panel specimens with various depth cracks in using ASTM 710 Grade A steel. Joyce and Link [41, 42] presented experimental data of ductile crack extension for CT, SENB, single edge-notched tensile (SENT) specimens, and double edge-cracked plate (DECP) with shallow to deep cracks in different structural steels. These investigators found no significant constraint effects on the corresponding to crack initiation toughness, but observed a larger constraint effect on the J-R curve after a relatively large amount of crack growth. The same experimental results were observed from ductile crack extension experiments by Marschall et al. [43], Eisele et al. [44], and Roos et al. [45] for large-sized fracture specimens, and by Elliot et al. [46], Alexander [47], Yoon et al. [48] for sub-sized fracture specimens.

In general, the J-T theory has only limited use in elastic-plastic fracture analysis because it is based on the elasticity theory. The J-Q theory is a common approach for characterizing the constraint effect under large scale yielding [49]. The J-Q approach also has been applied for analyzing the constraint effect in stationary crack growth [50-52]. However, this theory has a restriction for ductile crack growth because the constraint parameter, Q , depends on the loading configuration. Therefore Zhu et al [39] proposed the modified constraint parameter, Q^* , instead of Q in the J-Q theory whereby Q^* is load independent, given Q^* as follows:

$$Q^* = \left[\frac{J}{\alpha \sigma_0 I_n \varepsilon_0 L} \right]^{\frac{-1}{n+1}} Q_{HRR} \quad \text{at } \theta = 0 \quad \text{and} \quad \frac{r\sigma_0}{J} = 2 \quad (2.38)$$

Figure 2-24 shows the J- Q^* controlled region is much larger than the J-controlled region. The larger region on front of the crack tip can be characterized by applying the J- Q^* theory (Figure 2-24).

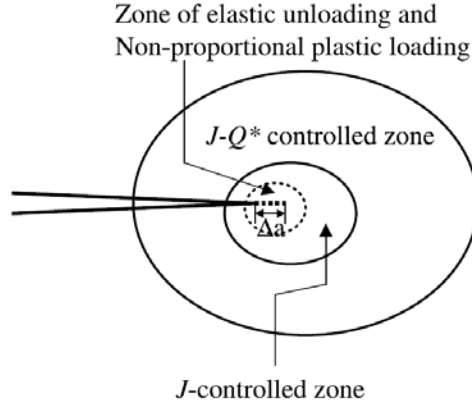


Figure 2-24-J and J-Q* Controlled Zones in Ductile Crack Growth [39]

2.2 Plastic Collapse Concept

In general, structures made from ductile materials, having a higher toughness, may fail by plastic collapse if they are overloaded.

2.2.1 Net Section Yield Load [53]

The net section yield load F_Y and reference stress (σ_{ref}^P) are defined as follows:

$$L_r = \frac{F}{F_Y} = \frac{\sigma_{ref}^P}{\sigma_0} \quad (2.39)$$

The result, whether a critical load or a critical crack size, is significantly dependent on the of the yield load. Unfortunately, the available yield load solutions vary greatly since they have been obtained over the past years by different methods which give different results for the same crack geometry [5].

In the past, limit loads were generally determined as maximum loads that a given structure made of perfectly plastic material could sustain. When such a limit load is reached the deformation becomes unbounded. However, engineering materials usually show some hardening

and not perfectly plastic deformation behavior. As a consequence a distinction should be made between two limiting criteria:

(a) The load at which the whole ligament becomes plastic. This is roughly correlated with the load above which the load-deformation characteristic of the component section becomes non-linear named the yield load.

(b) The load at which the component fails due to plastic collapse. This limit load (plastic collapse) is higher than the yield load and is designated as the plastic collapse load. It should be noted that the yielding load for non-hardening materials is equal to the limit load. However, materials experiencing hardening show two limit states: one when yielding spreads over the whole ligament, and a second at which the maximum load is reached and the component fails. Therefore, the yield load and plastic collapse load are different in these hardening materials.

Many yield load solutions are determined as limit loads based in a perfectly plastic material with a limiting stress equal to the yield strength. In contrast, the plastic collapse load is determined as the limit load for a perfectly plastic material with a limiting stress equal to the flow stress, σ_f , which is usually defined as the average of the yield and tensile strengths as follows:

$$\sigma_f = \frac{\sigma_0 + \sigma_U}{2} \quad (2.40)$$

The effect of material work hardening is considered approximately by applying the flow stress.

Traditionally, solutions are obtained by two bounding theorems as follows:

(a) A lower bound, characterised by a statically admissible stress field that satisfies equilibrium and yield.

- (b) An upper bound, based on a kinematically admissible strain-rate field satisfying compatibility and the flow rule [54].

The yield load solutions are commonly generated for plane strain or plane stress considerations and the Tresca or von Mises yield criteria. As a rule, the lowest values are obtained for the lower-bound theorem, plane stress and Tresca's criterion, whereas the highest values refer to the upper-bound theorem, plane strain conditions and the von Mises criterion [54].

Recent yield load solutions are often based on finite element analyses [55, 56]. This is advantageous with respect to the possibility of three dimensional analyses, the treatment of complex structures and a yield load definition closer to real conditions [53]

2.2.2 Global versus Local Collapse

A structure may fail by global or local plastic collapse. The term global refers to the entire structure including the cross section containing the crack, whereas local plastic collapse refers to a defined local region in the ligament ahead of the crack. In general, the local failure load is lower than that for global collapse. It should be noted that local collapse for a pressure vessel would not lead to the total failure of a cracked component. However, it may lead to leakage prior to the plastic collapse.

Global collapse is typically predicted by determination of material non-linearity in the ligament. As plasticity spreads in finite element model, the material non-linearity behavior increases. Eventually, the strain in the model becomes extremely large for a small increment. This situation causes numerical instability of the model due the number of unsuccessful iterations. This corresponds to the necking of the cross section of the part.

2.3 Material Characterization

2.3.1 Tensile Test [5]

Uniaxial tensile testing is a fundamental material test used to measure the stress-strain response of a material, which can be used with a yield theory to predict how a material will react under different types of loading, such as biaxial loading or in the presence of stress concentrations. Typical mechanical properties include the yield strength, ultimate strength and strain hardening parameters (ASTM E 8M-09) [57]. Tests can be undertaken using samples oriented along the length of the pipe or in the circumferential direction, where the circumferential properties have been shown to provide better estimates of the collapse pressure [58]. Pipeline materials generally exhibit anisotropy in the longitudinal and circumferential directions.

Twelve longitudinal and twelve circumferential pipe samples were tested based on the ASTM (E 8M-07) procedure conducted in the previous work [5]. The thickness of the specimens was 5.7 mm, the same as wall thickness of the pipe, and the width was 12.5 mm. The average values of yield strength, and true ultimate strength in the circumferential direction, which were used in the assessment methods, were 431 MPa and 618 MPa respectively. The standard deviations for yield strength and true ultimate strength were 24.2 MPa and 17.5 MPa respectively. The Ramberg-Osgood constants coefficients (α and n) were calculated to be 2.29 and 7.31 respectively.

2.3.2 Charpy Test [5]

The Charpy impact test [59] was traditionally used for evaluating material resistance to fracture. In the absence of fracture toughness data from traditional K_{IC} or J_{IC} tests, Charpy data

has been correlated to fracture toughness. This test measures the energy absorption of a Charpy V-Notch (CVN) specimen while breaking under impact bending.

The primary factors affecting the measured energy include temperature and the specimen dimensions. The standard sample thickness is 10mm (ASTM E23) [59]. Since the thickness of typical pipe material does not allow testing full-size specimens; sub size specimens are used and the results scaled to full-size samples. There is no direct correlation between sub-size and full-size Charpy specimens for impact energy in pipeline materials. However, the following equation was suggested for upper shelf and lower shelf energies according to API 579 [1] for scaling the impact energy to full-size specimens:

$$CVN = CVN^S \left(\frac{t_c}{t_s} \right) \quad (2.41)$$

2.3.2.1 K_{IC} -CVN Correlation

The following methods were studied in this work to correlate the CVN impact upper bound to K_{IC} :

API 579 [3] applied the Rolfe-Novak equation which can be used for the upper bound fracture toughness. It should be noted that this equation generally gives conservative results..

$$\left(\frac{K_{IC}}{\sigma_0} \right)^2 = 0.52 \left(\frac{CVN}{\sigma_0} - 0.02 \right) \text{ (ksi(in)}^{0.5}, \text{ksi,ft-lb)} \quad (2.42)$$

CorLAS [4] is a computer program for corrosion-life assessment of pressurized pipes and vessels. The following empirical equation can be used for converting Charpy impact energy to J_c for the upper bound values:

$$J_c = 10 \text{ CVN at } (ft - lb)/(in^2) \quad (2.43)$$

It is worth noting that Equation (2.43) gives the lower bound value of the upper shelf fracture toughness. In other words, it provides conservative results.

Mak and Tyson [9] investigated the material properties of eight different pipes manufactured from 1952 to 1981. The pipes grades were X52, X65, and X70 and the thickness of the pipes ranged from 7.9 to 12.7 mm and all of the pipes exhibited ductile tearing. The reported CVN upper shelf energies (43.5 J) were used by Mak and Tyson (Figure 2-25 digitized by Badr Bedairi [60]).

It should be noted that the pipe wall thickness in the present work was 5.7 mm (less than the pipe wall thickness for the Mak and Tyson study) and was considered a thin-wall pipe. Therefore, the results are an approximation of the actual fracture value. Figure 2-25 was digitized by Badr Bedairi [60].

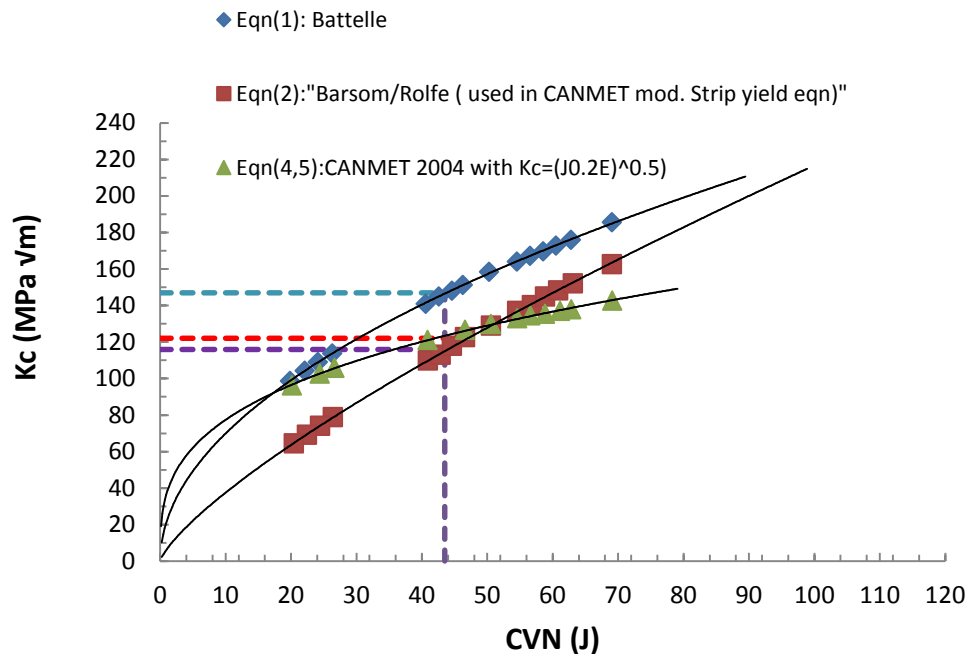


Figure 2-25- CVN vs. K_{IC} (Tyson 2005) [60]

The BS 7910 [2] recommends Equation (2.44) which can be used for the lower bound of upper shelf fracture toughness of pipeline materials. The Equation is plotted in Figure 2-26.

$$K_{mat} = 17 CVN + 1740 \quad (2.44)$$

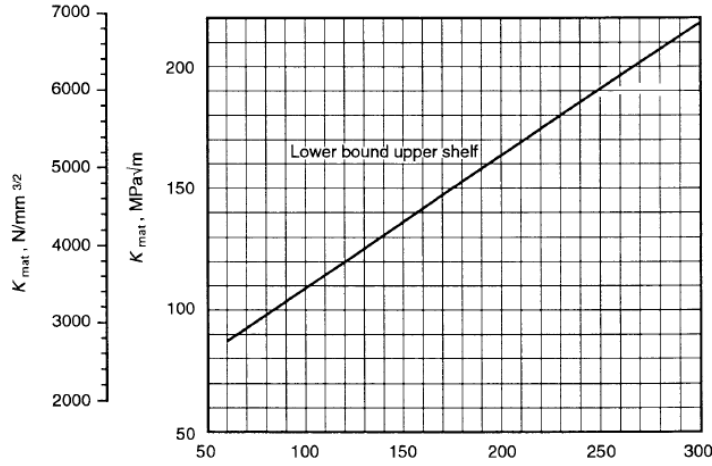


Figure 2-26- K_{mat} Plotted against Charpy Impact Energy for Upper Shelf Behavior [2]

In the previous work [5], a set of 108 sub-size Charpy impact specimens (ASTM-E23-07 [59]) were machined from four different sections of the pipe, and tested at eight different temperatures (-60,-40,-20, 3, 22, 50, 100 and 150 °C) (Figure 2-27). Equation (2.41) was applied to scale the impact energy to full-size specimens.

The average upper shelf energy corresponding to completely ductile fracture was 43.5(J), calculated using a sigmoidal curve (Figure 2-27).

In the absence of direct toughness measurements, this upper shelf energy was used to estimate the fracture toughness (K_{IC}). For example, the estimated fracture toughness was $89\text{MPa}\sqrt{\text{m}}$ using the API 579 Appendix F K_{IC} correlation for Level II and Level 3 analyses. Similarly, using the relationship proposed by Mak and Tyson [9], the J_{IC} value was estimated from the Charpy data to be 97 kJ/m^2 .

Table 2-1- Charpy Test Results (scaled to full size equivalent using Equation (2.41) [5])

Temperature (°C)	-60	-40	-20	3	22	50	100	150
Average Energy E (Joules)	10.1	11.5	19.2	37.1	42.1	43.1	43.2	43.2
Percent Shear (%)	0	10	40	60	85	95	100	100

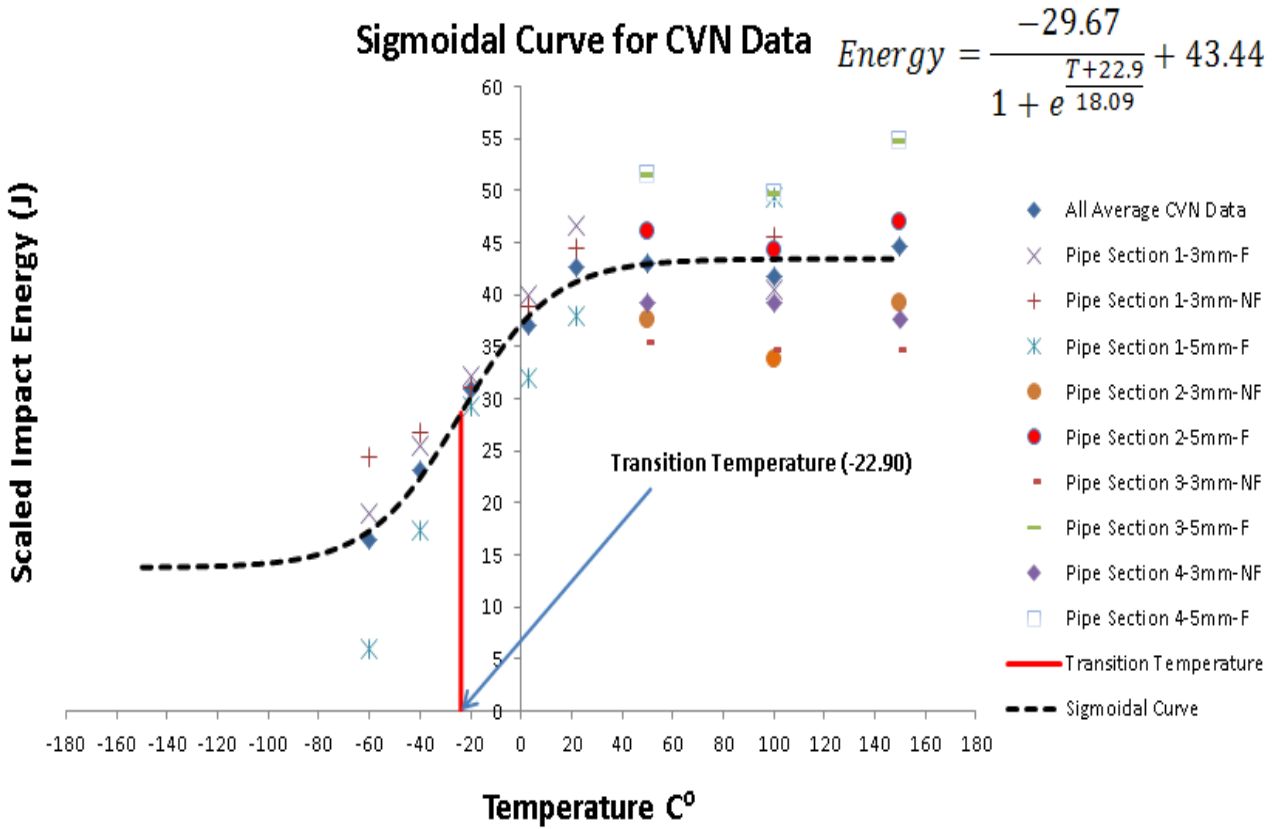


Figure 2-27- Scaled Energy Chart [5]

Table 2-2 summarizes the above methods for correlating Charpy impact energy to the fracture toughness.

Table 2-2- Charpy Impact Energy Correlation to Fracture Toughness in Different Methods

Methods	Charpy	Upper	Fracture
	Shelf	Average	Toughness
	Energy E (J)		($MPa\sqrt{m}$)
API 579	43.5		89.0
CorLAS	43.5		108.0
Tyson & CANMET	43.5		128.0
BS 7910	43.5		80.0

2.3.3 Fracture Toughness Test, Values and Trends

Fracture toughness is considered a unique material property; however, for different test conditions and test sample sizes, the same materials may have different apparent values. For example, the fracture toughness of aluminum foil (Al) and low density polyethylene (LDPE) [61-63] has been studied and shown to be much lower than that given in standard material handbooks. Therefore, a fracture toughness test was suggested [61-63] for these types of materials. Most often, it may not be possible to evaluate the fracture behavior of a specimen or a component for the purpose of assessment of its structural integrity using standard ASTM test techniques. This is because of the requirements of the ASTM test methods for specifying the plane strain conditions at the crack tip. Hence, these geometry and loading conditions restrict the application of fracture mechanics for obtaining valid fracture parameters for these materials. A number of test techniques have been proposed in the literature [64-68] but none of them satisfy the ASTM requirements.

The fracture toughness of material taken from the walls of cylinders or tubes is required to assess flaws. The fracture mechanics tests are not well suited to measuring the fracture toughness

of tubular materials. Two methods can be used to investigate the resistance to crack propagation in the axial direction. The first method consists of machining small compact tension (CT) samples out of large thickness and diameter samples. However, these results cannot be extrapolated to thin walled tubes [69]. The second method consists of cutting specimens out of previously flattened tubes. The results can be questioned owing to possible microstructure changes, internal stress redistribution and strain hardening [69]. It would be preferable to test the tubular element as a whole, but this is often not feasible. Others researchers, for example Evans et al [70] designed a specimen which was machined from the cylinder wall so that the crack front was parallel to the radial direction. The inner and outer surfaces of the cylinder composed the side surfaces of the specimen. Moreover, Samal et al [71] designed a pin-loading tension test (PLT) which required geometric functions for evaluation of the stress intensity from the experimental data. These geometries do not conform to the ASTM standard and hence, the parameters mentioned above [69, 70] are usually not available.

A fracture toughness test measures the resistance of a material to crack extension. Such a test may yield either a single value of fracture toughness or a resistance curve, where a toughness parameter such as K_{IC} , J_{IC} , or crack tip opening displacement (CTOD) is plotted against crack extension. A variety of organizations have published standardized procedures for fracture toughness measurements, including the American Society for Testing and Materials (ASTM) [8], the British Standards Institution (BSI) [72], the International Institute of Standards (ISO) and the Japan Society of Mechanical Engineers (JSME). The first standards for K_{IC} and J_{IC} testing were developed by ASTM in 1970 and 1981, respectively, while BSI published the first CTOD test method in 1979. Existing fracture toughness standards include procedures for K_{IC} , K-R curve, J_{IC} and J-R curves [8].

The recommended specimens (Figure 2-28) are compact [C (T)], single-edge bend [SE (B)], and disk-shaped compact [DC (T)]. All specimens contain notches and sharp fatigue cracks.

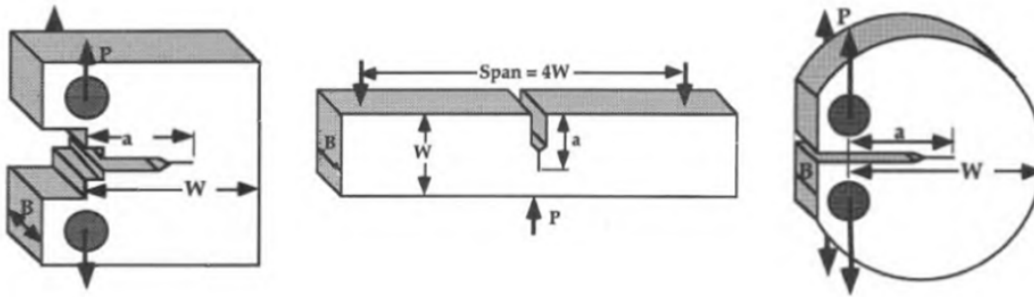


Figure 2-28- Standardized Fracture Mechanics Test Specimens [10]

The specimens include a machined notch with a pre-fatigue crack. Growth of the crack is detected by observing the force (P) versus displacement (v_g) using a clip gauge mounted across the mouth of the notch. A deviation from linearity on the P_c - v_g plot, or sudden drop in force due to crack extension, identifies a point of P_Q corresponding to an early stage of crack extension. The value of K , denoted K_Q , is then calculated for this point.

2.3.3.1 J-Integral Test [5]

EPFM approaches require a relevant measure of fracture toughness, such as ductile tearing or J-testing (ASTM-E1820-11). Experimental tests to measure J and the corresponding critical value (e.g. J_{IC} , corresponding to large yielding with crack extension) use a fatigue pre-cracked sample that is loaded, resulting in stable or unstable crack growth. For the measured load-displacement data, the area under the curve corresponds to the energy required for the crack propagation (Figure 2-29).

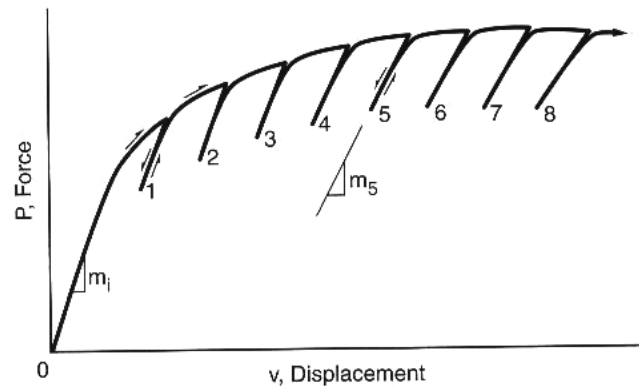


Figure 2-29- Force vs. Displacement Curve during an Elastic-Plastic Fracture Toughness Test [15]

Samples from 3 pipe sections were tested. J was calculated using an incremental procedure based on the current crack length, $a=a_i+\Delta a$, and area A_{pl} . Values of J were then plotted with the corresponding crack extension, Δa , to create the resistance (R) curve (Figure 2-30).

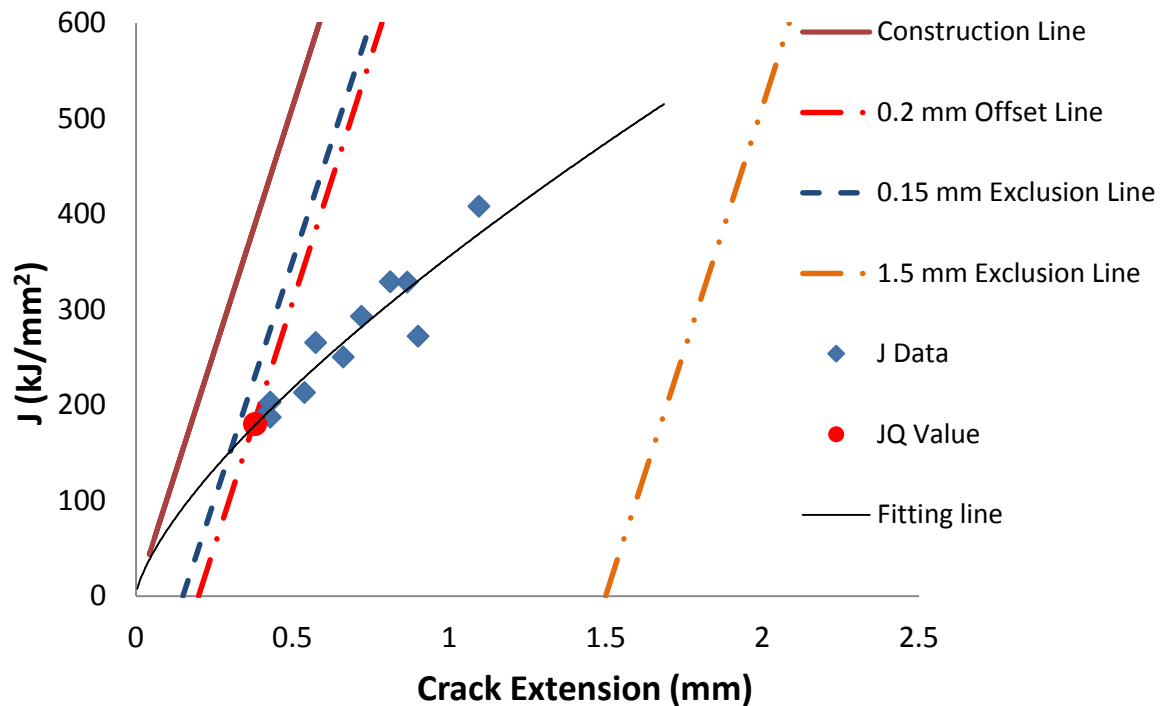


Figure 2-30- J-Integral Example Test Result for One Pipe Section

Considering the elastic and plastic components of J :

$$J = J_{el} + J_{pl} \quad (2.45)$$

$$J_{el} = \frac{K_I^2(1-\nu^2)}{E} \quad (2.46)$$

The elastic term J_{el} is calculated from the stress intensity (K) at the crack resulting from the applied load:

$$K = \frac{P}{\sqrt{tW}} f\left(\frac{a}{W}\right) \quad (2.47)$$

The plastic portion of the J integral (J_{pl}) is given by:

$$J_{pl} = \frac{\eta A_{pl}}{t(b-a)} \quad (2.48)$$

where a is the crack length, b is the remaining ligament and t is the specimen thickness. For a test sample in bending, $\eta=1.9$.

Local plastic deformation at the crack tip prior to growth causes blunting represented by the blunting line (Equation (2.49)).

$$\frac{J}{\Delta a} = 2\sigma_y \quad (2.49)$$

Figure 2-30 shows a typical J-Integral resistance curve. The construction lines (Figure 2-30) are plotted parallel to the blunting line. The second and forth lines drawn from 0.15 and 1.5 mm on the x-axis are the exclusion lines, and only those points that fall inside these lines can be used to determine J_{IC} . The third line (0.2 mm offset line) is used to define J_Q by intersection with the resistance curve. If J_Q meets the size requirement, then it is considered as J_{IC} . Finally, the value of J at 0.2 mm crack growth ($J_{0.2}$) can be measured by intersection of vertical line from 0.2 mm with the resistance curve.

$$t, (b - a) > 25 \left(\frac{J}{\sigma_y} \right) \quad (2.50)$$

Of particular interest are cracks that originate on the pipe wall, typically oriented along the length of the pipe, perpendicular to the hoop or circumferential stress and growing through the thickness of the pipe. Test samples with cracks oriented in this direction failed to meet the requirements of Equation (2.50), consequently J_Q was calculated, an approximation of J_{IC} . Further, when the sample thickness is not sufficient, the measured J value will be higher than that measured using a full-size sample. This is due to the greater extent of plastic deformation in the vicinity of the crack leading to higher J values. However, it is considered that this higher material value will directly relate to the behavior of the actual pipe material since it is the same thickness and the predicted collapse pressure will be in agreement with the measured failure pressure.

For the current study, the cracks in the test samples were oriented in the same direction as surface flaws in the operating pipe. The variation in thickness of the test samples (5.30 mm, 5.12 mm and 5.33 mm) was due to minor surface corrosion which was removed when the samples were machined, and the specimen length and width were the same for the test samples. Since the sample thickness was small, extensive plasticity occurred and the results did not meet the requirements for J_{IC} . Therefore, the resistance curve, J vs. crack extension Δa (Figure 2-30) was used to determine J_Q [73]. The measured values of J_Q were 215, 197 and 180 kJ/m² with an average of 197 kJ/m², which is higher than the value of 97 kJ/m² predicted by the Mak and Tyson Charpy energy correlation [12], based on experimental tests from eight pipe materials comprising X52, X65 and X70 with thicknesses ranging from 7.9 to 12.7 mm.

2.3.3.2 Trends in K_{IC} with Temperature and Loading Rate

Fracture toughness generally increases with temperature. An especially abrupt change in toughness over a relatively small temperature range occurs in metals with a BCC crystal structure, notably in steels with ferritic-pearlitic and martensite structures. The temperature region where the rapid transition occurs varies considerably for different steels, shown in Figure 2-31. There is usually a lower shelf of approximately constant K_{IC} below the transition region, and an upper shelf above it, corresponding to a higher approximately constant K_{IC}. It should be noted that just one set of data in Figure 2-31 covers a sufficient range to exhibit an upper shelf.

The statistical variation in fracture toughness is especially large within the temperature transition region. In fact, the position of the transition may shift by as much as 50 °C for different batches of the same steel [15] as shown in Figure 2-31.

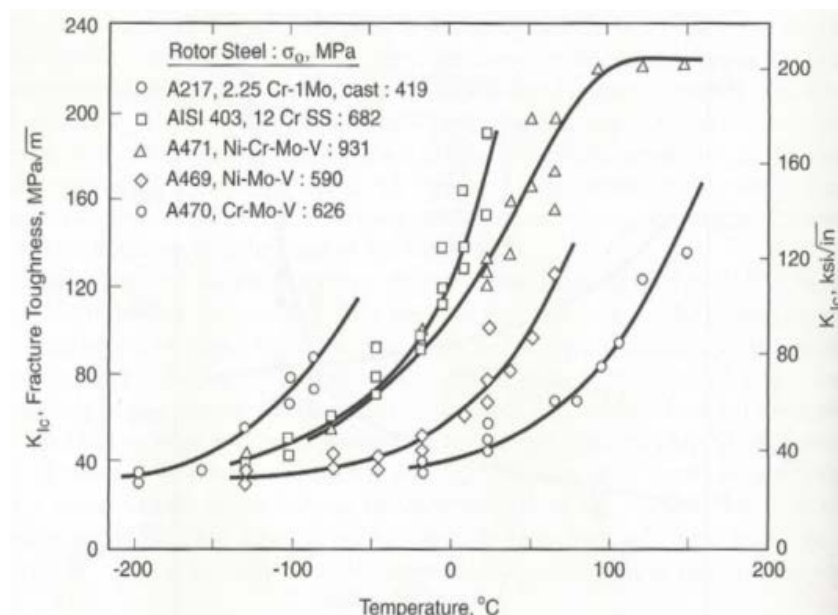


Figure 2-31- Fracture Toughness vs. Temperature for Different Steels [15]

A higher rate of loading usually lowers the fracture toughness same as a decrease in the temperature.

2.3.3.3 K_{IC} Variations with Material Thickness and Yield Strength

The measured fracture toughness may have different values based on different test types and sample sizes, with the most important parameter being specimen thickness [19]. The thickness of material is an important parameter between the state of plane stress and plane strain, and the fracture toughness value in these two states is very different. Many tests indicate that the fracture toughness value decreases gradually with increasing specimen thickness and reaches a constant value K_{IC} . The relation between the sample thickness and its fracture toughness is shown in Figure 2-32. When the plate thickness t is less than t_0 , the fracture toughness rises rapidly with increasing thickness. When t is equal to t_0 , the fracture toughness reaches the largest value K_{iC} , which is normally considered as the plane stress fracture toughness, and decreases for greater thickness values. When t is greater than t_1 , fracture toughness is approximately constant (K_{IC}), which is considered the plane strain fracture toughness. Usually, the plate thickness t is either $t_0 < t < t_1$ or $t > t_1$, so the value of fracture toughness falls between K_{iC} and K_{IC} . The effect of thickness on fracture toughness in typical carbon steel is shown in Figure 2-32.

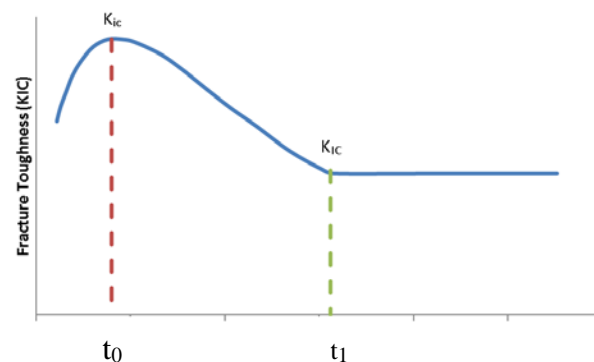


Figure 2-32- Effect of Thickness on Fracture Toughness

When the plastic zone is large compared with the specimen thickness (plane stress), the effect of thickness is more obvious, because the crack tip has a large plastic zone in the plane stress state. Therefore, the resistance for crack propagation is large, and the corresponding fracture toughness is also large. When the plastic zone is small compared with the specimen thickness, fracture toughness of a specimen is not affected by thickness (plane strain). In other words, when the specimen thickness reaches a certain value, the size of the plastic zone is far smaller than the plate thickness, and the corresponding fracture toughness does not vary with the thickness.

In general, when the thickness of specimens obeys the following relationship involving the yield strength, no further decrease in fracture toughness value is expected, and the value is considered the plane strain fracture toughness.

$$t \geq 2.5 \left(\frac{K_{IC}}{\sigma_0} \right)^2 \quad (2.51)$$

Values of K_{IC} for pipeline materials are generally in the range 20 to 200 $\text{MPa}\sqrt{m}$ [15] where fracture toughness typically decreases with increasing yield strength.

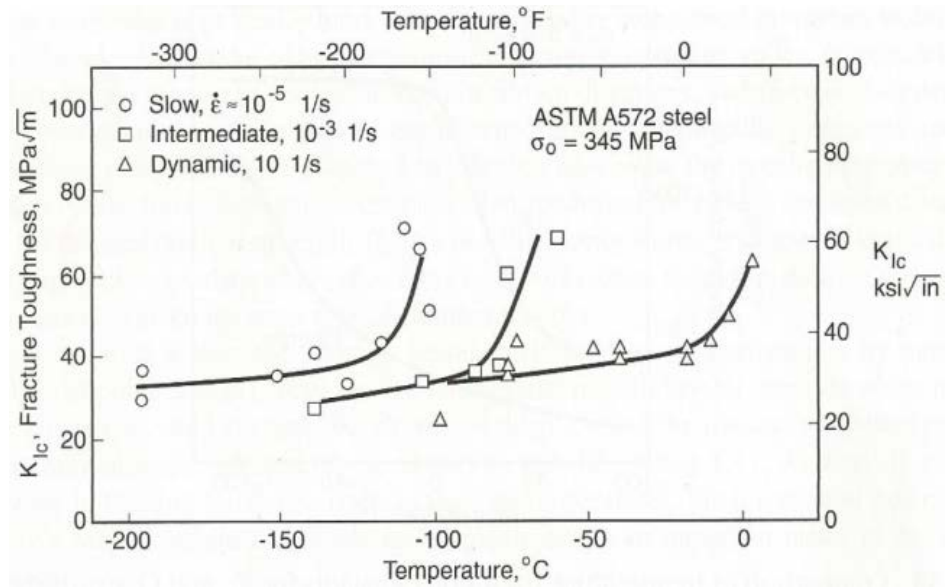


Figure 2-33- Effect of Loading Rate on the Fracture Toughness of a Structural Steel [15]

It is worth noting that the transition temperatures of Charpy and K_{IC} tests are different for the same steel (Figure 2-34). This is due to the Charpy test is in a higher rate of loading in comparison to the K_{IC} test.

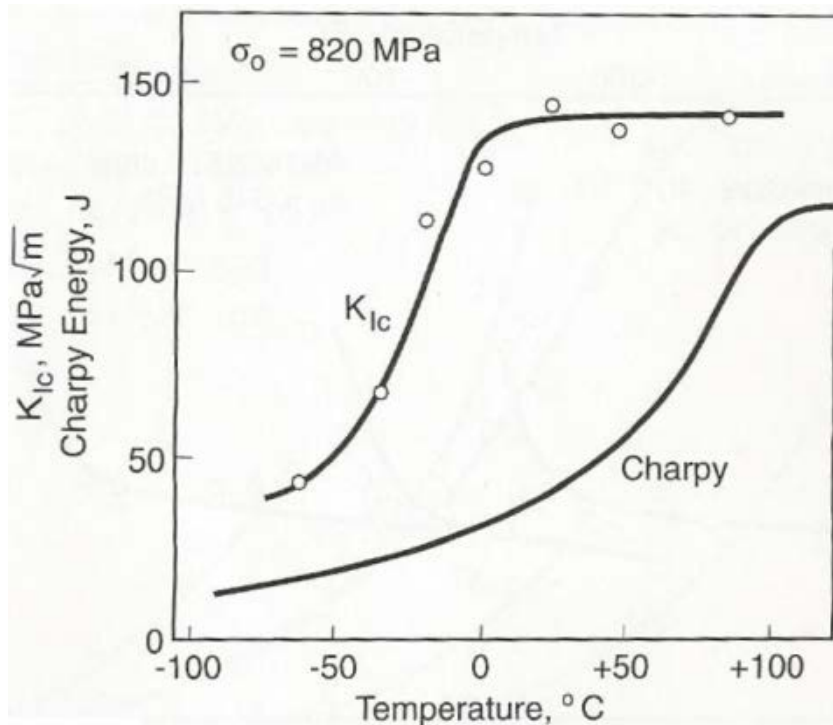


Figure 2-34- Comparison of Temperature-Transition Behaviors for K_{IC} and Charpy Test on a Same Steel [15]

2.4 Flaw Assessment Methods [5]

2.4.1 Corrosion Flaw Assessment

Corrosion is the degradation of the material due to chemical or electrochemical interactions with their environments. Corrosion can be categorized in different classes such as pitting, general corrosion, erosion corrosion or crevice corrosion.

Corrosion may occur on the outside of a pipe due to coating failure. Corrosion can also occur on the internal surface of the pipeline caused by contaminants in the products such as small sand particles or amino acids [3].



Figure 2-35- A Corroded Pipe Section

There are parameters, which have been recognized as having significant effect in the remaining strength of corroded pipe. The parameters in order of significance are as follows [74]:

- Internal pressure
- Pipe diameter
- Wall thickness/flaw depth
- Flaw length/width
- Ultimate strength
- Yield strength/strain hardening characteristics
- Fracture (Charpy) toughness

It should be noted that the fracture toughness properties of new pipeline materials are high, therefore, this parameter does not generally play a significant role in failure of corroded pipes [75].

The following methods have been developed for predicting the burst pressures on blunt flaws, which characterise the behavior of typical corrosion flaws. All of these methods are primarily

concerned with the longitudinal extent of the corroded area and internal pressure loading. The older methods are based on the original Battelle part-wall failure criterion (the NG-18 equations), whereas the more recent methods have been developed from extensive numerical studies validated against test data.

These methods are listed as follows:

- 1) ASME B 31G [76]
- 2) Modified B 31G [77]
- 3) RSTRENG [77]
- 4) Shell 92 [78]
- 5) PCORRC [79, 80]
- 6) CPS [58]

RSTRENG [3] is the most commonly used method in industry. However, a more recent methods such as Corroded Pipe Strength (CPS) [58] provides improved failure pressure predictions. Most existing methods consider that the circumferential or hoop stress in the pipe dominates the response and estimates the collapse pressure based on the area of metal loss.

The RSTRENG method is based on the NG-18 equation to predict failure of part-wall flaws in pipe. RSTRENG is generally regarded as a conservative method for predicting the remaining strength of externally corroded pipe. However, it is less conservative than other methods, such as the original B31G or Modified B31G approaches [3]. The main improvements in RSTRENG compared to the other methods include improved representation of the metal loss area [75], and a more accurate estimate of the material flow stress (Figure 2-36).

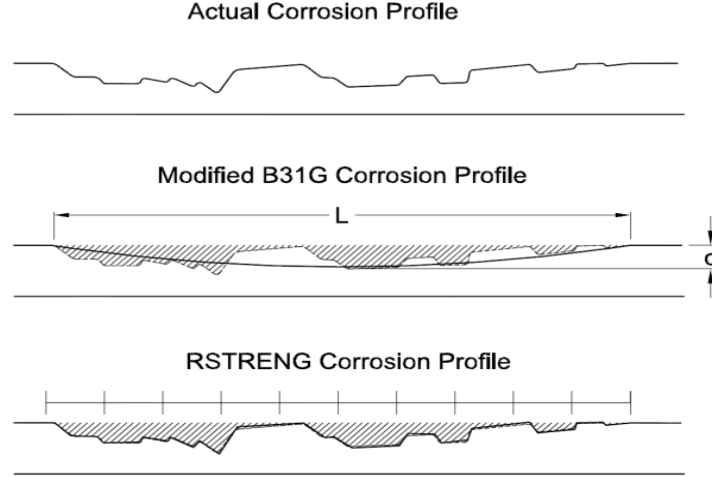


Figure 2-36- Corrosion Flaw Profile

The NG-18 surface flaw equation expresses the relation between flow stress, bulging (Folias) factor (M), and flaw geometry as follows:

$$\sigma_{\theta} = \bar{\sigma} \left[\frac{1 - \frac{d}{t}}{1 - \left(\frac{d}{t}\right)\frac{1}{M}} \right] \quad (2.52)$$

For RSTRENG, the flow stress $\bar{\sigma}$ is estimated by using:

$$\bar{\sigma} = \sigma_0 + 69.8 \text{ (MPa)} \quad (2.53)$$

The Folias factor (M) (Equation (2.54)) describes the bulging effect of a shell surface that is thinner in wall thickness than the surrounding shell.

$$M = \sqrt{1 + 0.6275 \left(\frac{2c}{\sqrt{Dt}} \right)^2 - 0.003375 \left(\frac{2c}{\sqrt{Dt}} \right)^4} \quad (2.54)$$

The failure stress of a corroded pipe under internal pressure containing a corrosion flaw oriented along the axis of the pipe is given as follows:

$$P_f = \left(\frac{t}{R}\right) \bar{\sigma} \left[\frac{1 - \frac{d}{t}}{1 - \left(\frac{d}{t}\right)^{\frac{1}{M}}} \right] \quad (2.55)$$

The CPS method [58] uses a plastic collapse criterion, where failure is initiated when the stresses in the material exceed a critical value (i.e. ultimate tensile strength). The upper (plain pipe) and lower (long groove) limit solutions provide bounds for the collapse pressure prediction, and the actual failure is determined based on the metal loss. The main advantage of this method is its ability to make full use of the actual corrosion geometry and tensile properties of the material. In addition flaw interaction is taken into account [58].

2.4.2 Crack Flaw Assessment

Cracks in high pressure pipelines may result from the interaction of metallic material, tensile stress and an aggressive electrolyte.

The crack characteristics can vary greatly depending on the cause of the crack, the material, and the environment. Cracks can initiate on the external pipeline surface and grow in both the depth and surface directions. Growth along the surface is perpendicular to the hoop stress, resulting in crack alignment along the longitudinal axis of the pipeline [81].

There are several assessment methods for crack like flaws in pipelines including API 579 [1], BS7910 [2], NG18 [82], and software applications such as CorLAS [4]. All have been used successfully to evaluate crack flaws, but the degree of conservatism and sensitivity to the various input parameters is not known.

2.4.2.1 Failure Assessment Diagram (FAD)

The failure assessment diagram (FAD) is widely used for assessing crack-like flaws in pipelines. A series of rupture tests were undertaken by Cravero and Ruggieri [83] to investigate

the failure behavior of axial cracks in pipelines. Their study validated the use of Failure Assessment Diagram (FAD)-based methodologies for assessing axial crack flaws in pipelines. Moreover, the results showed larger margins between the experimental and the predicted failure pressures for deeper cracks, particularly for the BS7910 cylinder approach. Additionally, burst tests were conducted by Mahendra and George [84] to investigate the failure behavior of longitudinal cracks in high pressure gas cylinders. Their study showed that the predicted FAD failure pressure was much lower than the experimental collapse pressure, using API 579 and BS 7910. Their results also revealed that the most conservative predictions were those obtained using the BS 7910 Level 2 FAD. The FAD approach can be used for a wide range of material behaviors, from brittle fracture under LEFM conditions to ductile fully plastic collapse in three deferent levels as follows:

➤ **Level 1 FAD**

The most convenient level of FAD, where there is limited information on the material properties or loading conditions, is level 1 (Figure 2-37). The crack flaw is considered acceptable if K_r is less than 0.707 and S_r is less than 0.8. If the assessment point lies in the area within the assessment line, the crack is acceptable. Otherwise it is not. It should be noted that K_r and S_r are toughness ratios and parameters for plastic collapse. These are shown as follows:

$$K_r = \frac{K_I}{K_c} \quad (2.56)$$

$$S_r = \frac{\sigma_{ref}^p}{\sigma_{flow}} \quad (2.57)$$

Where

$$\sigma_{flow} = \frac{\sigma_0 + \sigma_u}{2} \leq 1.2\sigma_0 \quad (2.58)$$

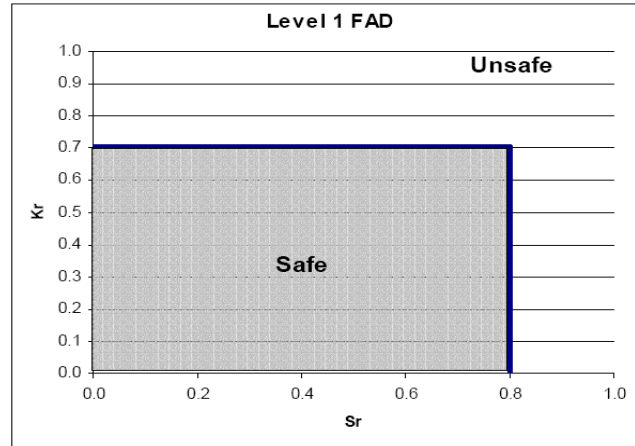


Figure 2-37- Failure Assessment Diagram (Level 1) [73]

➤ Level 2 FAD

The level 2 FAD provides a better estimate of the structural integrity of a component than a Level 1 assessment with a crack-like flaw [85] because Level 1 is based on the assumption of an elastic-perfectly plastic stress-strain curve with no strain hardening. Level 2 and Level 3 allow more by using the actual shape of the material stress-strain curve [2]. The assessment line is given by Equation (2.59) and if the assessment point lies within the area bounded by the axes and the assessment line, the flaw is acceptable otherwise it is not (Figure 2-38).

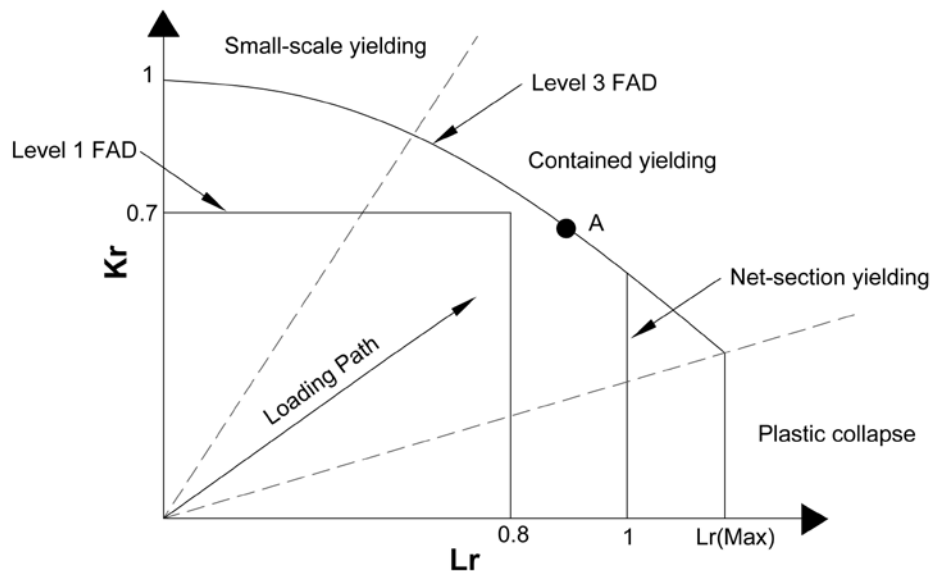


Figure 2-38- Failure Assessment Diagram (Level 3) [1]

$$K_r = (1 - 0.14(L_r^P)^2 \left(0.3 + 0.7 \exp \left[-0.65 (L_r^P)^6 \right] \right)) \quad (2.59)$$

The limiting cut-off line ($L_{r(\max)}^P$) is to prevent localized plastic collapse and is calculated as follows:

$$L_{r(\max)}^P = \frac{\sigma_y + \sigma_u}{2\sigma_{ys}} \quad (2.60)$$

➤ Level 3 FAD

The assessment procedure in Level 3 FAD provides the best estimate of the structural integrity of a component with a crack-like flaw [1]. It requires a true stress-strain curve for the material containing the flaw. The assessment line is given by Equation (2.59) and if the assessment point lies within the area bounded by the axes and the assessment line, the flaw is acceptable otherwise it is not acceptable. Five methods (A to E) are associated with a level 3 FAD based on API 579.

$$K_r = \left[\frac{E \varepsilon_{ref}}{L_r^P \sigma_Y} + \frac{(L_r^P)^3 \sigma_Y}{2E \varepsilon_{ref}} \right]^{-0.5} \quad (2.61)$$

The FAD is divided into three regions (Figure 2-38): small-scale yielding contained yielding and plastic collapse [53].

2.4.2.2 NG-18 Crack Assessment Method

The NG-18 approach can be used to evaluate a crack or crack like flaws in pipelines. The NG-18 equation incorporates the flow stress and fracture toughness or Charpy fracture energy (CVN) to evaluate the failure pressure in pipeline as follows [86]:

$$K_I^2 = \left(\frac{E \text{ CVN}}{A} \right)^2 = \frac{8}{\pi} c_{eq} \times \bar{\sigma}^2 \times \ln \sec \left(\frac{\pi \times M_p \sigma_\theta}{2\bar{\sigma}} \right) \quad (2.62)$$

Where

$$\sigma_f = \sigma_0 + 68.9 \text{ (MPa)}$$

$$M_p = \frac{1 - \frac{d}{t} \left(\frac{1}{M_t} \right)}{1 - \frac{d}{t}}$$

and

$$M_t = \sqrt{\left[1 + 1.255 \left(\frac{c_{eq}^2}{Rt} \right) - 0.0135 \left(\frac{c_{eq}^4}{R^2 t^2} \right) \right]}$$

2.4.2.3 CorLAS

CorLAS is a life prediction software developed by CC Technologies [4]. It evaluates the residual strength of pipelines containing corrosion or stress-corrosion cracking (SCC), stating “that the critical flaw size for the fracture-toughness failure criterion may be determined in one of two ways using the J integral. The first method involves computing the condition for which the applied value of J integral (J_{ap}) is equal to the J fracture toughness (J_C) of the material. When J_C is applied, the condition for initiation of tearing (crack advance) is predicted. However, if J_C is taken to be the maximum toughness, the condition for failure or tearing instability can then be predicted. This second method involves computing the tearing instability condition where the applied tearing parameter (dJ_{ap}/da) is equal to the tearing resistance (dJ/da) of the material, and is illustrated in Figure 2-39. Both methods require iterative calculations to determine the critical flaw size” [4].

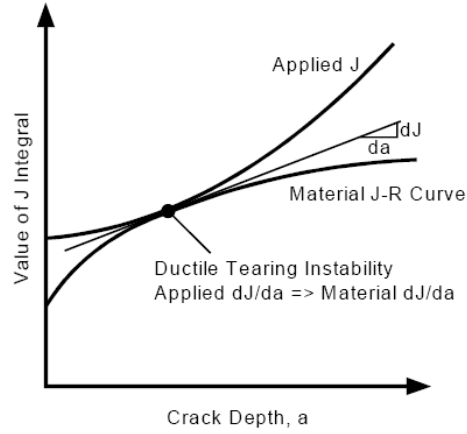


Figure 2-39- Illustration of Tearing Instability Criterion [4]

For the surface crack, the following equation is used to compute values of applied J as a function of crack size (a) and stress (σ):

$$J = Q_f F_{sf} \left[\frac{\sigma^2 \pi a}{E} + f_3(n) a \epsilon_p \sigma \right] \quad (2.63)$$

Q_f is the elliptical shape factor, F_{sf} is the free surface factor and σ is the applied stress, and $f_3(n)$ is the function developed by Shin and Hutchinson [87]. The J value is either measured from a standard test or Charpy energy using empirical Equation (2.63), given above.

2.5 Experimental Burst Tests [5]

To investigate the failure behavior of pipes containing longitudinal either corrosion, cracks or CIC flaws using 508 mm diameter, 5.7mm wall thickness line pipe. Rupture tests were carried out on end-capped, seam-welded pipe specimens. The flaws were created in the pipe sections, away from the seam welds, and the geometries were accurately measured before conducting the rupture tests. The pipe was closed by welding on hemispherical end caps and then filled with water. The pipe was initially internally pressurized to 1 MPa to verify that there were no leaks. Subsequently the pressure was increased at a rate of $9.83 \times 10^{-5} \text{ m}^3/\text{min}$ until failure

occurred. The pressure in the pipe was continuously measured using a pressure transducer and amplifier. The highest pressure was recorded for each test.

2.5.1 Corrosion Flaws

Three rupture tests were completed on sections of pipe (1800mm long \times 508mm OD \times 5.7 mm thickness) that contained simulated corrosion flaws. These flaws, 200 mm long, 30 mm wide (Figure 2-40 & Figure 2-41), were machined on the outside of the pipe with depths varying from 22% to 61% of the wall thickness. The corners of the groove were rounded with to a radius of 6mm to decrease the stress concentration.

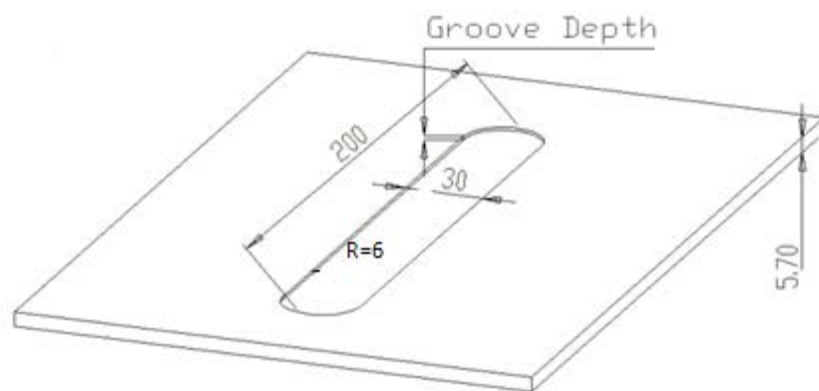


Figure 2-40- A Sample Corrosion Flaw Profile



Figure 2-41- An Artificial Corrosion in a Tested Pipe

The predicted failure pressures of the pipes tested were calculated based on Modified B31G and RSTRENG. The average difference for RSTRENG and Modified B31G were 23.8% and 17.20% respectively. The study also showed that the longitudinal length of a corroded area is the most important parameter for determining the failure pressure. The circumferential size has a

smaller influence on the collapse pressure. The results are shown in

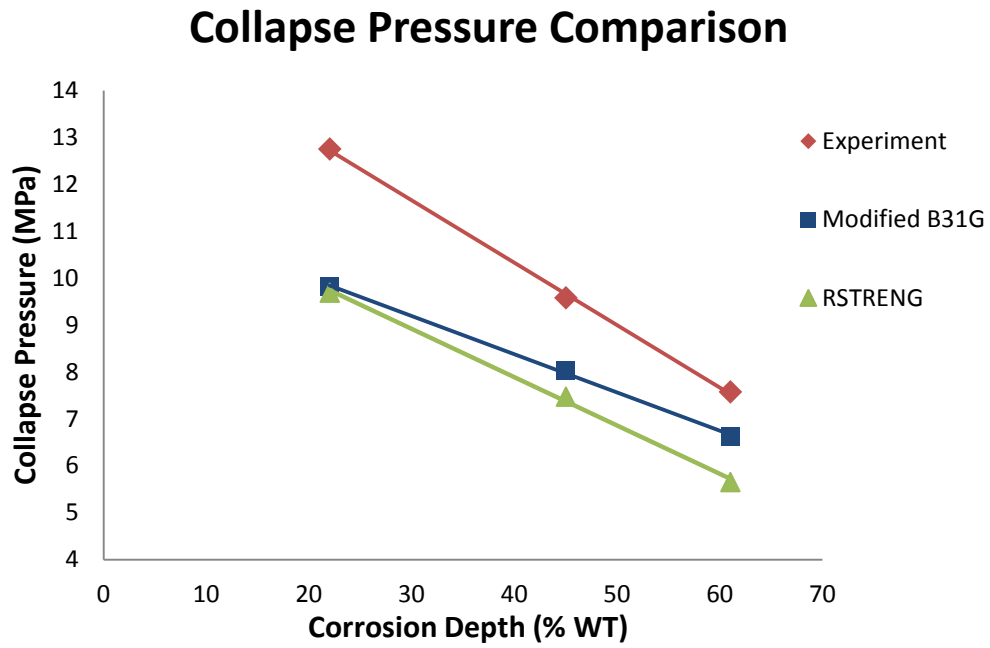


Figure 2-42.

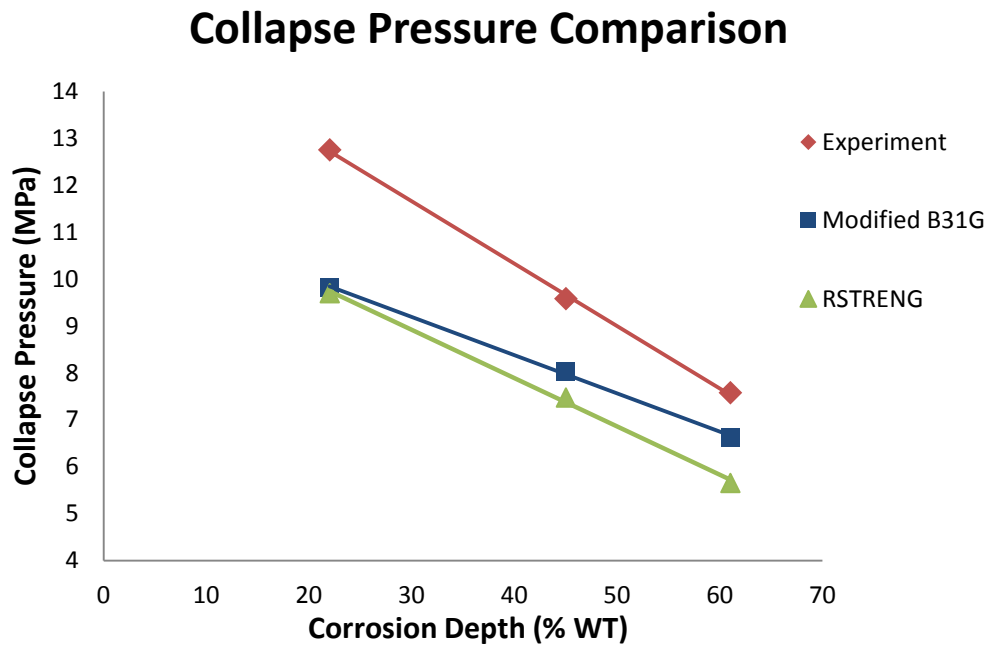


Figure 2-42- Failure Pressures Comparison between the Analytical Methods and the Experimental [5]

2.5.2 Crack Flaws

Four rupture tests were undertaken in samples containing cracks of different depths ranging from 38% to 51% of the wall thickness, and constant length of 200 mm. To create a sharp crack a narrow slit was initially cut in the pipe using a Jeweller's saw, and then the pipe was subjected to cyclic loading until a fatigue crack initiated and propagated at the bottom of the slit (Figure 2-43). The depth of the initial slit was varied, based on the required final flaw depth (Figure 2-44). The maximum applied hoop stress was 340 MPa, well below the yield strength of this steel. In general, the number of cycles required to create a fatigue crack of the required depth varied from 75000 to 125000 cycles.

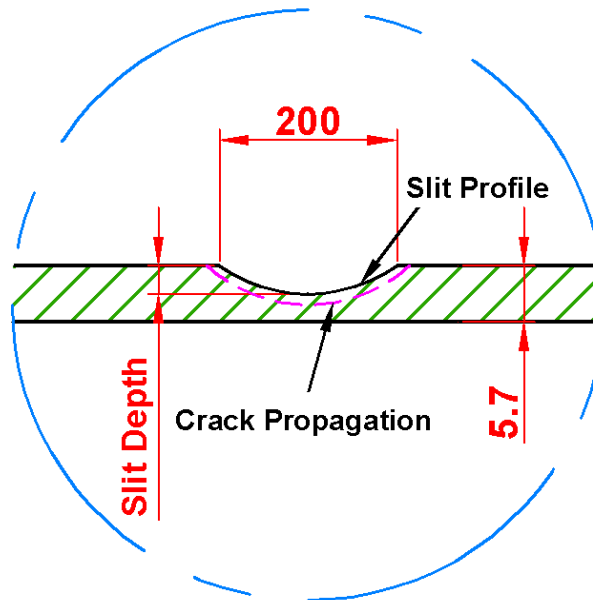


Figure 2-43- Machined slit, and crack after cyclic loading

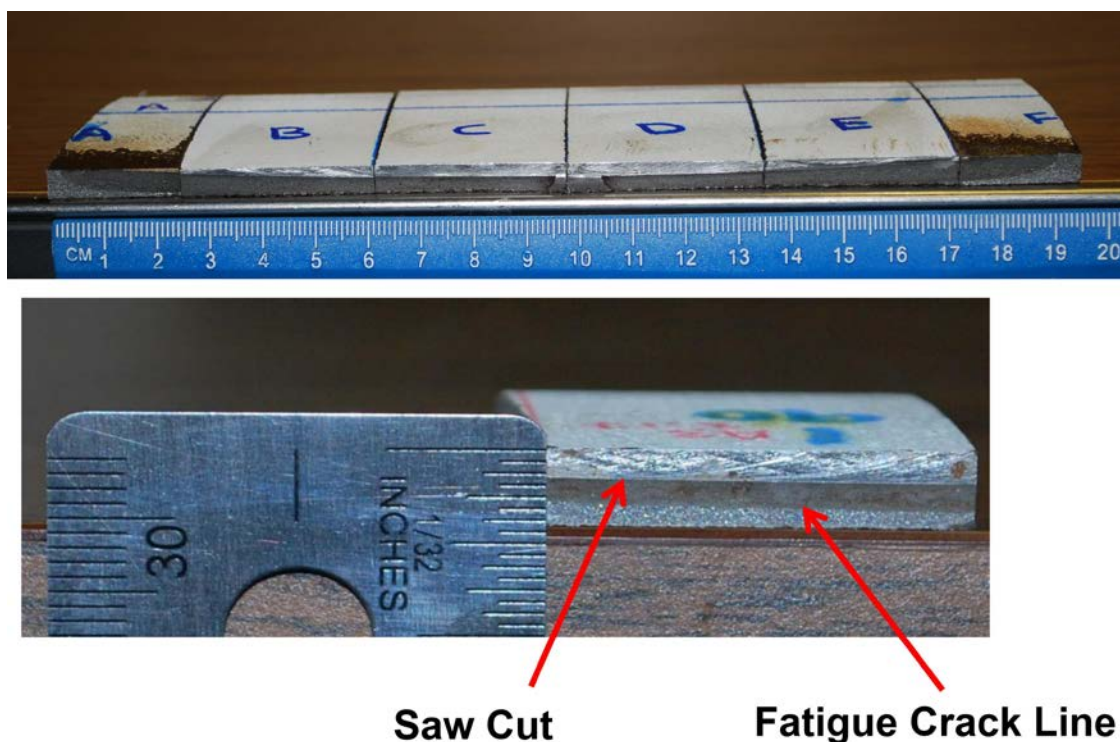


Figure 2-44- Crack Profile in a Tested Pipe after Pre-Fatiguing Procedure

The integrity analyses compared the bursts predictions based on API 579 & BS7910 Level 3 FAD. These results were compared with the CorLAS and NG-18 methods. The results are shown in Table 2-3.

Table 2-3- Comparison of Measured and Predicted Failure Pressures for the Pipes Tested in Different Methods

Test ID	Crack Depth (a) (%WT)	Experimental Failure Pressure (MPa)	Predicted Failure Pressure (MPa)				Difference (%)			
			API 579 Cylinder	BS7910 Cylinder	CorLAS	NG-18	API 579 Cylinder	BS7910 Cylinder	CorLAS	NG-18
CR1	38	10.1	8.10	5.80	8.48	7.10	20.0	43.0	16.0	30.0
CR2	47	9.30	7.10	4.62	7.69	6.30	24.0	50.0	17.0	32.0
CR3	48	9.60	6.86	4.45	7.58	6.20	29.0	54.0	21.0	35.0
CR4	51	8.83	6.21	3.97	7.24	5.90	30.0	55.0	18.0	33.0
Average Difference (%)							25.0	50.0	18.0	33.0

All methods predicted a failure pressure less than the experimental failure pressure. The CorLAS results predicted the better agreement with the experimental results. The most

conservative predictions were made using BS7910 Level 3 FAD. This study verified that the conventional methods such as BS7910 and API579 Level 3 FAD Method B provide very conservative results. Therefore, there is a need to move on to the newer methods such as Level 3 FAD Method D.

2.5.3 Crack in Corrosion (CIC) Flaws

Five rupture tests were carried out to investigate the failure behavior of axial CIC flaws with varying flaw depths ranging from 52% to 66% of the wall thickness (Table 2-4). To create a crack in corrosion (CIC) flaw a narrow slit was first machined in the pipe. The pipe was cycled until a fatigue crack formed and propagated from the bottom of the slit. An artificial corrosion (groove) was then machined in the form of a rectangle over the initial narrow slit on the outside of the pipe, as shown in Figure 2-45. The depth of the corrosion flow was the same as the depth of the initial slit.

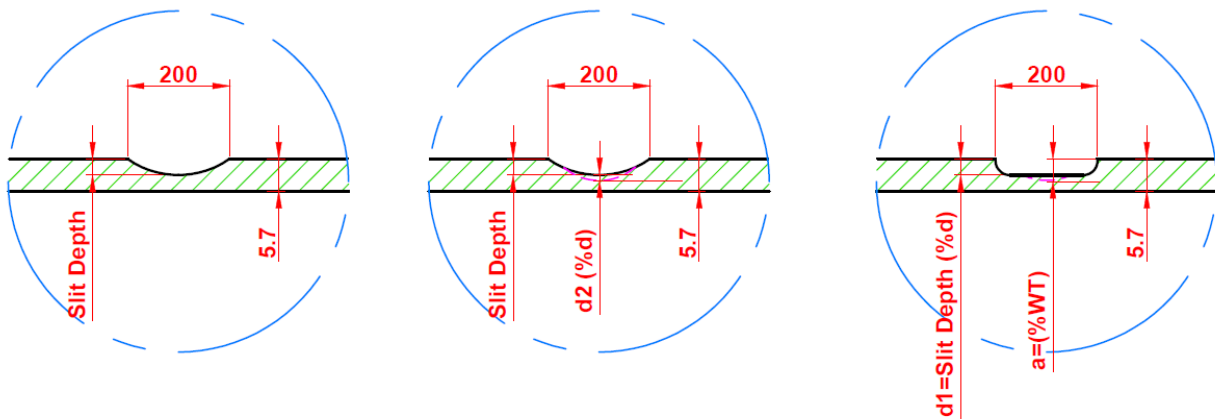


Figure 2-45- CIC Flaw Manufacture a) Cut slit, b) Fatigue crack and c) Corrosion flow [73]

Table 2-4- CIC flaw geometry

Test No.	Flaw Depth				Total Flaw Depth (a) (%WT)	Wall Thickness (mm)
	Corrosion		Crack			
	d ₁ (%WT)	(mm)	d ₂ (%WT)	(mm)		
CIC1	35	2.01	17	0.95	52	5.7
CIC2	37	2.08	22	1.28	59	5.7
CIC3	40	2.26	20	1.16	60	5.7
CIC4	43	2.43	18	1.04	61	5.7
CIC5	43	2.44	23	1.32	66	5.7

To predict the failure pressure of a CIC flaw, two different assessment methods were employed (Figure 2-46):

1-The CIC flaws were assumed to be crack flaws of equivalent depths and lengths and Level 3 FAD Method B was applied to predict the collapse pressure.

2-The CIC flaws were assumed to be corrosion flaws of equivalent depths and lengths and RSTRENG was applied to predict the collapse pressure.

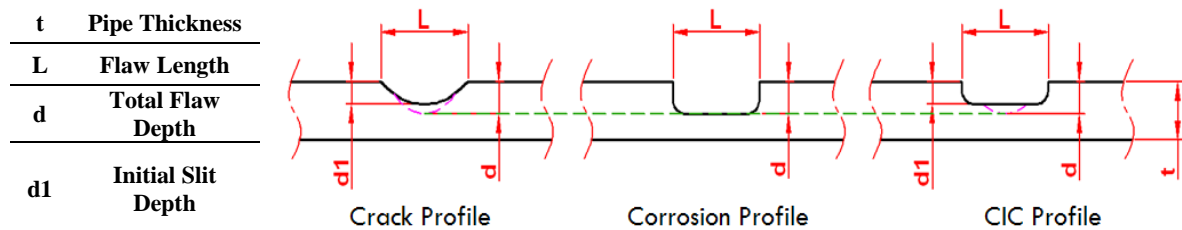


Figure 2-46- Comparison between Crack, Corrosion and CIC Flaws of Equivalent Depths

The results also are shown in Table 2-5.

Table 2-5- Comparison between the Experimental and the Predicted Collapse Pressures for CIC Flaws

Test ID	Total Flaw Depth (% WT)	Exp. Failure Pressure (MPa)	Predicted the Failure Pressure of Equivalent Flaw (MPa)		Difference (%)	
			Crack Only	Corrosion Only	Crack Only	Corrosion Only
			Level 3 FAD API 579-Cylinder	RSTRENG	Level 3 FAD API 579-Cylinder	RSTRENG
CIC1	52	7.74	6.15	6.55	21.0	15.0
CIC2	59	6.72	4.89	5.75	27.0	14.0
CIC3	60	7.06	4.75	5.63	33.0	20.0
CIC4	61	7.89	4.45	5.51	44.0	30.0
CIC5	66	6.15	3.73	4.91	39.0	20.0
				Average Difference (%)	33.0	20

A review of the results showed that the failure behavior of the CIC flaws fell between corrosion flaws (lower bound) and crack flaws (upper bound) of equivalent depth. The transition to crack flaw behavior only occurs when the crack flaw depth is significant or vice versa. Moreover, failures for all CIC flaws occurred by plastic collapse, verified by examining the fracture surfaces. Moreover, the results verified that there is need to improve the evaluation of CIC flaws to get more accurate collapse prediction.

Chapter 3

Experimental Testing

3.1 Material Characterization

API 5L Grade X 52 pipeline steel of external diameter 20n inch (508 mm), and 5.7 mm wall thickness was investigated in the previous work [5]. Two additional Tensile, Charpy and fracture toughness tests (J-test) were undertaken in this study to verify the previous work and improves of the material properties data for the tested pipes. Two additional burst tests were undertaken on 36 inches (914.4 mm) pipe sections; therefore, tensile and Charpy tests were undertaken on these pipes to measure their material properties.

3.1.1 Tensile Test

3.1.1.1 20 inch Diameter Pipes

Sixteen circumferential tensile specimens were tested following ASTM E8M-09 [57]. The thickness of the specimens was 5.7 mm, the same as the wall thickness of the pipe. For analysis purposes, the modulus of elasticity (E) was assumed to be 207GPa. The average values of the 0.2% offset yield strength [88] and ultimate tensile strength in the circumferential direction for combinational of the previous and current data were 435.0 MPa (19.2 MPa standard deviation) and 572 MPa (standard deviation 14.1 MPa), respectively (Figure 3-1). For corrosion analysis, a critical stress corresponding to the ultimate tensile strength expressed as a true strength is often used. This value was 631.0 MPa (standard deviation 28.2 MPa) for the materials tested. The Ramberg-Osgood equation (Equation 3.1) given below expressed the true stress-true strain data and will be used for finite element modeling.

$$\varepsilon = \frac{\sigma}{E} + 1.75 \left(\frac{\sigma}{\sigma_y} \right)^{8.35} \left(\frac{\sigma}{E} \right) \quad (3.1)$$

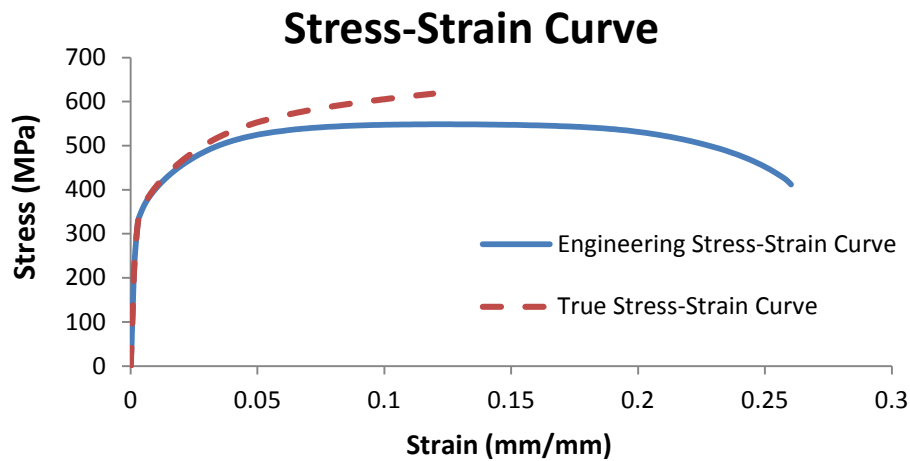


Figure 3-1- The Engineering and True Stress-Strain Curves in Circumferential Direction for One of Specimens

3.1.1.2 36 inch Diameter Pipes

Eleven circumferential and longitudinal tensile specimens were tested following ASTM E8M-09 [56]. The thickness of the pipe 1 and pipe 2 sections were 8.1 mm and 8.21 respectively, the same as the wall thickness of the pipes. For analysis purposes, the modulus of elasticity (E) was assumed to be 207GPa. The average values of the 0.2% offset yield strength [88] and ultimate tensile strength in the circumferential direction for both pipes data were 534.6 MPa (10.5 MPa standard deviation), and 631.0 MPa (standard deviation 8.9 MPa). The results are shown in Figure 3-2.

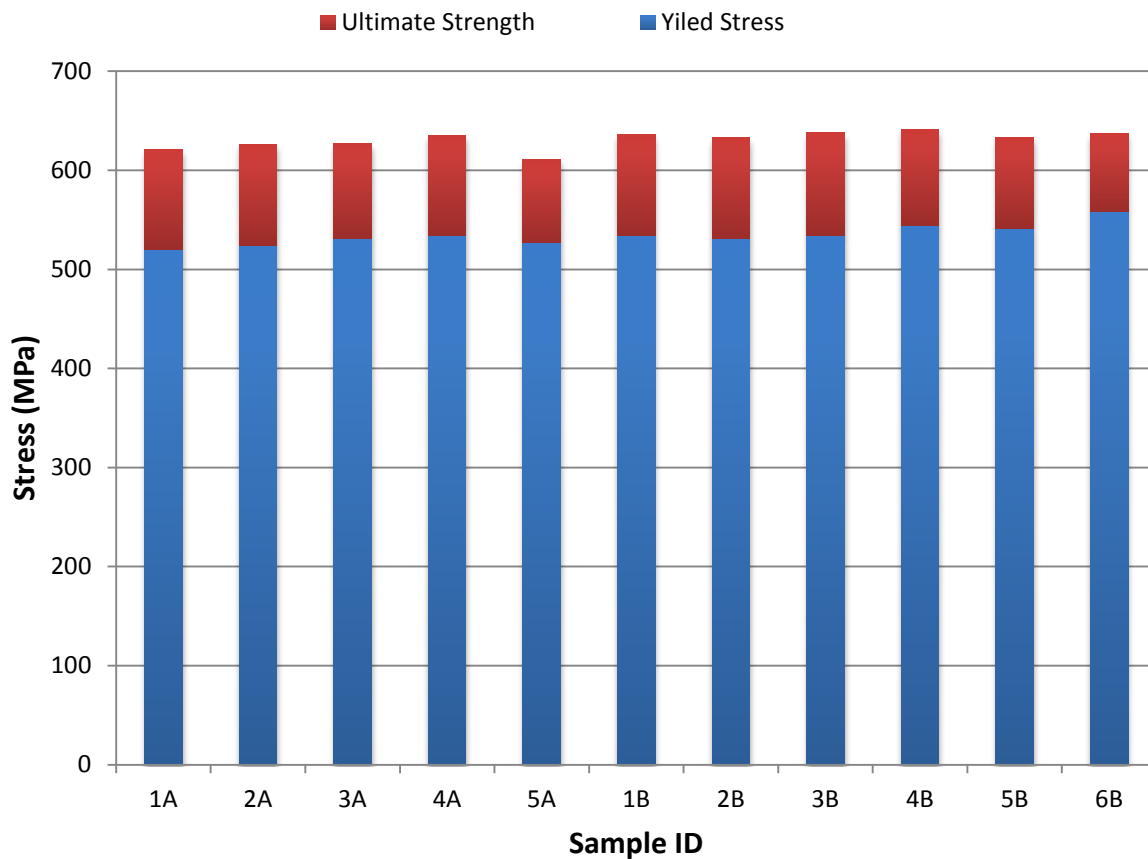


Figure 3-2- Tensile Tests Results for 36" Diameter Pipe 1 (A) & Pipe 2 (B)

3.1.2 Charpy Tests

3.1.2.1 20 inch Diameter Pipes

A set of six circumferential sub size Charpy V-notch impact specimens were removed from the pipe sections and tested at Anderson Associates Consulting Engineering Metallurgical Engineers and Testing Laboratory [89] in the three different temperatures (-16,0,22 ° C). The scaled full size results are shown in Table 3-1 and Figure 3-3 respectively.

Table 3-1-Charpy V-Notch Impact Test Results (20" Diameter Pipe) (Full Size)

Specimens	Impact Energy (J)			Fracture Appearance (% Shear)		
	-16° C	0° C	25° C	-16° C	0° C	25° C
1	45.1	58.7	63.2	60	60	100
2	31.6	58.7	63.2	50	50	100
3	40.6	58.7	63.2	60	60	100
4	36.0	40.6	58.7	60	60	100
5	45.1	58.7	63.2	70	70	100
6	54.2	58.7	58.7	80	80	100
Average	42.0	55.7	61.7	N/A	N/A	N/A

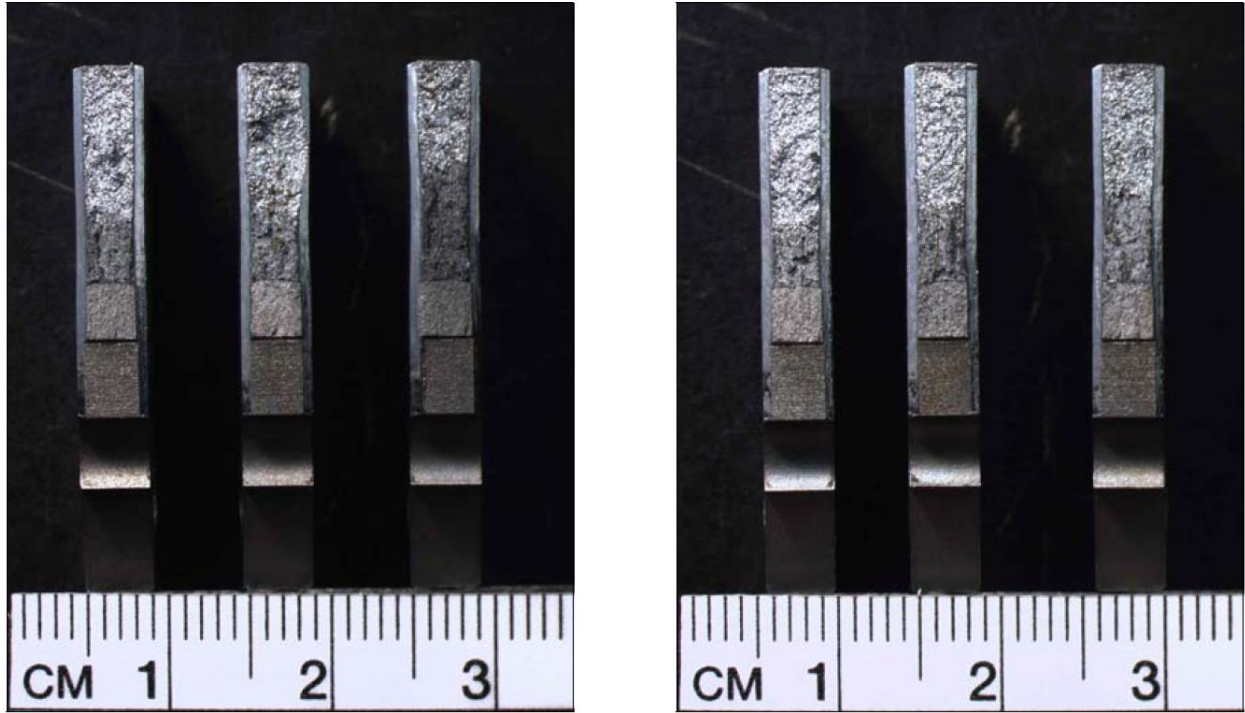


Figure 3-3- The Sample Fracture Surfaces of Charpy Specimens (20" Diameter Pipe)

3.1.2.2 36 inch Diameter Pipe

A set of 96 sub-size Charpy impact specimens (ASTM-E23-07 [59]) were machined from two different pipe sections and tested at eight different temperatures (-70,-42,-22, 3, 24, 50, 100 and 150 °C) (Figure 3-4). Equation (2.41) was applied to scale up the impact energy to full-size specimens.

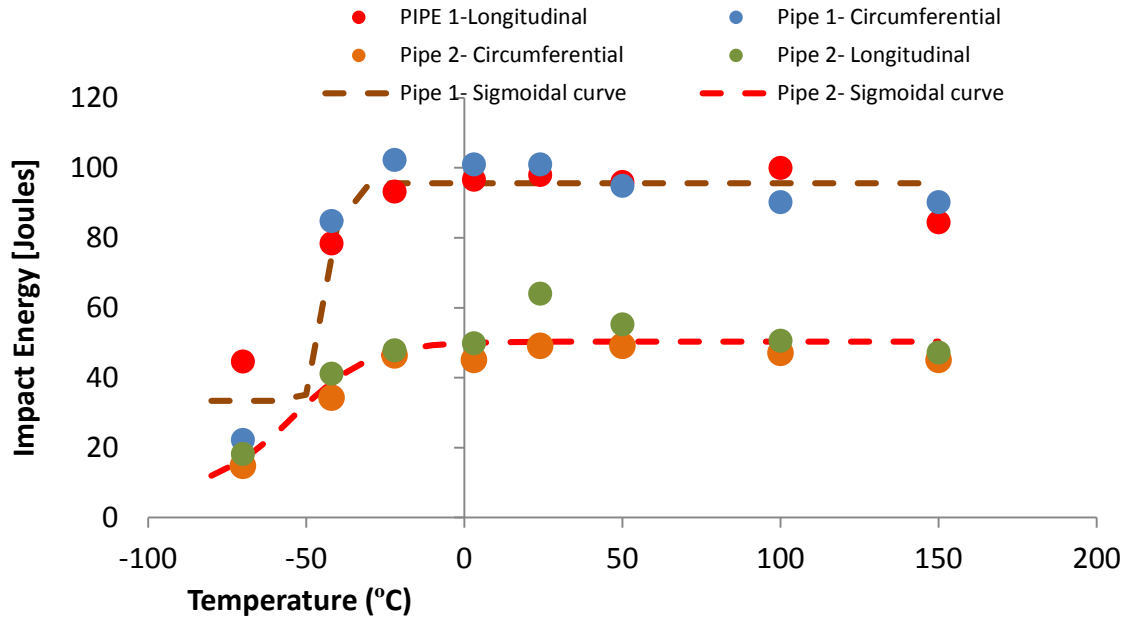


Figure 3-4 Charpy V-Notch Impact Test Results (Full Size-36 Inches Pipes)

A Boltzmann function was used to fit a sigmoidal curve for the CVN test results to determine the average upper shelf, lower shelf energy and transition temperature for both pipes (Table 3-2).

Table 3-2- Upper & Lower Shelf Energy (Full Size-36 Inches Pipes)

	Lower Shelf Average Energy E (J)	Upper Shelf Average Energy E (J)	Transition Temperature (°C)
Pipe 1	33.4	95.6	-43.0
Pipe 2	7.6	50.3	-53.0

In the absence of fracture toughness data, CVN data can be correlated to fracture toughness. The Rolfe-Novak Equation (2.42) was applied to correlate the upper shelf CVN impact energy to the lower bound value of the fracture toughness K_{IC} . The estimated fracture toughness for pipe 1 and pipe 2 are $195.6 \text{ MPa}\sqrt{\text{m}}$ and $102.9 \text{ MPa}\sqrt{\text{m}}$ respectively.

3.2 Experimental Rupture Tests

3.2.3 20 Inch Diameter Pipes

3.2.3.1 Corrosion Flaws

To expand the test matrix, three additional rupture tests were conducted on sections of pipe (1800mm long × 508mm OD × 5.7 mm thickness) that contained simulated corrosion flaws. The flaw dimensions were 200 mm long, 30 mm wide to keep consistency with the previous work [5]. All flaws were machined on the outside of the pipe with depths of 61%, 66%, and 70% of the wall thickness. The corners of the groove were rounded with to a radius of 6mm to decrease the stress concentration. It is worth noting that to improve the consistency of the results for the 61% WT section an additional experimental test was conducted.

3.2.3.2 Crack Flaws

One additional rupture test was undertaken in a 20 inch pipe containing 66% WT crack depth, and t length of 200 mm to expand experimental of the previous study [5]. The crack was created in the same manner the previous procedure [5]

3.2.4 36 Inch Diameter Pipes

3.2.4.1 Cracks, Corrosion, and CIC Flaws

Two more additional burst tests were undertaken on 36 inches pipes that contained colonies of cracks, corrosion and CIC flaws with various depths. The same procedure [5] was applied to do the burst tests. The pipe dimensions and geometry of the flaws are summarised in Table 3-3 and Figure 3-5 respectively.

Table 3-3- Pipe Dimension (Geometry & Flaws-36" Diameter)

		Pipe 1	Pipe 2
Measured Diameter		911 mm	914 mm
Measure Thickness		8.10 mm	8.21 mm
Length of Section		2530 mm	2570 mm
Corrosion Depth (mm)	Maximum	2.51 mm (31 %WT)	2.92 mm (35.6 %WT)
	Average	1.68 mm (20.7 %WT)	1.8 mm (21.9 %WT)
	Minimum	1.4 mm (17.2 %WT)	1.32 mm (16.1 %WT)
Corrosion Length (mm)	Maximum	12.7 mm	114.3 mm
	Average	9.41 mm	14.9 mm
	Minimum	6.35 mm	1.59 mm
Crack Colony Length (mm)	Maximum	584.2 mm	889 mm
	Minimum	12.7 mm	9.53 mm
Crack Linear (mm)	Maximum	63.5 mm	203.2 mm
	Minimum	8.26 mm	6.35 mm

Pipe 1

Pipe 2



Figure 3-5- 36" Pipe Sections before Rupture Tests

3.2.4.2 Results and Discussion

Pipe 1 collapsed due to an existing shallow crack on the weld; therefore, the collapse pressure was predicted for the pipe 1 using the API Level 2 Method B approach. The same procedure of the previous study [5] applied to predict the collapse pressure based on API Level 2 Method B.

The results are shown in Table 3-4 and Figure 3-6.

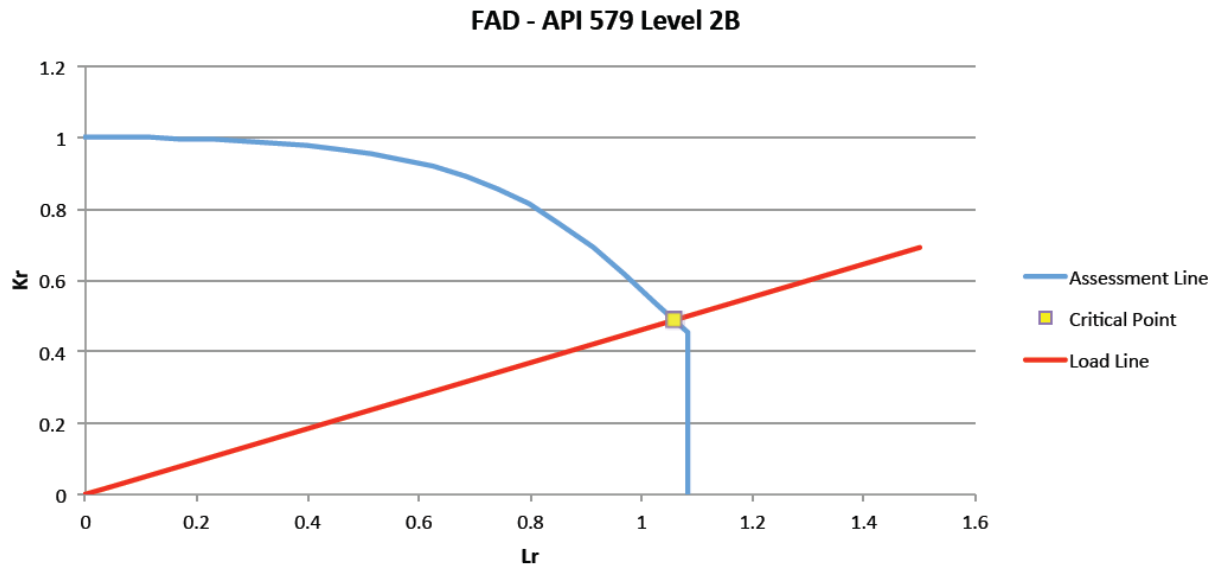


Figure 3-6 Collapse Pressure Prediction for Crack using API579 Level 2 FAD Method B (Pipe1-36")

Table 3-4- Comparison between the Experimental and the Predicted Collapse Pressures (Pipe 1-36")

	Experimental Collapse Pressure (MPa)	API Level 2 Method B (MPa)	Difference (%)
Pipe 1	11.06	10.4	9.2

A review of the result in Figure 3-6 showed that the failure occurred by plastic collapse, verified by examining the fracture surfaces.

Pipe 2 failed at an existing corrosion flaw. Therefore, the collapse pressure was predicted for the pipe 2 using the CPS, RSTRENG and B31G. The results for this pipe section are shown as follows:

Table 3-5- Comparison between the Experimental and the Predicted Collapse Pressures (Pipe 2-36")

	Experimental Collapse Pressure (MPa)	Predicted Pressure (MPa)			Difference (%)		
		CPS	RSTRENG	B31G	CPS	RSTRENG	B31G
Pipe 2	11.11	10.4	9.34	9.43	6.4	15.9	15.1

The failure of the corroded pipe occurred due to plastic collapse by ductile tearing which was verified by examining the fracture surfaces. The failure criterion, used in CPS, RSTRENG, and B31G methods, predicts the onset of ductile tearing at a critical point within the corrosion flaw [4] Plastic collapse of a corrosion flaw takes place by local necking of the ligament owing to an increase in the hoop stress, which overcomes strain hardening of the material by increasing the pipe radius and decreasing wall thickness. A rupture of pipe tested containing a corrosion flaw is shown in Figure 3-7.

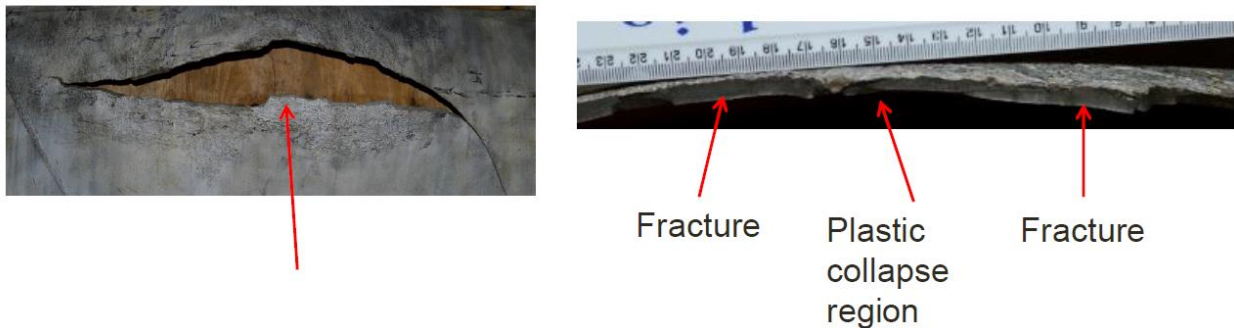


Figure 3-7- The Tested Pipe 2 Containing Corrosion Flaw after the Rupture Test

Pipe 1



Pipe 2

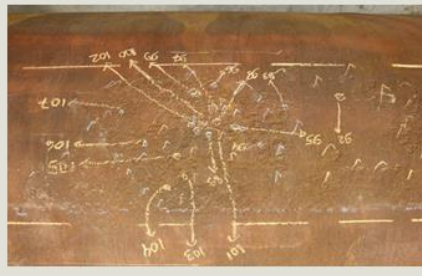


Figure 3-8- Sample Flaws for 36 inches Pipes

Chapter 4

Results and Discussion

The results of experimental, analytical methods and finite element modeling for corrosion, crack and CIC flaws are reviewed and discussed in this chapter.

4.1 Corrosion Flaws

4.1.1 Corrosion-Finite Element Model Development

The finite element method (FEM) has been used widely in the automotive, aerospace, and a pipeline industry. FEM can be applied to predict the failure pressure of different types of flaws based on fracture mechanics and plastic collapse. This has been used by several authors [11, 90-92] to evaluate the collapse of corrosion flaws [58].

In this study, the implicit finite element program Abaqus/CAE 6.10 was used to predict the collapse pressures of thin-walled pipes containing different types of flaws. A three-dimensional

quarter symmetry model was used to simulate longitudinal corrosion of uniform depth in a thin-walled pipe. Twenty-node quadratic brick elements (C3D20R) with reduced integration were used. This type of element is recommended [93] for 3D modeling, and for large strain problems because it gives more accurate results with reduced computation time.

The mechanical properties of the material were represented using Ramberg-Osgood deformation plasticity [75] which is applicable for monotonically increasing loads, providing a numerically efficient solution. The model is most commonly applied in static loading with small-displacement analysis for which the fully plastic solution must be developed as a part of the model [93]. Therefore, non-linear geometry analysis was applied to consider the large deformation effect on the model to obtain better results. The boundary condition is shown in Figure 4-1.

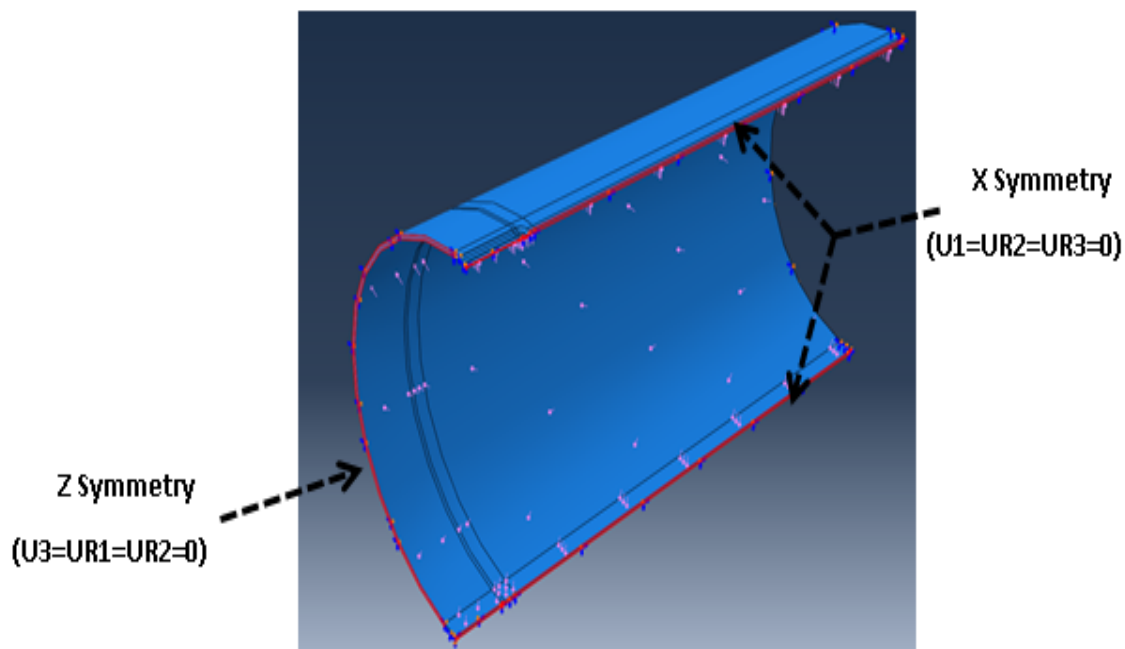


Figure 4-1- Boundary Condition of the Corrosion Model (45%)

Six elements were used throughout of the pipe wall thickness. The three-dimensional meshes consisted of 108113 nodes and 23295 elements. The model was designed to be parametric, and can be used for various corrosion depths and lengths.

Five models with corrosion flaws of 200mm length and depths of 22%, 45%, 61%, 66% and 70% WT were simulated, corresponding to the experimental flaw geometry consisting of a rectangular groove with a radius at the corners. Modeling of the end caps was neglected because the case was under plain strain and generally the end caps should be modeled when there is significant plasticity, which is not the case in the thin-walled pipes. Modeling of the end caps would only increase the number of elements and run time [74]. The width of the corrosion in all models was 30 mm. Figure 4-2 shows 45% WT of the corrosion flaw.

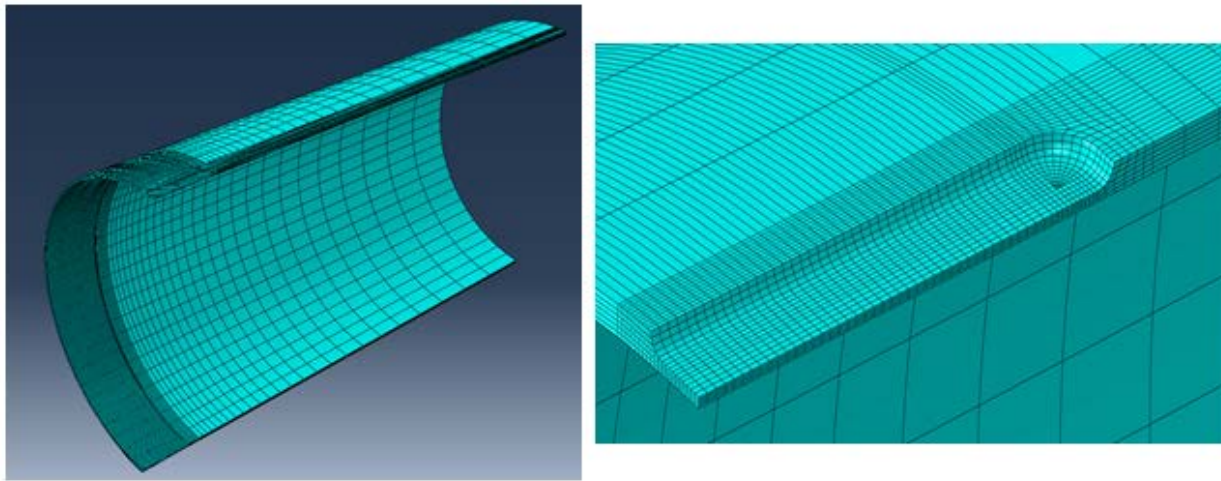


Figure 4-2- A Sample Corrosion Model (45% WT)

4.1.2 Collapse Pressure Prediction for a Corrosion Flaw

Several methods have been proposed for the prediction of collapse pressure of corrosion flaws in pipelines. Mok et al.[94] modeled a simple longitudinal groove in a pipe, and plotted the load-displacement of the model to identify initiation of asymptotic behaviour. The model used the

actual material properties. The predicted collapse pressure was within 5% of the experimental results. The accuracy of this method was dependent upon the load-displacement curve.

Several corrosion pits and other geometries were modeled by Chouchaoui [91]. He determined the highest unstable load obtained by FEM results, and assumed that the load was the plastic collapse load. The predicted collapse pressures by FEM were within -6% to 7% of the experimental results. The advantage of this method is that the collapse pressure can be determined in a reasonable computing time.

Sattarifar [95] also conducted a number of 3D corrosion simulations. He determined the plastic collapse pressure by extrapolating the displacement from the load-displacement curve after the numerical instability load.

Numerical instability occurs when the displacement increases while the load decreases. Most analytical methods cannot simulate load relaxation, and hence the simulation stops when the load ceases to increase with increasing displacement [96]. Therefore, Crisfield et al. [97] proposed the “modified Riks method” to solve this problem. In theory, this method allows the calculation of accurate displacements and forces beyond the point of instability. By using this method, the global collapse load can be identified as the maximum load, which occurs prior to a drop in load [96].

Choi et al. [98] carried out finite element modeling to develop limit load solutions for corroded gas pipelines. Incremental plasticity, combined with large deformation theory was applied for the entire FEM to simulate the local deformation in the flaw area. The collapse load was determined when the von Mises stress distribution across the corroded ligament reached the reference stress. It is important to note that the reference stresses were set to different values. The

reference stresses were the yield strength, σ_0 , flow strength, σ_f and , 80 or 90% ultimate strength, σ_u respectively. The flow strength was defined as:

$$\sigma_f = \frac{\sigma_0 + \sigma_u}{2} \quad (4.1)$$

The collapse predictions obtained from the yield strength or flow stress were conservative in comparison with ultimate strength. In general, the most accurate prediction was achieved when the reference stress assumed was 90% ultimate strength, and the difference was less than 7%.

Cronin tested twenty five burst tests on pipe sections removed from service due to presence of corrosion flaws [99]. He applied the non-linear FEM analysis to predict the collapse pressure of the pipes. The collapse pressure was predicted using the von-Mises criterion. The initial failure was assumed to occur when the stress exceeded the ultimate true stress. It was shown that the Finite Element method is very sensitive to local changes in defect depth and requires accurate geometry measurements to provide an advantage over other assessment methods. This is related to the fact that, in the Finite Element Model, the local stresses are primarily determined by the local geometry, with the surrounding geometry as a secondary effect. Detailed material properties, as determined from uniaxial tensile tests, are also required for accurate burst pressure predictions [99].

Fu and Kirkwood [92] proposed a different solution. They found that the criterion based on the von-Mises stress gave the most accurate collapse load. Therefore, this method was used in this study. According to their method, failure was predicted using a critical stress approach [92] equal to the ultimate material strength, expressed as true stress. In general, a pipe may fail by either global or local plastic collapse. A flaw free pipe would fail by global plastic collapse and a corroded pipe would fail by local plastic collapse.

This concept was used to predict the collapse pressure in the corroded pipe. Figure 4-3 shows a typical corrosion flaw model subjected to an internal pressure of 9.47 MPa.

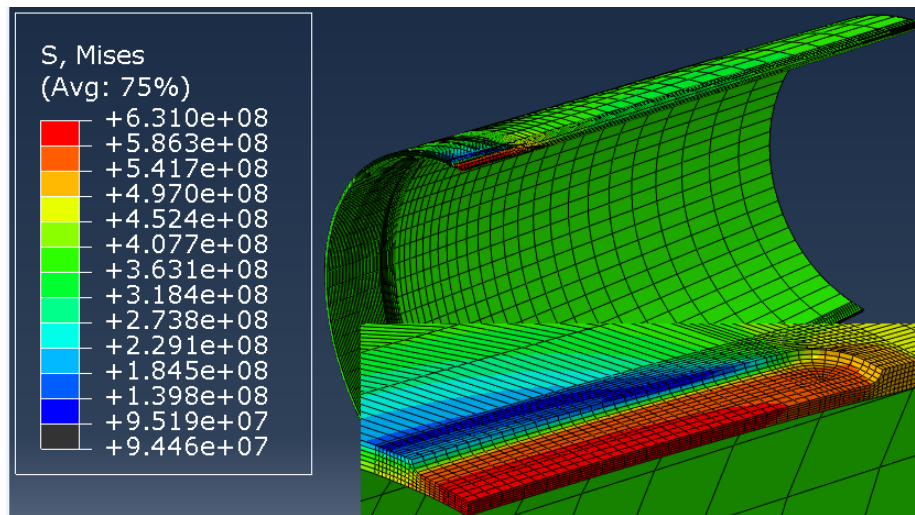


Figure 4-3-Corrosion Flaw Model (45% WT)

The initiation of failure was predicted when the maximum stress at the bottom of the corrosion (external element on the corroded area) reached the circumferential ultimate strength, expressed as the true stress of 631 MPa. The intersection between the predicted the von Mises stress, as a function of pressure, and the critical stress indicated the collapse pressure. The corrosion modeling analysis is shown in Figure 4-4.

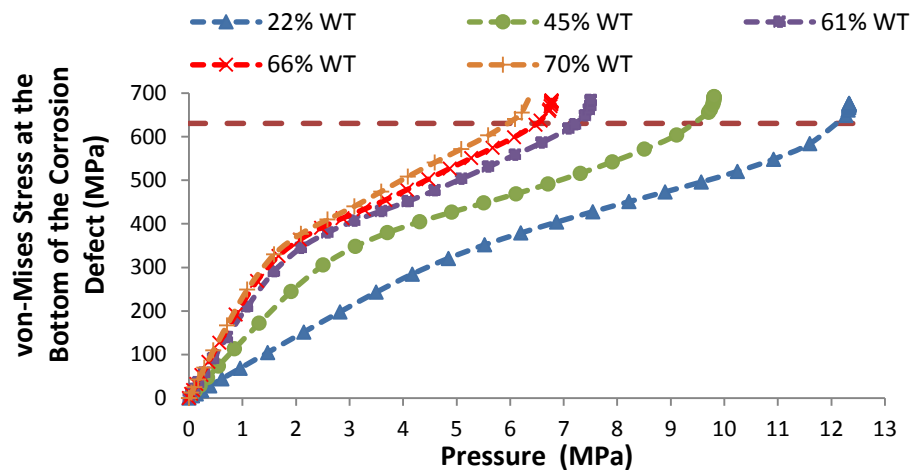


Figure 4-4- FE Analysis of Corrosion Flaws (varying depths)

4.1.3 Comparison between Experimental, Analytical, and FEM Results

The predicted collapse pressures were calculated using the CPS and RSTRENG methods, given in Table 4-1 and Figure 4-5 [73]. In general the CPS method provided more accurate results predicting collapse pressures between 80% and 93% of the experimental values (with an average difference of 13.5%). It should be noted that the results for the shallower flaws (22% and 45% WT) were more accurate than the deeper flaws (61% to 70% WT). This is because the failure for the shallower crack occurs due to the plastic collapse and that these methods are based on plastic collapse. The RSTRENG method was more conservative, predicting collapse pressures between 74% and 78% of the experimental values, with an average difference of 24.2%. The predicted collapse pressures using the CPS, RSTRENG and FEM models were compared to the experimentally measured values (Table 4-1) and are plotted in Figure 4-5. In general the predicted FEM model collapse pressures were conservative compared to the experimental results with an average difference of 3.20%.

Table 4-1- Comparison between Experimental and FEM Results for Corrosion Modeling

Test No.	Flaw Depth (%WT)	Exp. Collapse Pressure (MPa)	Predicted Collapse Pressure			Difference (%)		
			CPS (MPa)	RSTRENG (MPa)	FEM (MPa)	CPS	RSTRENG	FEM (MPa)
C1	22	12.76	11.96	9.74	12.1	6.3	23.7	5.3
C2	45	9.59	8.79	7.48	9.4	8.3	22.0	1.8
C3	61	7.58	6.35	5.66	7.2	16.2	25.3	4.5
C4	66	6.63	5.54	5.04	6.5	16.4	24.0	1.8
C5	70	6.12	4.90	4.52	6.0	20.0	26.1	2.6
Average						13.5	24.2	3.2

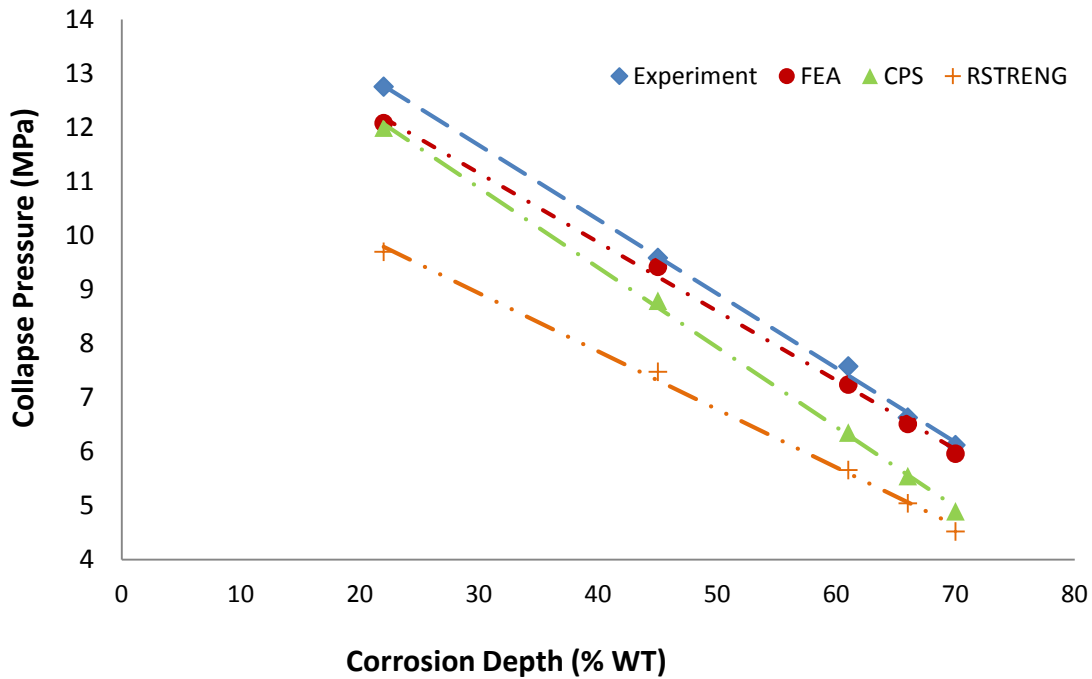


Figure 4-5- Predicted Corrosion Flaw Collapse Pressure Compared to Experimental Data

Both RSTRENG and CPS methods are based on the real corrosion profile which calculates the corrosion area based on iterative algorithms and are not suited to hand calculations.

In general, the CPS method gave more accurate results predicting collapse pressures between 80% and 93% of the experimental values (with an average difference of 13.5%). It should be noted that the results for the shallower flaws (22% and 45% WT) were more accurate than those for the deeper flaws (61% to 70% WT). The RSTRENG method was more conservative, predicting collapse pressures between 74% and 78% of the experimental values, with an average difference of 24.2%. Collapse pressures predicted using CPS, RSTRENG and FEM models were compared to the experimentally measured values (Table 4-1)) and are plotted in Figure 4-5 . In general, the predicted corrosion FEA model collapse pressures were conservative compared to the experimental results with an average difference of 3.2%.

Comparison of the above results shows that the most accurate method for assessing of a corrosion flaw is FEM. However, the other two analytical methods (CPS & RSTRENG) are also acceptable. In general, the corrosion geometry and material properties are the most important parameters, which affect the collapse pressure. Therefore, as these two parameters are measured and are more detailed, the collapse pressure prediction is more accurate.

FEM needs the detailed measurement of a corrosion flaw and material properties, and it is more time and cost consuming in comparison with the other methods. CPS requires more detailed tensile properties of the material in comparison with RSTRENG. Therefore, all methods can be used based on the level of information is available.

4.2 Crack Flaws

4.2.1 Crack Flaws-Finite Element Model Development

FEM analysis has been widely used to predict the failure pressure for crack flaws based on LEFM or EPFM. The fundamental challenge with modeling a crack for elastic analysis is the singularity of the strain and stress at the crack tip. This singularity cannot be characterized by regular polynomial shape functions used for isoparametric elements. In fact, a sharp crack in a linear elastic material produces a singularity at the crack tip with the function of $\frac{1}{\sqrt{r}}$. Henshell[100] and Barsoum [101] showed that by moving the mid-nodes of the quadratic elements, such as the 6-node triangular element shown in Figure 4-6 to the $\frac{1}{4}$ point the nearest sides connected to the crack tip can capture the singularity at the crack tip.

The differences between LEFM and EPFM modeling have been investigated [103], and it was concluded that LEFM significantly overestimated the failure pressure compared to the EPFM modeling. Cronin [103] showed the J-Integral and the stress intensity were in a very good

agreement in the elastic area. However, beyond the elastic region the J-Integral increased rapidly with increasing the load. Therefore, EPFM was more appropriate in crack flaw evaluation. To confirm this difference for the steel pipe under investigation, a 20 % crack flaw was modeled by both LEFM and EPFM. The results are shown in Figure 4-7.

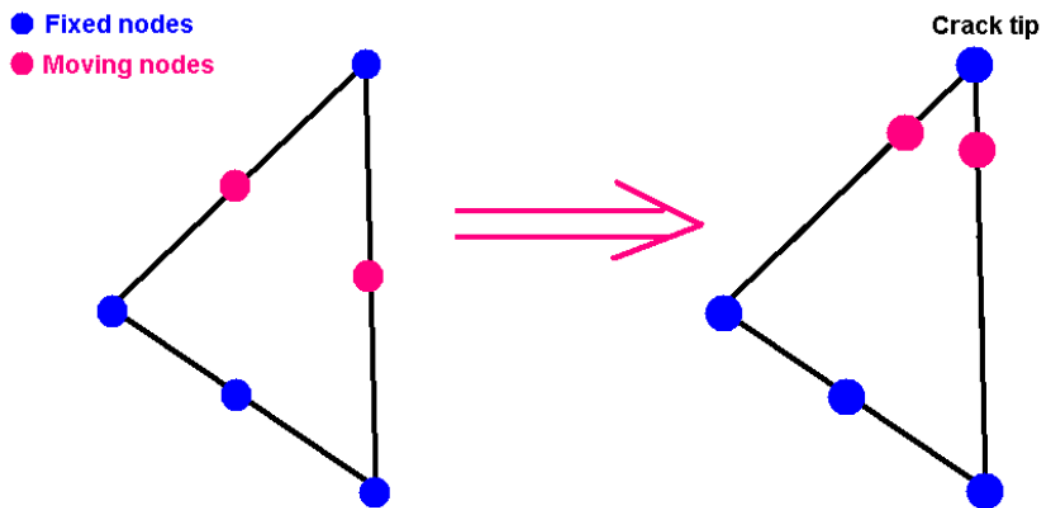


Figure 4-6--Singular 2D Element (Right) Produced from Regular 6-Node Triangular Element [102]

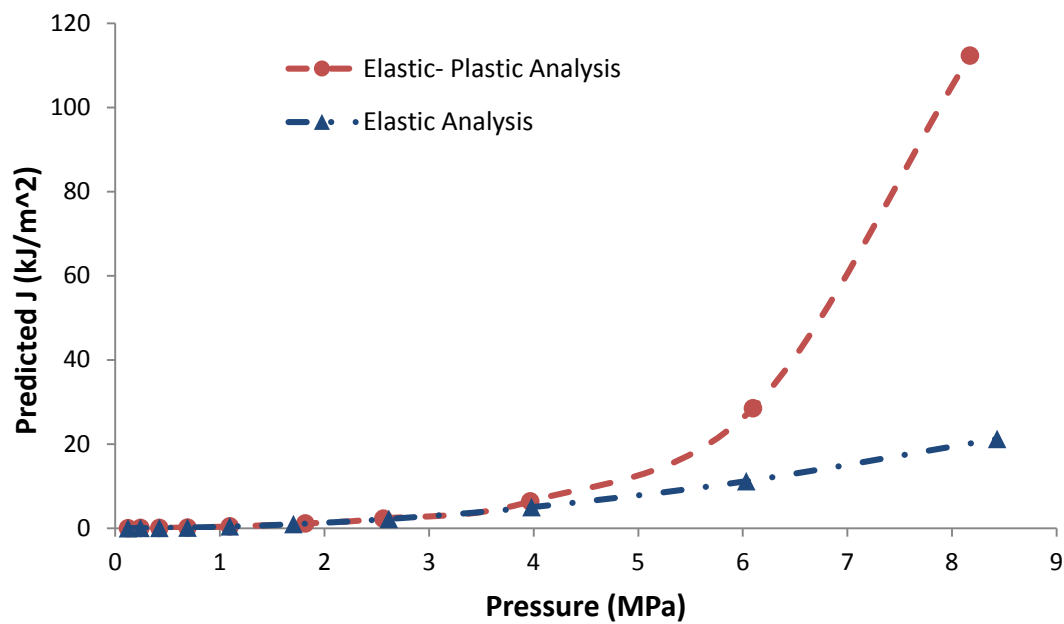


Figure 4-7- Predicted J integral value for elastic and elastic-plastic analysis (47%WT)

The crack tip was modeled as a blunt notch with a radius of approximately 10^{-3} times the estimated size of the plastic zone (r_p) for plane stress [93]. The r_p is the size of the plastic zone, and calculated as follows:

$$r_p = \frac{1}{2\pi} \left(\frac{K_I}{\sigma_y} \right)^2 \quad (4.2)$$

The notch should be small enough that under applied load, the deformed shape of the notch no longer depends on the geometry. The size of element around the notch has to be about $1/10^{\text{th}}$ the notch-tip radius to calculate accurate results. The crack tip and crack front is shown in Figure 4-8.

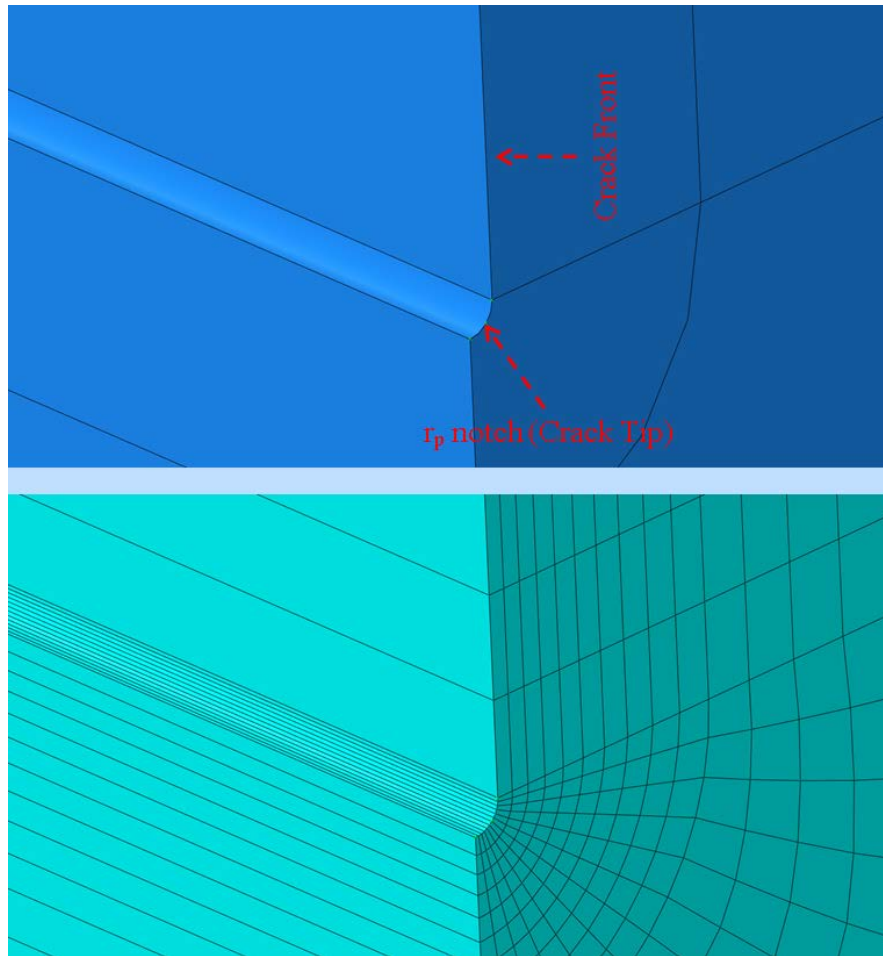


Figure 4-8- The Crack Tip and Crack Front for the EPFM Analysis

The J-integral is a measure of the strain energy density around the crack tip, applicable to cases where there is a large amount of plasticity in the vicinity of the crack tip. The benefit of the J-integral is that it is path independent and can be calculated analytically if the stress and strain distributions around the crack are known. Finite Element analysis can be applied when a special crack tip mesh is used. In LEFM, the mesh includes concentric rings of elements with the elements collapsed at the crack tip to model the stress distribution. The J-integral can be evaluated numerically at each concentric ring of elements, and converges to a constant value after several contours. In the current study, it was found that the J-integral magnitude converged after the 10th contour (Figure 4-9) and an average of the converged values was used for the J-integral. The convergence criterion was determined by evaluating the model at the predicted failure pressure of the flaw to ensure convergence of the J-integral value for the scenarios considered.

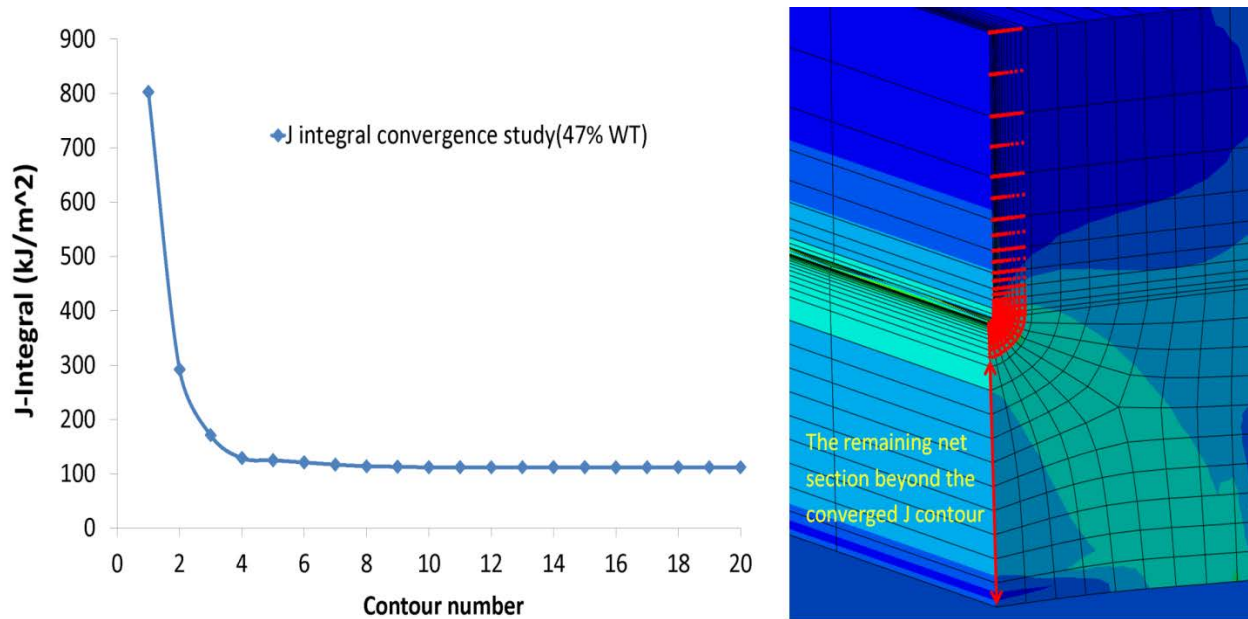


Figure 4-9- J Contour convergence and the remaining net section beyond the converged J Contour (average stress calculated for this section)

A three-dimensional quarter symmetry model (Figure 4-10) was used to simulate a longitudinal (axially) oriented surface crack in a thin-walled pipe. Twenty-node quadratic brick elements (C3D20R) with reduced integration were used, as recommended [93] for 3D modeling, and for large strain problems giving more accuracy and reduced computation time. The three-dimensional meshes consisted of 35198 hexahedral elements to simulate crack depths of 38%, 47% (Figure 4-10), 48%, 51% and 66% WT with twenty elements through the pipe wall thickness.

The model was designed to be parametric, and can be used for various crack depths and lengths.

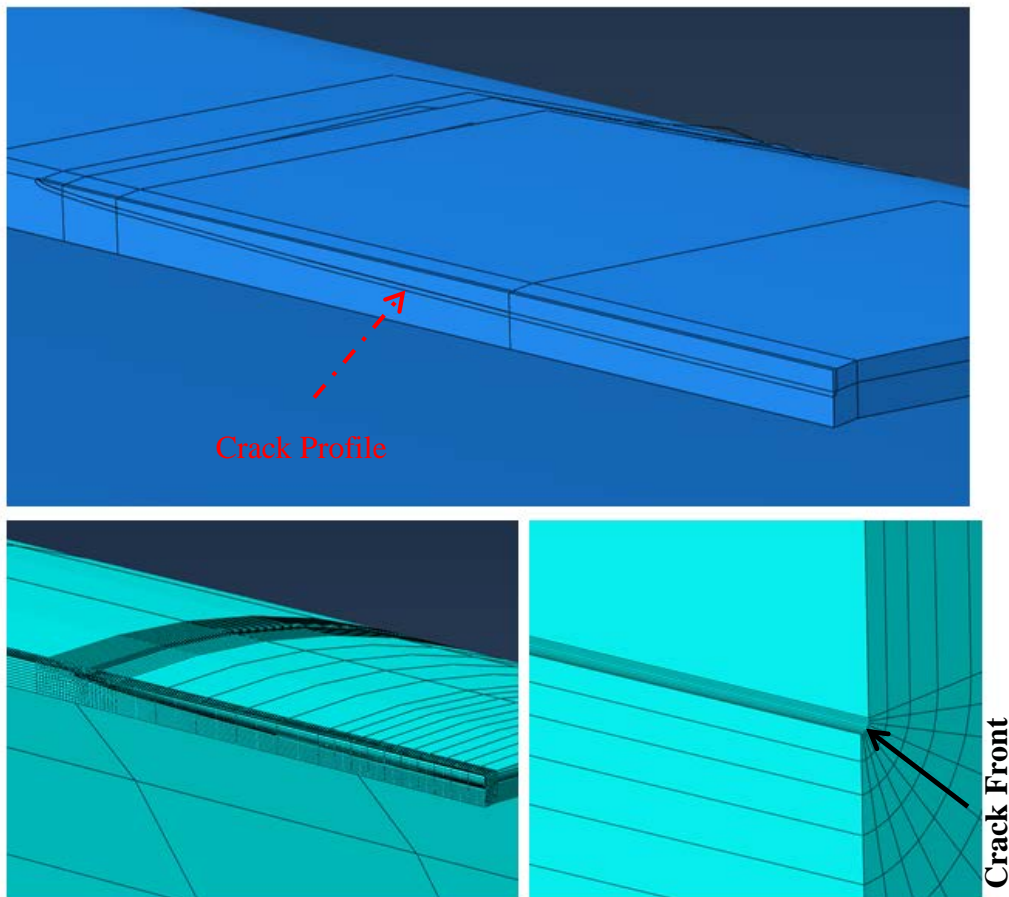


Figure 4-10- Quarter Symmetry Crack Model (47% WT) (Top: Geometry, Bottom Left: Crack, Right: Close view of crack tip mesh)

4.2.2 Collapse Pressure Prediction for a Crack Flaw

There are several methods or procedures proposed in the literature to predict the failure pressure of cracks in pipelines [11, 56, 60, 69, 90, 98, 104-107]. The conventional criterion for predicting the collapse pressure for longitudinal semi-elliptical cracks in pipelines is LEFM for low or moderate toughness materials, which generally corresponds to the older pipelines. These LEFM procedures are based on the limit load solution, which does not necessarily reflect the possibility for stable crack growth before ultimate failure, but crack propagation in low or moderate toughness materials is often negligible. However, high toughness materials such as newer pipelines, as in the present case, often exhibit some stable crack growth before ultimate failure, which must be addressed for accurate prediction of the collapse pressure. This is achieved through the use of EPFM and appropriate measures of toughness. Hence, the present crack flaws were evaluated in the same manner (EPFM), through application of the FAD approach to the FE model results.

There are several analytical methods available to evaluate crack or crack-like flaws. In the present work, the API 579 standard was applied, comprising 3 levels of assessment with sublevels. In general, the required level of the material and flaw data, and the accuracy of the prediction increase with increasing level. Level 1 FAD (Figure 2-37) which evaluates the failure pressure using a conservative rectangular envelope has been investigated as an application of the FE method to the FAD approach.

A semi-elliptical surface crack in a pipe under pressure can fail by a combination of plastic collapse and fracture. In general, failure in thin-walled pipe constructed of ductile steel is dominated by plastic collapse; however, some stable tearing can occur prior to ultimate failure. Since the stress intensity varies around the crack tip and is highest at the deepest point, as shown

in Figure 4-11, the crack typically grows in that direction first. The plastic zone at the crack tip generally extends through the remaining ligament leading to failure by plastic collapse. The prediction of failure using the finite element method is challenging since both modes of failure must be considered. Previous work considered a Modified Level 1 FAD approach [108] where by failure occurs only by plastic collapse or fracture (i.e. no combination as shown in Figure 2-38).

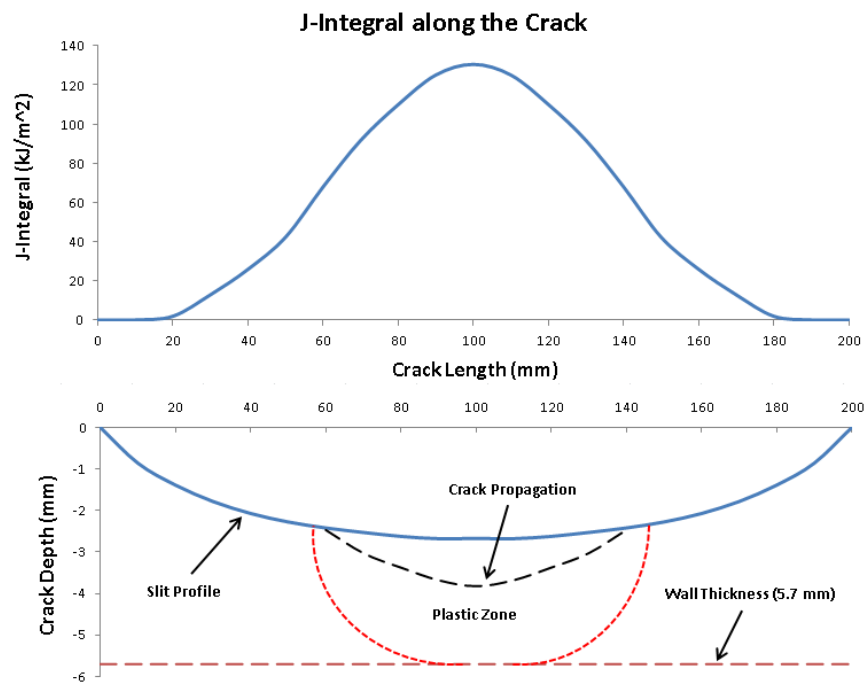


Figure 4-11- The J-Integral throughout the Semi-Elliptical Crack (47% WT)

To assess a particular flaw, the average von-Mises stress in the crack ligament and the converged J-integral value were used for comparison to the corresponding critical values. The values of stress and J-integral were evaluated from the model in the region where the J-integral values had converged. This was generally beyond the 10th contour, or 10th ring of elements around the crack tip (Figure 4-9). For the assessment methods where K (LEFM) was required, an

elastic analysis was used. In all cases, the stresses were determined from the elastic-plastic FE analysis.

Application of FE models with the FAD approach requires the definition of K_r and L_r , which vary for the different FAD levels. It was noted that the elastic FE model predictions were in agreement with the analytical elastic solution for K (semi-elliptical crack, cylinder method [1]) as expected, verifying the geometry and FE implementation. Three levels were considered for predicting the failure pressure of flaws in this study namely FEM API Level 1, FEM API Level 3 B and FEM Level 3 D.

In general, a Level 1 FAD is the most conservative method [7] using elastic stress intensity and an effective ligament stress. This has been successfully adapted using FEM by Bedairi et al [108] and revised in the current study using elastic-plastic analysis for the J-integral (Equation (4.2)) and the ligament stress (Equation (4.3b)) (Appendix A) to demonstrate the applicability of this method.

For the FEM Level 3 FAD approach (Methods B and D), the FAD was defined using the actual tensile stress-strain data for the pipe. The K_r ratio was defined as the ratio of the converged elastic-plastic J_{Total} (Figure 4-9) to that of the critical value (e.g. J_Q) (Equation (4.2)). The L_r ratio was predicted using the average von-Mises stress in the remaining flaw ligament over the region where the J-integral value had converged. For the flaw geometries considered in this study, the highest stresses were at the quarter symmetry point in the model (i.e. at the deepest point in the crack). It is important to note that the API code often compares the stress in the ligament, approximated using the reference stress to the yield stress (e.g. net section yielding) (Equation (4.3a)). However, the maximum allowable value (L_r Max) is greater than unity and depends on the material work hardening prior to failure. The actual stress-strain curve of the

material was used in the FEM analysis and the ligament stress (σ_{Ligament}) was determined from the finite element model results, using the average stress through the thickness of the ligament for elements in the converged J Integral zone (Equation (4.3b)).

$$K_r = \sqrt{\frac{J_{\text{Total}}}{J_Q}} \quad (4.2)$$

$$L_r = \frac{\sigma_{\text{Reference}}}{\sigma_y} \quad (4.3a)$$

$$L_{r \text{ FE}} = \frac{\sigma_{\text{Ligament}}}{\sigma_y} \quad (4.3b)$$

To predict the failure pressure of the cracked pipe for FEM Level 3 Method B, a loading path for the crack configuration was constructed on the K_r vs. L_r diagram. The intersection of the loading path with the failure line (Level 3 FAD) defined the predicted failure pressure. Equation (4.2) was applied to determine K_r using the measured J_Q value of $197 \text{ MPa}\sqrt{\text{m}}$. In the finite element analyses, the reference stress (Equation (4.3a)) was replaced with the average von-Mises stress in the ligament from the elastic-plastic analysis (Equation (4.3b)).

As noted above, application of FEM Level 3, Method D requires additional information in the form of the material resistance or J-R curve (e.g. Figure 2-30). This is much more challenging to assess with FE models since it requires extension of the crack to determine the point of instability. Method D was investigated using the FE method for single crack geometry by creating several finite element models with crack depths corresponding to the crack extension in the J-R curve test data.

4.2.3 Comparison between Experimental, Analytical, and FEM Results

API 579 Level 1, Level 3 B and Level 3 D procedures were applied to the experimental test data. For Level 1 (Appendix A), the predicted failure pressures were conservative by 39.6%. For Level 3 B, a loading path for each crack configuration was constructed on the L_r versus K_{Ic} plot (Figure 4-12) and the failure pressure was defined by the intersection of this loading path with the fracture assessment curve using the a fracture toughness $K_{Ic}=89 \text{ MPa m}^{0.5}$ (Table 4-2). The average difference based on the experimental test data was 30.4%, or under-prediction of the failure pressure. Similarly, the API 579 Level 3 Method D (Figure 4-13), which uses the tearing resistance curve (J-R curve), was applied to the cracks. This resulted in predictions that were 14.4% conservative on average which expected. This is expected, since use of the J-R curve is generally acknowledged to provide a more accurate prediction of failure for ductile materials.

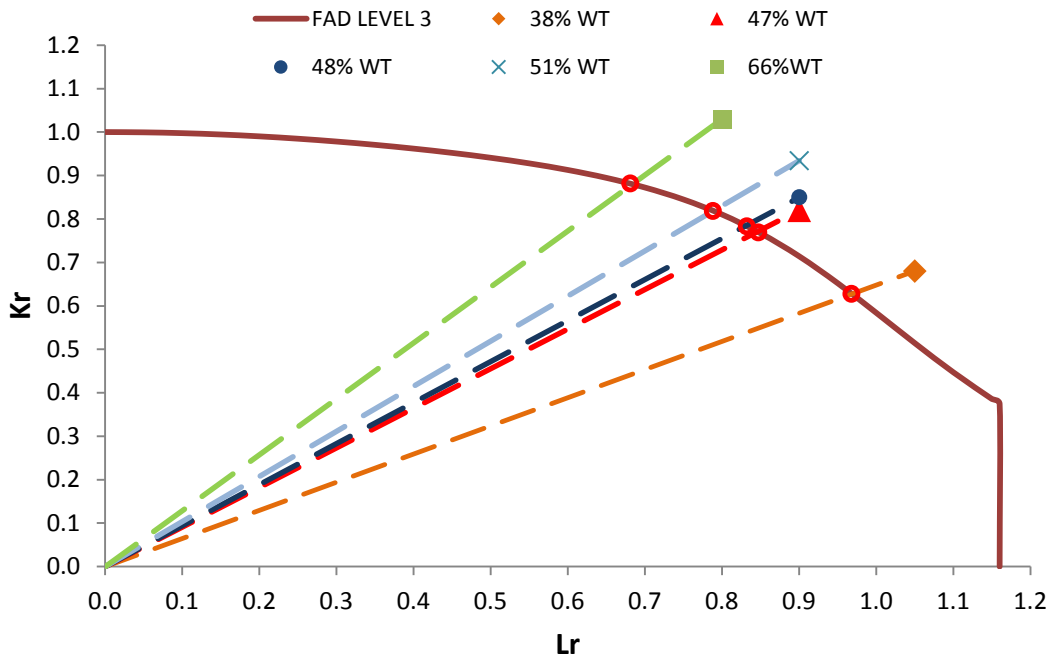


Figure 4-12- Failure Pressure Prediction for Cracks using API579 Level 3 FAD Method B

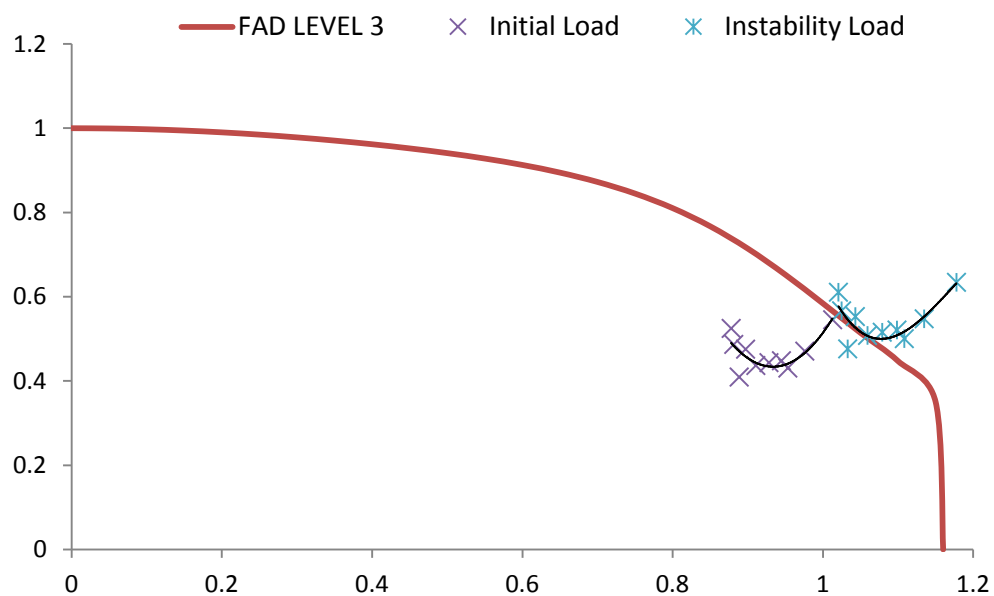


Figure 4-13-Failure Pressure Prediction for Cracks using API579 Level 3 FAD (Method D) (47%WT)

Table 4-2- API Failure Pressure predictions for Crack Flaws

Test No.	Crack Depth (a) %	Failure Pressure (MPa) Exp.	Predicted Failure Pressure (MPa)		Difference (%)	
			API 579 Level 3		API 579 Level 3	
			Method B		Method D	
			Method B		Method D	
CR1	38	10.1	7.87	8.80	22.1	12.9
CR2	47	9.30	6.47	7.74	30.4	16.8
CR3	48	9.60	6.31	7.72	34.3	19.6
CR4	51	8.83	5.85	7.53	33.7	14.7
CR5	66	6.49	4.45	5.96	31.4	8.2
			Average		30.4	14.4

An elastic-plastic FE analysis was applied using the crack geometries for the prediction of K_r , calculated as the square root of the ratio of total J_{Total} to J_Q (Equation (4.2)), where J_Q was determined from the sub-sized sample tests and found to be 197 kJ/m^2 . The improved estimate of stress and stress intensity in the ligament from the FE analysis improved the average conservative prediction for a Level 1 approach from 39.6% for the API Level 1 to 23.5% for the FEM API Level 1 (Appendix A), in agreement with previous studies [60, 108].

For Level 3, Method B the FE results were used to plot a load line (Figure 4-14) for each case, which was not linear since the stress analysis and therefore L_r and K_r were not linear. The intersection of the load line with the FAD provided the failure pressure prediction, given in Table 4-3. The predicted failure pressures were 21.4% conservative on average, reducing the conservatism by 9% compared to API Method B. In a separate analysis, it was noted that using the improved ligament stresses (Equation (4.3b)) accounted for approximately half of the improved prediction, while the balance was due to the use of J_{Total} value (Equation (4.2)).

Application of the FE method to Level 3 D required the development of ten additional crack meshes with crack extensions corresponding to the J-R curve data. Each model was then analyzed as elastic-plastic and the resulting K_r - L_r data was plotted on the FAD to identify the tangency point and the collapse pressure. The result (12.4% conservative, CR2) (Table 4-3) was less conservative than API Level 3 Method D (16.8%) for the same test. However, this approach required significant time and effort to generate and analyze the models.

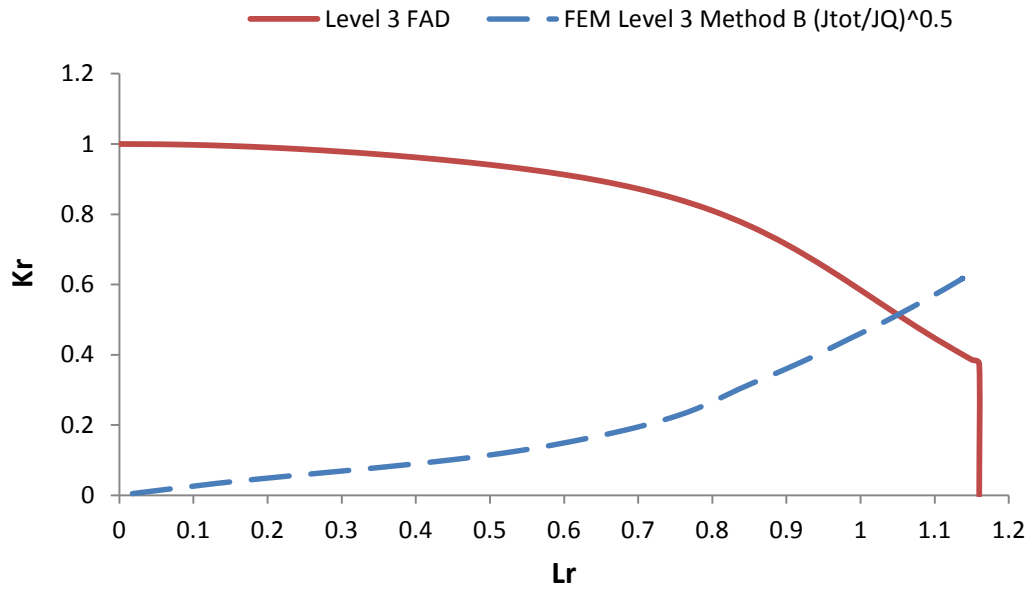


Figure 4-14- FE Analysis for FEM Level 3 FAD Method B API 579 (47% WT)

Table 4-3- FEM Failure Pressure predictions for Crack Flaws

Test No.	Crack Depth (a)	Failure				
		Pressure (MPa) Exp.	Predicted Failure Pressure (MPa)		Difference (%)	
			FEM	FEM	FEM	FEM
			API 579	API 579	API 579 Level	API 579 Level
			Level 3	Level 3	3	3
			Method B	Method D	Method B	Method D
CR1	38	10.1	8.09		19.9	-
CR2	47	9.30	7.17	8.15	22.9	12.4
CR3	48	9.60	7.04		26.7	-
CR4	51	8.83	7.26		17.8	-
CR5	66	6.49	5.21		19.7	-
Average					21.4	

The API579 Level 3 FAD Method D provides better agreement with experimental data in comparison with Level 3 FAD Method B. However, Level 3 Method B needs less data than Method D. Method D is based on the ductile tearing analysis and requires more material characterization data such as the J-R curve.

FEM API Level 3 FAD Method B showed better agreement than Level 3 FAD Method B with the experimental data. It should be noted that accurate prediction of the failure load is dependent on accurate modeling of the crack geometry, material properties and boundary conditions. Therefore, the FEM method does not provide accurate results whereas insufficient or non-accurate data.–FEM Level 3 FAD Method D provides a slightly better agreement with the experimental data than FEM Level 3 Method B, but requires much more time for finite element modeling and analysing.

In general, material characterization for the thin-walled pipes is not as simple full size pipe sections. For instance, this study revealed that J_{IC} cannot be measured for 5mm thickness pipes. Moreover, the measurement of the crack size is another challenging for the thin-walled pipes. On the other hand, the levels of accuracy of the proposed methods for evaluation of crack flaws are dependent on the material characterization and geometry measurements.

To summarize, API Level 3 Method D and FEM Level 3 FAD Method B are the more desirable methods for assessing crack flaws. Either method can be applied based on the availability of the crack size, material properties, time and budget.

4.3 Crack in Corrosion (CIC) Flaws

4.3.1 Crack in Corrosion (CIC) Flaws- Finite Element Model Development

Considering that the CIC models have a corrosion flaw with a flat bottom and a uniform depth crack, the boundary conditions, material properties and type of elements were the same as the crack or corrosion models. The same procedures based on the corrosion and crack models were then applied to develop a CIC flaw (Figure 4-15).

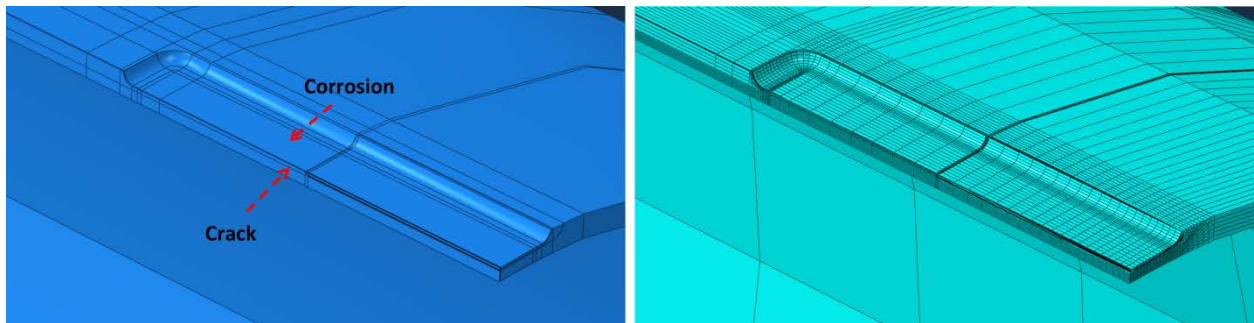


Figure 4-15- CIC Quarter Model (Left: Geometry, Right: FE Mesh)

4.3.2 Comparison between Experimental, Analytical, and FEM Results

The CIC flaws were evaluated using the API Level 3 Method B approach, which accounted for corrosion through a reduction in the pipe wall thickness equal to the corrosion depth. Thus, the CIC flaws were treated as a crack in reduced wall thickness pipe with the same remaining ligament as the original CIC flaw (Figure 4-16). The relevant dimensions and predicted collapse pressures are given in Table 4-4. A fracture toughness of $K_{IC}=89 \text{ MPa m}^{1/2}$

was applied, which was determined from the Charpy upper shelf energy for the pipe.

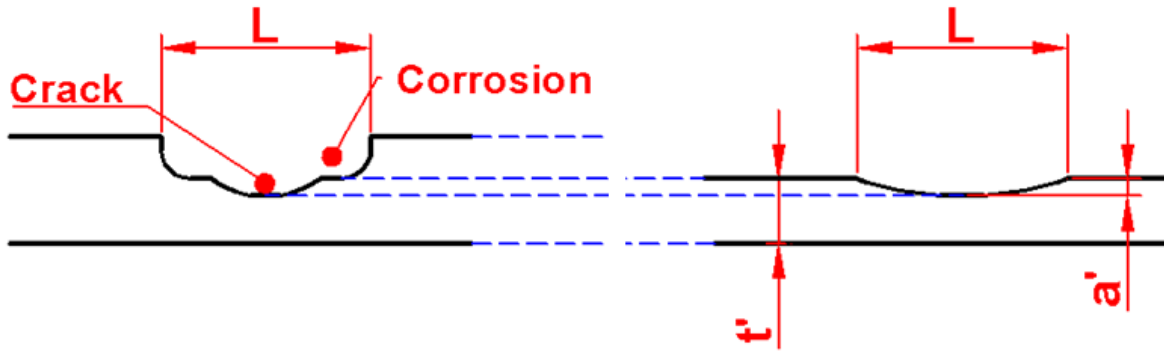


Figure 4-16-Crack in Corrosion (left) and Equivalent Cracks in the Remained Pipe Section Profile

Table 4-4- CIC Flaw Dimensions for API analysis

Test ID	CIC Flaw			Equivalent Crack with Thinner WT		
	Equivalent WT (t) (mm)	Total Equivalent Flaw Depth (a) (mm)	(a/t)%	Equivalent WT (t') (mm)	Total Equivalent Flaw Depth (a') (mm)	(a'/t')%
CIC 1	5.7	2.96	52	3.68	0.95	26
CIC 2	5.7	3.36	59	3.61	1.28	35
CIC 3	5.7	3.42	60	3.44	1.16	34
CIC 4	5.7	3.55	62	3.40	1.25	37
CIC 5	5.7	3.76	66	3.25	1.32	40

Level 3 FAD Method B and Method D were applied to predict the collapse pressure of CIC flaws considering the CIC flaws as cracks with the reduced wall thickness. On average they were 25.1% conservative for Level 3 FAD Method B, whereas Level 3 FAD Method D was 15.9% conservative (Table 4-5).

One benefit of the FE method was that the whole flaw (crack in corrosion) could be analyzed without any geometric simplifications. The FE predictions (Table 4-6) were conservative by 11.0% for Method B using the measured J_Q value, demonstrating improved prediction capability.

Table 4-5- API Failure Pressure predictions for CIC Flaws

Test No.	Crack Depth (a) %WT	Failure Pressure (MPa)	Predicted Failure Pressure (MPa)		Difference (%)	
		Experimental	API 579 Level 3 Method B	API 579 Level 3 Method D	API 579 Level 3 Method B	API 579 Level 3 Method D
CIC1	26	7.74	6.28	6.59	18.9	14.9
CIC2	35	6.72	5.40	6.16	19.6	8.3
CIC3	34	7.06	5.29	5.91	25.1	16.3
CIC4	37	7.89	5.03	5.74	36.2	27.2
CIC5	40	6.15	4.56	5.35	25.8	13.0
Average					25.1	15.9

Table 4-6- FEM Failure Pressure Predictions for CIC Flaws

Test No.	Crack Depth (a) %WT	Failure Pressure (MPa)	Predicted Failure Pressure (MPa)		Difference (%)
		Experimental	FEM API 579 Level 3 Method B	FEM API 579 Level 3 Method B	FEM API 579 Level 3 Method B
CIC1	26	7.74	6.69		13.6
CIC2	35	6.72	6.51		3.1
CIC3	34	7.06	6.45		8.6
CIC4	37	7.89	6.23		21.0
CIC5	40	6.15	5.63		8.5
Average					11.0

The use of J_{Total} , and J_Q in Level 3 Method B reduced the conservatism in the predicted values by 9%, on average for the crack flaws and by 14%, on average for the CIC flaws. Interestingly, correlations currently exist for a critical J value as a function of the Charpy impact energy. Using the correlation from Mak and Tyson [9], the corresponding J value is 97 kJ/m^2 and applying this in the elastic-plastic analysis provided more conservative predictions than the standard API Method B approach, supporting the present hypothesis that the measured J_Q value, using sub-sized samples, provides a more relevant estimate of the stress intensity at the crack tip for thin-walled pipe.

There may be some limitations to the current study regarding the number of experimental tests; however, this is often a limitation for work involving full-scale rupture testing. Importantly, the present work has covered a practical range of crack depths, and demonstrated consistency in the results over this range. In the proposed approach, the $L_r \text{ Max}$ value was increased based on the true stress-strain response of the pipe material, which is consistent with approaches used to predict plastic collapse in corrosion flaws. However, all crack flaws in the present study were predicted to fail at L_r ratios below $L_r \text{ Max}$, so this approach is not fully validated for crack flaws. It is proposed that J_Q is measured on sub-sized test samples, with the cracks oriented as surface flaws, as in practice. It is well known that J_Q is different than the material value that would be obtained in qualified test samples and that this value may be directly applicable to pipes of similar thickness and material properties.

4.3.3 CIC Parametric Study

CIC flaws consist of cracks within corrosion (Figure 4-17). It was found that the failure pressure for CIC flaws varied between a long uniform depth crack and long uniform corrosion

flaw [103], therefore, the relative amounts (percentage) of crack and corrosion depth plays a major role in the collapse pressure of a CIC flaw.

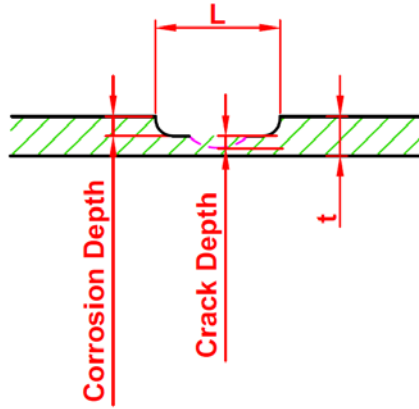


Figure 4-17-Transverse View through CIC Flaw

A test matrix was designed to provide a further understanding of CIC flaw failure behavior. The test matrix contained the cracks and corrosion of equivalent depth and length. Moreover, the test matrix also included the CIC flaws of varying crack and corrosion depths. The length of all the flaws 200 mm. The first aspect of this study considered 20%WT total flaw depth of varying crack and corrosion depths shown in Table 4-7 below.

Table 4-7-Test Matrix for CIC Parametric Study

Test No.	Crack (%WT)	Corrosion (%WT)	Total Depth (%WT)
1	0	20	20
2	5	15	20
3	10	10	20
4	15	5	20
5	20	0	20

The failure pressure prediction for cracks and corrosion only flaws was determined based on API Level 3 FAD Method D and CPS respectively. The failure pressure for CIC flaws was determined based on the method proposed in the previous section. According to this procedure, a

CIC flaw can be assumed as a crack flaw with the thinner wall thickness based on the corrosion depth. This is given in Table 4-8.

Table 4-8- Parametric Study for CIC Flaws (20% WT)

Test ID.	Crack (%WT)	Corrosion (%WT)	Total Depth (%WT)	Pipe Thickness (mm)	Equivalent Pipe Thickness (mm)	Equivalent Crack Depth (mm)	a'/t' (%WT)	Failure Pressure (MPa)
CIC-20-1	0	20	20	5.7	4.56	0	0.0	12.2
CIC-20-2	5	15	20	5.7	4.845	0.285	5.9	11.5
CIC-20-3	10	10	20	5.7	5.13	0.57	11.1	11.3
CIC-20-4	15	5	20	5.7	5.415	0.855	15.8	11.2
CIC-20-5	20	0	20	5.7	5.7	1.14	20.0	11.1

The results also are shown in Figure 4-18.

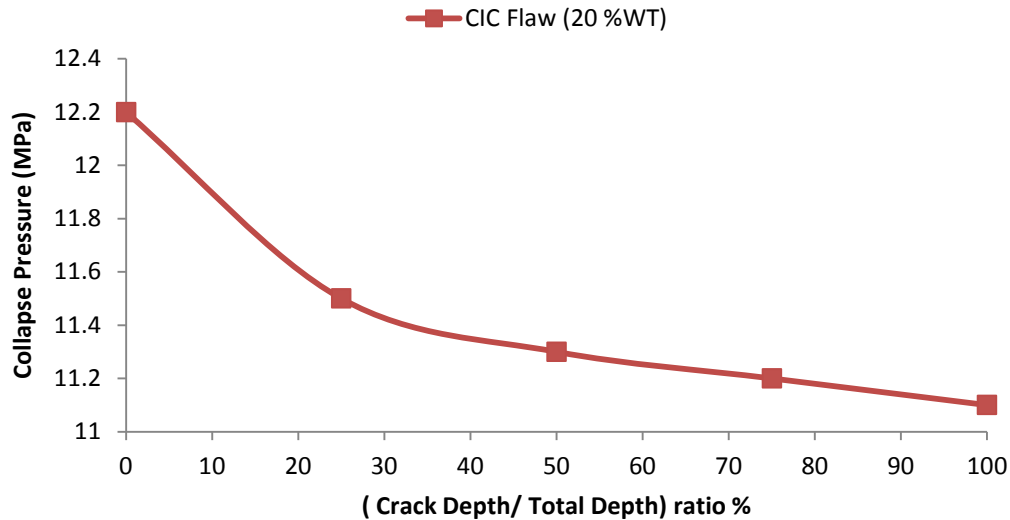


Figure 4-18- Collapse Pressure Prediction for CIC Flaws of Varying Different Crack & Corrosion Ratio for Total Depth of (20%WT)

The same procedure and test matrices were applied for the parametric study of CIC flaws for total 40% WT. The results are shown in Table 4-9 and Figure 4-19.

Table 4-9- Parametric Study for CIC Flaws (40%WT)

Test ID.	Crack (%WT)	Corrosion (%WT)	Total Depth (%WT)	Pipe Thickness (mm)	Equivalent Pipe Thickness (mm)	Equivalent Crack Depth (mm)	a'/t' (%WT)	Collapse Pressure (MPa)
CIC-40-1	0	40	40	5.7	3.42	0	0.0	12.2
CIC-40-2	5	35	40	5.7	3.705	0.18525	7.7	8.6
CIC-40-3	10	30	40	5.7	3.99	0.399	14.3	8.5
CIC-40-4	15	25	40	5.7	4.275	0.64125	20.0	8.4
CIC-40-5	20	20	40	5.7	4.56	0.912	25.0	8.4
CIC-40-6	25	15	40	5.7	4.845	1.21125	29.4	8.4
CIC-40-7	30	10	40	5.7	5.13	1.539	33.3	8.3
CIC-40-8	35	5	40	5.7	5.415	1.89525	36.8	8.4
CIC-40-9	40	0	40	5.7	5.7	2.28	40.0	8.4

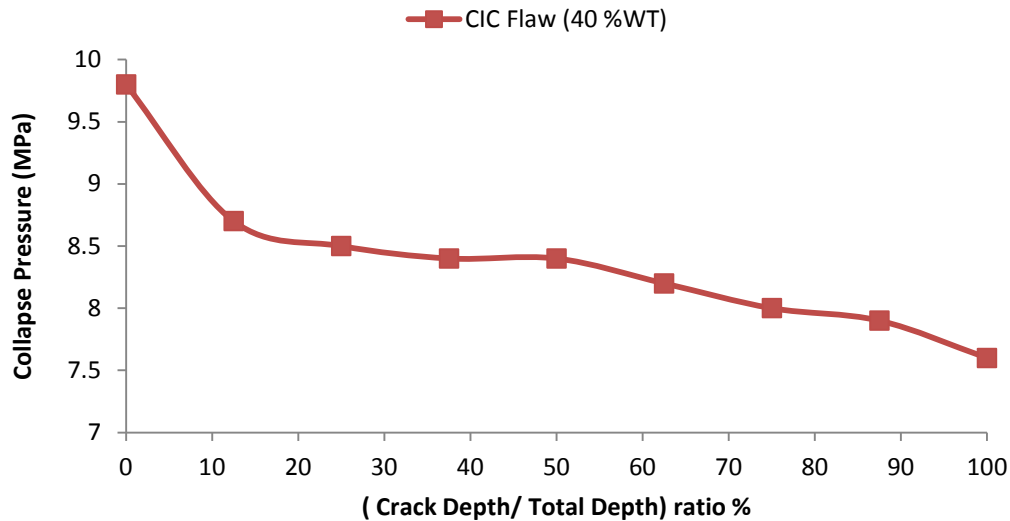


Figure 4-19- Collapse Pressure Prediction for CIC Flaws of Varying Different Crack & Corrosion Ratio for Total Depth of (40%WT)

The results showed that the crack only data is more critical than the corrosion only flaw of equivalent depth. However, this is not always the case for other flaws, which contain a crack

coincident with corrosion since by increasing the crack depth, the collapse pressure would not necessarily decrease in a CIC flaw. For instance, the total depth for both CIC-40-7(Cr30%+C10%) and CIC-40-8 (Cr 35%+C 5%) is 40% WT. Yet comparison of the predicted collapse pressures for CIC-40-7 and CIC-40-8 shows that CIC-40-8 is more critical than the CIC-40-7. It is apparent that in addition to the crack to corrosion ratio, other parameters such as pipe thickness, total depth and length of CIC flaw, pipe diameter and material properties determine the collapse pressure of the flaw.

It is worth noting that by changing the pipe wall thickness and corrosion depth, the type of failure may be changed for the CIC flaws. For instance, the failure for a pipe containing a 20% WT crack with 40 mm wall thickness will occur due to fracture collapse, however, for the same pipe containing a CIC flaw (Cr 20%+ C 40%), failure will occur by the plastic collapse. On eliminating the corrosion depth; the equivalent pipe thickness would be 12 mm which changes the pipe from thick wall into thin-wall.

Chapter 5

Conclusions and Future Work

5.1 Conclusions

- ❖ Experimental rupture tests were conducted to investigate the failure behavior of longitudinally oriented corrosion, crack and CIC flaws in two different line pipes (20 and 36 inch diameter).
- ❖ Tensile, Charpy, and J tests were carried out on the pipe sections to measure the material properties.
- ❖ Toughness measured using J testing on samples that failed to meet the E1820-11 size requirements resulted in geometry dependent properties. However, if the samples were the same thickness as the pipe wall, the measured J value was consistent with the

conditions experienced in the pipe wall when a crack was present. Toughness can be characterized using the J_Q value.

- ❖ Corrosion flaws may fail by plastic collapse due to ductile tearing. The FEM method was more accurate compared to the experimental results with an average difference of 3.2%. Moreover, the CPS method provided more accurate collapse pressure predictions (13.5%) compared to RSTRENG (24.2%). The CPS method uses a more complete description of the material response and surrounding material loss in comparison to RSTRENG. Also there is no need to consider flaw interaction rules, since the interaction of adjacent corrosion is considered without simplification.
- ❖ Cracks may fail by plastic collapse or fracture, which can be predicted using the Failure Assessment Diagram. API Level 3 FAD Method D was found to be the most accurate with an average difference of 14.4% compared to API Level 3 FAD Method B for the evaluation of cracks. However both API Level 3 FAD Methods B and D are limited for thin-walled pipe.
- ❖ The use of J_Q in the FEM API Level 3 FAD Method B provided improved estimates of the collapse pressure in comparison with API Level 3 FAD Method B with average differences of 21.4% and 30.4% respectively, while still remaining conservative.
- ❖ API Level 3 FAD Method D requires the use of the material R curve and consideration of the crack extension. Evaluation of a flaw using FEM with Level 3 FAD Method D is possible. However, it is time consuming compared to Level 3 FAD Method B since multiple FE models are required. The prediction result (12.4% conservative, CR2) was less conservative than API Level 3 FAD Method D (16.8%) for the same test.

- ❖ A CIC flaw can be treated as a crack in a pipe with the wall thickness reduced by the depth of the corrosion for application of the API procedure
- ❖ On average analytical failure prediction results were 25.1% conservative for API Level 3 FAD Method B, whereas the pressures were 15.9% conservative for API Level 3 FAD Method D.
- ❖ Application of the FE method to CIC using the predicted ligament stresses and J_Q resulted in improved estimates of the collapse pressure with an average difference of 11% compared to the standard reference stress.
- ❖ The percentage of crack to corrosion depth ratio is a major role in the failure behavior of the CIC flaw. Another important factor is the pipe wall thickness.

5.2 Recommendations and Future Work

Future work will include a larger number of tests to improve the statistical accuracy of the experimental tests. It is also recommended that the parametric study be performed on CIC flaws to figure out the effect of flaw geometry such as length and depth on the failure behaviour of CIC flaws. Moreover, the effect of material properties such as fracture toughness on the failure prediction could be significant, and should be investigated for the thin-walled pipelines.

References

1. API 579, *Recommended Practice for Fitness for Service*, American Petroleum Institute, 2000.
2. BS 7910, *Guide on Methods for Assessing the Acceptability of Flaws in Metallic Structures*, British Standard Institute, 1999.
3. Escoe, A.K., *Piping and Pipeline Assessment Guide*. Vol. 1. 2006: Gulf Professional Publishing.
4. Jaske, C., *Corlas 1.0 User Manual Computer Program for Corrosion-Life Assessment of Piping and Pressure Vessels*, Version.
5. Hosseini, A., *Assessment of Crack in Corrosion Defects in Natural Gas Transmission Pipelines*, 2010, MASc Thesis, University of Waterloo.
6. Association, C.S., *Steel Pipe*, 2002.
7. Folga, S., *Natural Gas Pipeline Technology Overview*, 2007, Argonne National Laboratory (ANL).
8. ASTM E 1820-11, *Standard Test Method for Measurement of Fracture Toughness*, Annual book of ASTM standards, 2011.
9. Mak, D.K. and Tyson, W.R. *Material Assessment of Canadian Saw Line-Pipes*. in IPC. 1998.
10. Anderson, T.L., *Fracture Mechanics: Fundamentals and Applications*. 1995: CRC Press LLC.
11. Oh, C.-S., Kim, N.-H., Kim, Y.-J., Baek, J.-H., Kim, Y.-P., and Kim, W.-S., *A Finite Element Ductile Failure Simulation Method Using Stress-Modified Fracture Strain Model*. Engineering fracture mechanics, 2011. **78**(1): p. 124-137.

12. Parton, V.Z., Morozov, E.M., and Hetnarski, R.B., *Mechanics of Elastic-Plastic Fracture*. 1989: Hemisphere Pub. Corp.
13. Benham, P. and Crawford, R., *Mechanics of Engineering Materials*. 1987, New York: John Wiley.
14. Griffith, A.A., *The Phenomena of Rupture and Flow in Solids*. Philosophical transactions of the royal society of london. Series A, containing papers of a mathematical or physical character, 1921. **221**: p. 163-198.
15. Dowling, N.E., *Mechanical Behavior of Materials: Engineering Methods for Deformation, Fracture, and Fatigue*. 1993: Prentice Hall Englewood Cliffs, NJ.
16. Irwin, G.R., *Fracture Mechanics*. Report of Nrl Progress, 1973(JUL): p. 35-37.
17. Inglis, C., *Stresses in a Plate Due to the Presence of Cracks and Sharp Corners*. SPIE MILESTONE SERIES MS, 1997. **137**: p. 3-17.
18. Michael Janssen, J.Z., Russell and Wanhill, *Fracture Mechanics*. Second ed. 2002: Span press.
19. Zhenhua Yi, S.S., *Thickness Effect on Fracture Toughness and Plastic Zone Size in International Conference on Mechanical, Industrial, and Manufacturing Technologies (MIMT 2010)*2010, ASME: Sanya, China.
20. ASTM E 399-11, *Standard Test Method for Plane Strain Fracture Toughness of Metallic Materials*, Annual book of ASTM standards, 2011.
21. Wells, A. *Unstable Crack Propagation in Metals: Cleavage and Fast Fracture*. 1961.

22. Burdekin, F.M. and STONE, D.E.W., *The Crack Opening Displacement Approach to Fracture Mechanics in Yielding Materials*. The Journal of Strain Analysis for Engineering Design, 1966. **1**(2): p. 145-153.
23. Hutchinson, J., *Singular Behaviour at the End of a Tensile Crack in a Hardening Material*. Journal of the Mechanics and Physics of Solids, 1968. **16**(1): p. 13-31.
24. Rice, J. and Rosengren, G., *Plane Strain Deformation near a Crack Tip in a Power-Law Hardening Material*. Journal of the Mechanics and Physics of Solids, 1968. **16**(1): p. 1-12.
25. Anderson, T., *Elastic-Plastic Fracture Mechanics: A Critical Review*, in SSC-3451990.
26. McMeeking, R. and Parks, D., *On Criteria for J-Dominance of Crack-Tip Fields in Large-Scale Yielding*. Elastic-Plastic Fracture, ASTM STP, 1979. **668**: p. 175-194.
27. McClintock, F.A., *Plasticity Aspects of Fracture*. Fracture: an advanced treatise, 1971. **3**: p. 47-225.
28. Shih, C. and German, M., *Requirements for a One Parameter Characterization of Crack Tip Fields by the Hrr Singularity*. International Journal of Fracture, 1981. **17**(1): p. 27-43.
29. Anderson, T.L., *Crack Tip Parameters for Large Scale Yielding and Low Constraint Configurations*. International Journal of Fracture, 1989. **41**(2): p. 79-104.
30. Williams, M., *On the Stress Distribution at the Base of a Stationary Crack*. 1997.
31. Cotterell, B., Li, Q.F., Zhang, D.Z., and Mai, Y.W., *On the Effect of Plastic Constraint on Ductile Tearing in a Structural Steel*. Engineering fracture mechanics, 1985. **21**(2): p. 239-244.
32. Leever, P. and Radon, J., *Inherent Stress Biaxiality in Various Fracture Specimen Geometries*. International Journal of Fracture, 1982. **19**(4): p. 311-325.

33. Al-Ani, A. and Hancock, J., *J-Dominance of Short Cracks in Tension and Bending*. Journal of the Mechanics and Physics of Solids, 1991. **39**(1): p. 23-43.
34. O'dowd, N. and Shih, C., *Family of Crack-Tip Fields Characterized by a Triaxiality Parameter-- I. Structure of Fields*. Journal of the Mechanics and Physics of Solids, 1991. **39**(8): p. 989-1015.
35. O'dowd, N. and Shih, C., *Family of Crack-Tip Fields Characterized by a Triaxiality Parameter-- Ii. Fracture Applications*. Journal of the Mechanics and Physics of Solids, 1992. **40**(5): p. 939-963.
36. O'Dowd, N.P. and Shih, C.F., *Two-Parameter Fracture Mechanics: Theory and Applications*. Fracture Mechanics, 1994. **24**: p. 21-47.
37. Jayadevan, K., Thaulow, C., Østby, E., Berg, E., Skallerud, B., Holthe, K., and Nyhus, B., *Structural Integrity of Pipelines: T-Stress by Line-Spring*. Fatigue & Fracture of Engineering Materials & Structures, 2005. **28**(5): p. 467-488.
38. Thaulow, C., Østby, E., Nyhus, B., Zhang, Z.L., and Skallerud, B., *Constraint Correction of High Strength Steel:: Selection of Test Specimens and Application of Direct Calculations*. Engineering fracture mechanics, 2004. **71**(16-17): p. 2417-2433.
39. Zhu, X. and Jang, S., *Jr Curves Corrected by Load-Independent Constraint Parameter in Ductile Crack Growth*. Engineering fracture mechanics, 2000. **68**(3): p. 285-301.
40. Hancock, J.W., Reuter, W., and Parks, D.M., *Constraint and Toughness Parameterized by T*. ASTM SPECIAL TECHNICAL PUBLICATION, 1993. **1171**: p. 21-21.
41. Joyce, J.A. and Link, R.E., *Effects of Constraint on Upper Shelf Fracture Toughness*. ASTM SPECIAL TECHNICAL PUBLICATION, 1995. **1256**: p. 142-177.

42. Joyce, J.A. and Link, R.E., *Application of Two Parameter Elastic-Plastic Fracture Mechanics to Analysis of Structures*. Engineering fracture mechanics, 1997. **57**(4): p. 431-446.
43. Marschall, C.W., Papaspyropoulos, V., and Landow, M.P., *Evaluation of Attempts to Predict Large-Crack-Growth Jr Curves from Small Specimen Tests*. Nonlinear Fracture Mechanics, 1989. **2**: p. 123-143.
44. Eisele, U., Roos, E., Seidenfuss, M., and Silcher, H., *Determination of J-Integral-Based Crack Resistance Curves and Initiation Values for the Assessment of Cracked Large-Scale Specimens*. ASTM SPECIAL TECHNICAL PUBLICATION, 1992. **1131**: p. 37-37.
45. Roos, E., Eisele, U., and Silcher, H., *Effect of Stress State on the Ductile Fracture Behavior of Large-Scale Specimens*. ASTM SPEC TECH PUBL, ASTM, PHILADELPHIA, PA(USA), 1993, 1993(1171): p. 41-63.
46. Elliot, C., Emark, M., and Lucas, G., *Development of Disk Compact Tension Specimens and Test Techniques for Hf⁺ Irradiation*. Journal of Nuclear Materials, 1991. **179**(Part A): p. 434-437.
47. Alexander, D.J., *Fracture Toughness Measurements with Subsize Disk Compact Specimens*. ASTM SPECIAL TECHNICAL PUBLICATION, 1993. **1204**: p. 130-130.
48. Yoon, K.K., Gross, L.B., Wade, C.S., and VanDerSluys, W.A., *Evaluation of Disk-Shaped Compact Specimen for Determining Jr Curves*. ASTM SPECIAL TECHNICAL PUBLICATION, 1995. **1256**: p. 272-283.
49. Pardoen, T., Marchal, Y., and Delannay, F., *Thickness Dependence of Cracking Resistance in Thin Aluminium Plates*. Journal of the Mechanics and Physics of Solids, 1999. **47**(10): p. 2093-2123.

50. Dodds, R.H., Ruggieri, C., and Koppenhoefer, K., *3-D Constraint Effects on Models for Transferability of Cleavage Fracture Toughness*. ASTM SPECIAL TECHNICAL PUBLICATION, 1997. **1321**: p. 179-197.
51. Henry, B., Luxmoore, A., and Sumpter, J., *Elastic-Plastic Fracture Mechanics Assessment of Low Constraint Aluminium Test Specimens*. International Journal of Fracture, 1996. **81**(3): p. 217-234.
52. Yuan, H. and Brocks, W., *Quantification of Constraint Effects in Elastic-Plastic Crack Front Fields*. Journal of the Mechanics and Physics of Solids, 1998. **46**(2): p. 219-241.
53. Zerbst, U., Schödel, M., Webster, S., and Ainsworth, R.A., *Fitness-for-Service Fracture Assessment of Structures Containing Cracks: A Workbook Based on the European Sintap/Fitnet Procedure*. 2007: Academic Press.
54. Miller, A., *Review of Limit Loads of Structures Containing Defects*. International journal of pressure vessels and piping, 1988. **32**(1-4): p. 197-327.
55. Goodall, I. and Webster, G., *Theoretical Determination of Reference Stress for Partially Penetrating Flaws in Plates*. International journal of pressure vessels and piping, 2001. **78**(10): p. 687-695.
56. Lei, Y., *J-Integral and Limit Load Analysis of Semi-Elliptical Surface Cracks in Plates under Tension*. International journal of pressure vessels and piping, 2004. **81**(1): p. 21-30.
57. ASTM E 8M, *Standard Test Method for Tension Testing of Metallic Materials*, Annual book of ASTM standards, 2009.
58. Cronin, D. and Pick, R., *Prediction of the Failure Pressure for Complex Corrosion Defects*. International journal of pressure vessels and piping, 2002. **79**(4): p. 279-287.

59. ASTM E 23, *Standard Test Method for Notched Bar Impact Testing of Metallic Materials*, Annual book of ASTM standards, 2007.
60. Bedairi, B., *Numerical Failure Pressure Prediction to Assess Crack in Corrosion Defects in Natural Gas Transmission Pipelines*, 2010, MASc Thesis, University of Waterloo.
61. Kao-Walter, S., Dahlström, J., Karlsson, T., and Magnusson, A., *A Study of the Relation between the Mechanical Properties and the Adhesion Level in a Laminated Packaging Material*. Mechanics of Composite Materials, 2004. **40**(1): p. 29-36.
62. Kao-Walter, S. and Ståhle, P., *Mechanical and Fracture Properties of Thin Al-Foil*. 2001: Blekinge Institute of Technology.
63. Kao-Walter, S., Ståhle, P., and Hägglund, R., *Fracture Toughness of a Laminated Composite*. European Structural Integrity Society, 2003. **32**: p. 355-364.
64. Arsene, S. and Bai, J., *A New Approach to Measuring Transverse Properties of Structural Tubing by a Ring Test*. Journal of testing and evaluation, 1996. **24**(6): p. 386-391.
65. Brown, W.F., *Review of Developments in Plane Strain Fracture Toughness Testing*. 1970: ASTM International.
66. Morozov, E. and Sapunov, V., *Fracture Toughness of Thin-Sheet Materials in the Process of Ductile Tear*. Materials Science, 2001. **37**(2): p. 272-278.
67. Pharr, G., Harding, D., and Oliver, W., *Measurement of Fracture Toughness in Thin Films and Small Volumes Using Nanoindentation Methods*. Mechanical properties and deformation behavior of materials having ultra-fine microstructures, 1993: p. 449-461.

68. Yagnik, S., Ramasubramanian, N., Grigoriev, V., Sainte-Catherine, C., Bertsch, J., Adamson, R., Kuo, R., Mahmood, S., Fukuda, T., and Efsing, P., *Round-Robin Testing of Fracture Toughness Characteristics of Thin-Walled Tubing*. J. ASTM Int, 2008. **5**(2): p. 1-216.
69. Dhia, A.B., Bai, J., and Francois, D., *3d Finite Element Analyses of a New Fracture Toughness Testing Method for Tubular Structures*. International journal of pressure vessels and piping, 1997. **71**(2): p. 189-195.
70. Evans, J., Kotsikos, G., and Robey, R., *A Method for Fracture Toughness Testing Cylinder Material*. Engineering fracture mechanics, 1995. **50**(2): p. 295-300.
71. Samal, M., Sanyal, G., and Chakravartty, J., *Estimation of Fracture Behavior of Thin Walled Nuclear Reactor Fuel Pins Using Pin-Loading-Tension (Plt) Test*. Nuclear Engineering and Design, 2010. **240**(12): p. 4043-4050.
72. BS 7448, *Fracture Mechanics Toughness Tests*, British Standard Institute, 2005.
73. Hosseini, A., Cronin, D., and Plumtree, A., *Crack in Corrosion Defect Assessment in Transmission Pipelines*. ASME Journal of Pressure Vessel Technology, 2013. **135**(2).
74. Cronin, D., *Assessment of Corrosion Defects in Pipelines*, 2001, Thesis, University of Waterloo.
75. Cosham, A., Hopkins, P., and Macdonald, K., *Best Practice for the Assessment of Defects in Pipelines-Corrosion*. Engineering Failure Analysis, 2007. **14**(7): p. 1245-1265.
76. ASME B 31G, *Manual for Determining the Remaining Strength of Corroded Pipelines*, ASME B31 code for pressure piping, 1991.
77. Kiefner, J. and Vieth, P., *A Modified Criterion for Evaluating the Strength of Corroded Pipe*. Final Report for Project PR, 1989. **3**: p. 805.

78. Ritchie, D. and Last, S., *Burst Criteria of Corroded Pipelines-Defect Acceptance Criteria*. Paper, 1995. **32**: p. 32-1.
79. Leis, B. and Stephens, D. *An Alternative Approach to Assess the Integrity of Corroded Line Pipe-Part I: Current Status*. 1997.
80. Leis, B. and Stephens, D., *An Alternative Approach to Assess the Integrity of Corroded Line Pipe-Part H: Alternative Criterion*. 1997.
81. CEPA, *Stress Corrosion Cracking Recommended Practices*, C.E.P. Association, Editor 2007.
82. Kiefner, J., Maxey, W., Eiber, R., and Duffy, A., *Failure Stress Levels of Flaws in Pressurized Cylinders*. ASTM Special Technical Publication 1973(536): p. 461-481.
83. Cravero, S. and Ruggieri, C., *Structural Integrity Analysis of Axially Cracked Pipelines Using Conventional and Constraint-Modified Failure Assessment Diagrams*. International journal of pressure vessels and piping, 2006. **83**(8): p. 607-617.
84. Rana, M.D. and Rawls, G.B., *Prediction of Fracture Stresses of High Pressure Gas Cylinders Containing Cracklike Flaws*. Journal of Pressure Vessel Technology, 2007. **129**: p. 639.
85. CEPA. *Canadian Energy Pipeline Association*. 2011.
86. Katz, D., Gao, M., Limon, S., and Krishnamurthy, R. *Advances in Crack Assessment for Pipeline Integrity*. 2005.
87. Shih, C. and Hutchinson, J., *Fully Plastic Solutions and Large Scale Yielding Estimates for Plane Stress Crack Problems*. Journal of Engineering Materials and Technology, 1976. **98**: p. 289.

88. Miki, C., Kobayashi, T., Oguchi, N., Uchida, T., Suganuma, A., and Katoh, A. *Deformation and Fracture Properties of Steel Pipe Bend with Internal Pressure Subjected to in-Plane Bending*. in 12th World Conference on Earthquake Engineering. 2000.
89. Laboratory, A.A.C.E.M.E.a.T. *Anderson Associates Consulting Engineering Metallurgical Engineers and Testing Laboratory*. Available from: <http://www.metaltest.com/>.
90. Chen, Y., *Finite Element Modeling of Ductile Tearing in Pipeline Steels Using a Micromechanical Damage Model*, 1969, PhD Thesis, University of Waterloo.
91. Chouchaoui, B., Pick, R., and Yost, D. *Burst Pressure Predictions of Line Pipe Containing Single Corrosion Pits Using the Finite Element Method*. 1992. American Society of Mechanical Engineers.
92. Fu, B. and Kirkwood, M.G. *Predicting Failure Pressure of Internally Corroded Linepipe Using the Finite Element Method*. 1995. American Society of Mechanical Engineers.
93. Dassault Systemes Simulia Corp., *Abaqus User's Manual for Version 6.10-Ef1*, 2010, Providence, RI, USA.
94. Mok, D., Pick, R., Glover, A., and Hoff, R., *Bursting of Line Pipe with Long External Corrosion*. International journal of pressure vessels and piping, 1991. **46**(2): p. 195-216.
95. Sattari-Far, I., *Finite Element Analysis of Limit Loads for Surface Cracks in Plates*. International journal of pressure vessels and piping, 1994. **57**(2): p. 237-243.
96. Alcott, W.J., *Defect Interaction and Plastic Collapse*, 1999, Thesis, University of Waterloo.
97. Crisfield, M., *A Fast Incremental/Iterative Solution Procedure That Handles*. Computers & Structures, 1981. **13**(1-3): p. 55-62.

98. Choi, J., Goo, B., Kim, J., Kim, Y., and Kim, W., *Development of Limit Load Solutions for Corroded Gas Pipelines*. International journal of pressure vessels and piping, 2003. **80**(2): p. 121-128.
99. Cronin, D.S. *Finite Element Analysis of Complex Corrosion Defects*. in ASME 2002 Pressure Vessels and Piping Conference. 2002. American Society of Mechanical Engineers.
100. Henshell, R. and Shaw, K., *Crack Tip Finite Elements Are Unnecessary*. International Journal for Numerical Methods in Engineering, 1975. **9**(3): p. 495-507.
101. Barsoum, R.S., *A Degenerate Solid Element for Linear Fracture Analysis of Plate Bending and General Shells*. International Journal for Numerical Methods in Engineering, 1976. **10**(3): p. 551-564.
102. Eshraghi, A.J., H., *Practical Finite Element Analysis* 2011.
103. Cronin, D. and Plumtree, A., *Assessment of Crack in Corrosion Defects in Natural Gas Transmission Pipelines, Confidential Report to Tcpl*, 2006.
104. Choi, J., *Investigation of Constraint Effects in Pipeline Fracture Specimens*, 1993, MAsC Thesis, University of Waterloo.
105. Choi, J., *Plastic Collapse of Circumferential Surface Defects in Pipeline Materials*, 1997, PhD Thesis, University of Waterloo.
106. Dotta, F. and Ruggieri, C., *Structural Integrity Assessments of High Pressure Pipelines with Axial Flaws Using a Micromechanics Model*. International journal of pressure vessels and piping, 2004. **81**(9): p. 761-770.

107. Shan, G.X.K., O. and Fischer, F.D., *A Numerical Study on the Crack Growth Behavior of a Low and a High Strength Steel*. International Journal of Fracture, 1996. **78**: p. 335-346.
108. Bedairi, B., Cronin, D., Hosseini, A., and Plumtree, A., *Failure Prediction for Crack-in-Corrosion Defects in Natural Gas Transmission Pipelines*. International journal of pressure vessels and piping, 2012. **96-97**: p. 90-99.

Appendix A: API Level I Evaluation

Following the procedure from the previous study [108] a modified Level 1 FAD analysis was undertaken using the results from an elastic-plastic finite element analysis. According to the modified Level 1 FAD, when the average von-Mises stress in the crack ligament of each model reaches the 435 MPa, the model is considered to fail by plastic collapse, and when the J-Integral value in the vicinity of the crack reaches the critical value of 197 kJ/m², the model will fail by fracture. In this study, all the models failed by plastic collapse.

The average von-Mises stress and J value for each crack geometry were calculated within the remaining ligament. J was determined when the J value was converged, a small distance from the crack tip, typically beyond the 10th element contour. The ligament stress was calculated in this same manner, where the stresses were calculated within the ligament for the area where the J-Integral was converged. For example, the result for the 47% crack is shown in Figure A1.

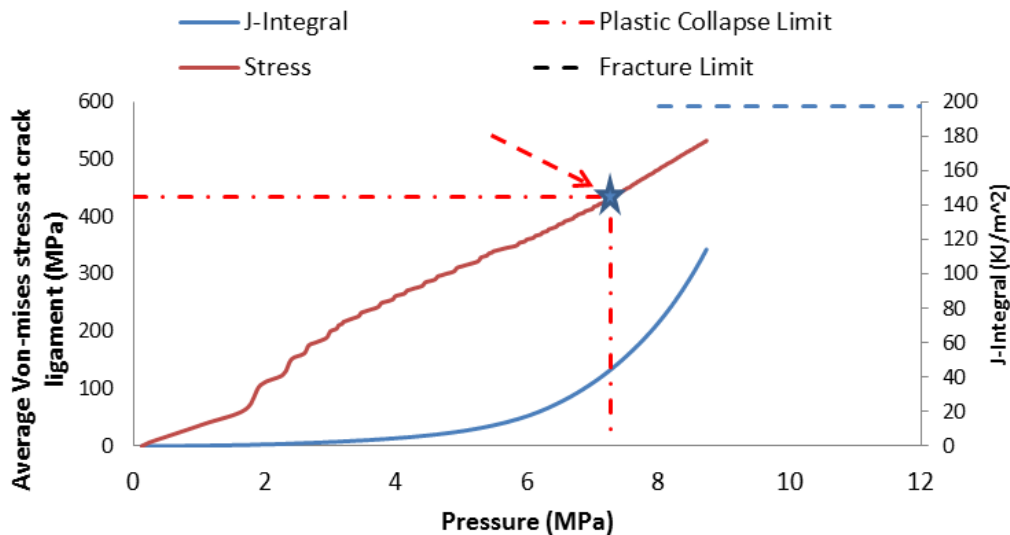


Figure A.1- FEM Analysis of 47% WT Crack Model using a Modified Level 1 FAD

Table A.1- FEM Collapse Pressure predictions for Crack Flaws

Test No.	Crack Depth (a) %WT	Experimental Collapse Pressure (MPa)	Predicted Collapse Pressure (MPa)		Difference (%)	
			FEMFEM API 579		FEMFEM API 579	
			Level 1		Level 1	
CR1	38	10.1	8.15		19.31	
CR2	47	9.30	7.27		21.83	
CR3	48	9.60	7.17		25.31	
CR4	51	8.83	6.79		23.10	
CR5	66	6.49	4.67		28.04	
		Average	Average		23.52	

Appendix B: Q-Stress

The T-stress is based on the elastic analysis and for high levels of plasticity and deformation it no longer describes the stress at the crack tip. Therefore, the Q-stress which is based on elastic-plastic analysis was applied. Modified Boundary Layer (MBL) should be applied to determine the value of Q-stress at the crack tip.

As mentioned in Equation (2.37) σ_{yy} at $T=0$ is required for calculation of the Q-stress. $(\sigma_{yy})_{T=0}$ corresponds to small scale yielding, i.e., the size of plastic region at the crack tip is negligible compared to the crack length. The term $(\sigma_{yy})_{T=0}$ is determined by constructing a circular model that contains a crack as shown in Figure B1 often referred to as modified boundary layer analysis (MBL).

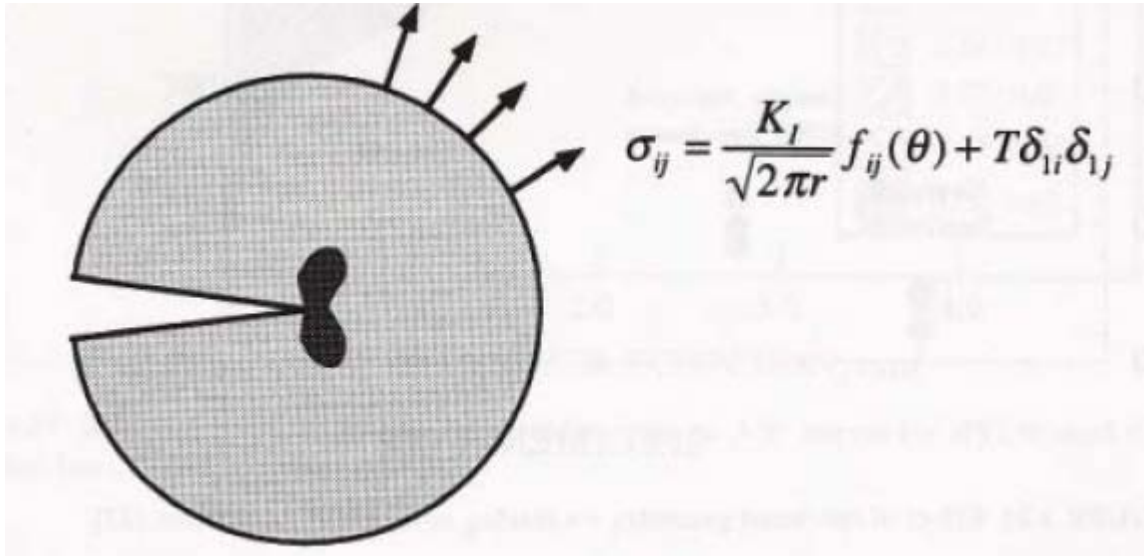


Figure B.1- Modified Boundary Layer Analysis

A finite element model was developed for MBL analysis as a semi-circular shape due to the symmetry. The crack was assumed as a sharp crack and the radius of the MBL model (semi-circular shape) was assumed as the crack depth of the pipe containing the crack. For instance, the

radius of the MBL model for 47% WT crack was 2.679 mm. The elastic stress field asymptotic stress field of a plane strain mode I crack was remotely applied (Figure B1). The remote stress was determined based on the equations shown in Figure B2. It was used to model the conditions around the crack tip. Eight-node plane strain elements (CPE8R) with reduced integration and a finer mesh at crack tip were used. The 2D meshes consisted of 13517 nodes and 4464 elements. The boundary conditions and mesh are shown in Figure B2 and Figure B3 respectively.

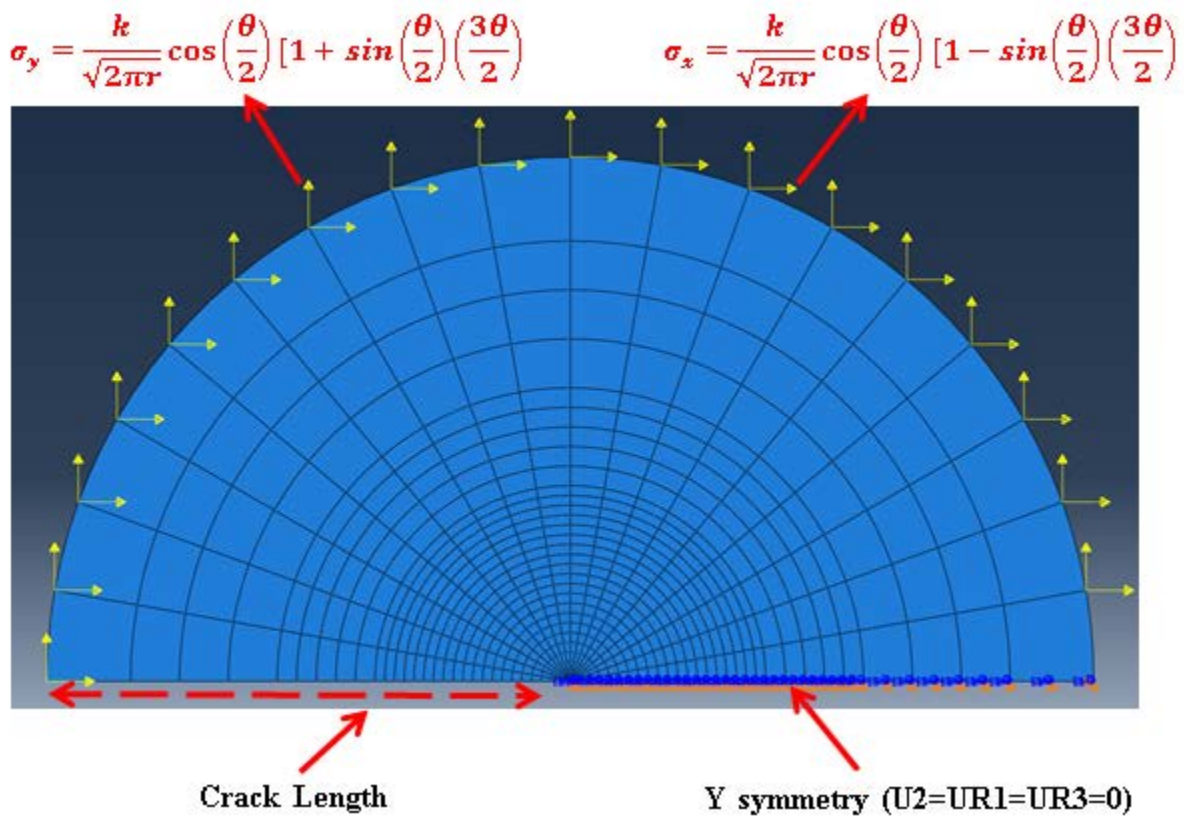


Figure B.2- Boundary Conditions of MBL Model (47%WT)

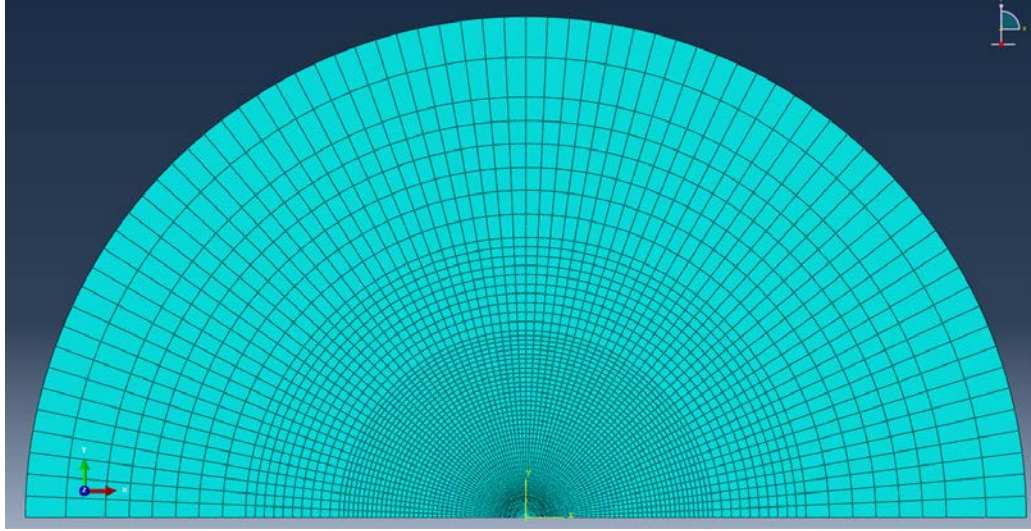


Figure B.3- Boundary Layer Mesh

The stress distribution obtained from the small strain analysis for $T=0$ under different loading levels is presented in Figure B4.

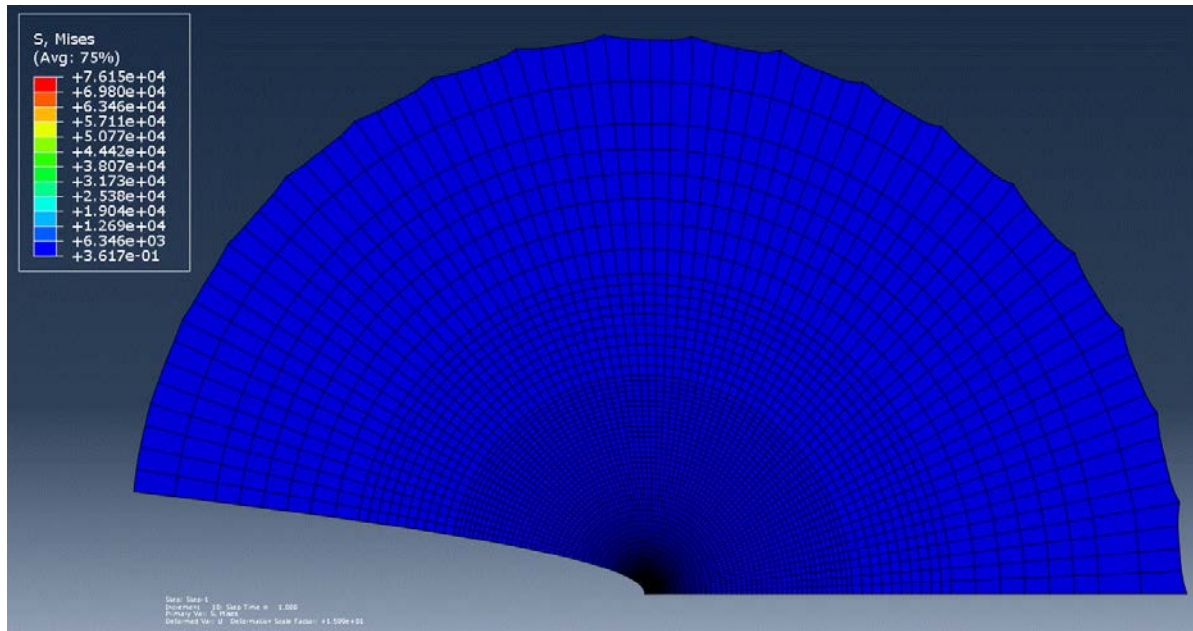


Figure B.4- von-Mises Stress Distribution for MBL Model (47% WT)

As shown, the stress is higher than the yield stress for the major part of the model. As mentioned the Q-stress can be calculated from the MBL model when there is small scale yielding around the crack tip in comparison with the rest of the model. But as shown in Figure B4 there is

large scale yielding throughout the whole model. Therefore, the Q-stress cannot be determined by the above model due to geometry limitations.